



POLITECHNIKA POZNAŃSKA



Wydział Inżynierii Materiałowej i Fizyki Technicznej

Instytut Fizyki

Zakład Fizyki Molekularnej

Karol Rytel

Opracowanie metod wytwarzania elektrod z nanomateriałów węglowych technikami Langmuira-Schaefera i ich charakteryzacja

Rozprawa doktorska

Promotor

prof. dr hab. Danuta Wróbel

POZNAŃ 2022

Badania w latach 2017-2021, zostały sfinansowane ze środków Narodowego Centrum Nauki, projekt PRELUDIUM 2016/21/N/ST8/03557, pt. „Opracowanie metod otrzymywania transparentnych elektrod na bazie nanorurek węglowych i grafenu technikami Langmuira”.



NARODOWE CENTRUM NAUKI

PODZIĘKOWANIA

Serdecznie dziękuję Pani Promotor prof. dr hab. Danucie Wróbel za cenne pomysły oraz wszystkie uwagi i wskazówki, bez których ta praca by nie powstała.

Szczególnie dziękuję dr. inż. Kamilowi Kędzierskiemu oraz dr. inż. Bolesławowi Barszczowi za współpracę oraz godziny dyskusji na tematy naukowe i nie tylko.

Dziękuję także wszystkim osobom, z którymi miałem okazję współpracować podczas prowadzonych badań.

Dziękuję również pracownikom i doktorantom Zakładu Fizyki Molekularnej za miłą atmosferę i wsparcie.

Szczególne dziękuję rodzicom Tadeuszowi i Alicji oraz cioci Ewie i wujkowi Mirkowi za bezustanne wsparcie podczas całej mojej dotychczasowej kariery naukowej.

Dziękuję także mojej żonie dr inż. Małgorzacie Widelickiej za wyrozumiałość podczas moich długich godzin pracy oraz za owocną współpracę podczas redagowania wspólnych prac.

Spis Treści

Streszczenie.....	4
Abstract.....	6
1. Forma rozprawy doktorskiej.....	8
2. Motywacja i cel rozprawy doktorskiej.....	9
3. Badane materiały oraz zastosowane techniki pomiarowe.....	11
4. Krótki opis badań składających się na rozprawę doktorską.....	13
5. Podsumowanie i wnioski.....	22
Literatura.....	24
Dorobek naukowy.....	28
Załączniki.....	34
Oświadczenia współautorów o wkładzie w publikacje naukowe doktoranta	34
Przedruk Publikacji [Rytel, PCCP 2018]	47
Przedruk Publikacji [Rytel, PCCP 2020]	60
Przedruk Publikacji [Rytel JoML 2022]	85
Przedruk Publikacji [Rytel Electr 2016]	101

Streszczenie

Prezentowana rozprawa doktorska opisuje wyniki prac badawczych nad warstwami nanomateriałów węglowych wytworzonymi metodami Langmuira. Badania miały na celu określenie wpływu procesu przygotowania zawiesiny, rozmiarów nanomateriałów węglowych oraz obecności barwnika na właściwości elektryczne i optyczne warstw, jak również pokazanie możliwości zastosowania wybranych warstw do poprawy parametrów pracy ogniów litowo-jonowych. Uzyskane wyniki zostały opisane w czterech artykułach naukowych z listy *Journal Citation Reports*.

W celu zbadania wpływu procesu przygotowania zawiesin na właściwości otrzymanych z nich warstw mieszaninę grafenu i dichlorometanu poddano działaniu ultradźwięków o mocach 60 W i 20 W przez okres czasu od 1 min do 180 min. Następnie z uzyskanych zawiesin wytworzono warstwy metodą Langmuira-Schaefera. Badania właściwości elektrycznych wykazały znaczący wzrost rezystancji powierzchniowej otrzymanych warstw w przypadku zastosowania wyższej mocy ultradźwięków podczas przygotowania zawiesiny. Na podstawie analizy wyników badań uzyskanych za pomocą spektroskopii rozproszenia Ramana oraz skaningowej mikroskopii elektronowej (SEM) wyjaśniono przyczyny wzrostu rezystancji powierzchniowej. Wykazano, że za wzrost rezystancji powierzchniowej odpowiedzialna była nie, jak początkowo zakładano, rosnąca ilość defektów, ale ich rodzaj. Badania te pozwoliły zoptymalizować proces przygotowania zawiesiny.

W dalszym etapie badań przygotowano zawiesiny wielościennych nanorurek węglowych (MWCNT) o różnym rozkładzie statystycznym średnic. Dla warstw wytworzonych metodą Langmuira-Schaefera zostały zmierzone rezystancje powierzchniowe i zarejestrowane widma transmitancji w zakresie UV-Vis. Następnie, wykorzystując metodę oscylujących barier, wyznaczono dla warstw Langmuira wartości zespolonych modułów kompresowalności oraz ścinania. Analiza otrzymanych wyników pokazała, że z powodu deformacji plastycznych warstw MWCNT w kierunku prostopadłym do kierunku kompresji warstwy, nie zawsze obserwuje się wzrost anizotropii rezystancji wraz z malejącą średnicą MWCNT. Dodatkowo, zauważono

korelację pomiędzy grubością ścianek MWCNT a przesunięciem maksimum pasma absorpcji w zakresie UV.

Na kolejnym etapie prac podjęto próbę zwiększenia współczynnika transmitancji warstw MWCNT. Do zrealizowania tego celu wykorzystano barwnik organiczny, który dodano do zawiesiny MWCNT i utworzono warstwy. Zastosowanie ftalocyjaniny cynkowej, która w warstwie wykazuje niską absorbancją w zakresie UV-Vis oraz silną fluorescencję, umożliwiło zwiększenie transmitancji otrzymanych warstw mieszanych do wartości około 98 %. Dodatkowo, uzyskano informacje na temat oddziaływań pomiędzy MWCNT a ftalocyjaniną cynkową. Zaobserwowano silne oddziaływania przyciągające pomiędzy MWCNT a makrocyklem oraz słabe oddziaływania odpychające pomiędzy MWCNT a grupami tert-butyłowymi ftalocyjaniny. Wykazano także, możliwość stosowania technik Langmuira do wyznaczania progów perkolacji wyrażonych jako ułamek masowy, ułamek powierzchniowy oraz gęstość powierzchniowa. Na podstawie uzyskanych wyników zaproponowano strategię doboru materiałów, która pozwala na optymalizację wartości rezystancji powierzchniowej warstw mieszanych. Opracowano także metodę pozwalającą na względnie łatwy i dokładny sposób określenia ułamków powierzchni zajmowanych przez każdy ze składników warstwy bez konieczności wykonania czasochłonnych badań mikroskopowych, która może mieć istotny wpływ na dalszy rozwój badań związanych z wyznaczaniem progów perkolacji.

Ostatni etap badań dotyczył możliwości zastosowania warstw MWCNT w technologii wytwarzania ogniw litowo-jonowych i ich wpływu na parametry pracy ogniwa. W tym celu zmodyfikowano kolektor prądowy katody poprzez naniesienie cienkiej warstwy MWCNT na jego powierzchnię. Wprowadzona modyfikacja pozwoliła na redukcję oporów wewnętrznych ogniwa, co spowodowało wzrost pojemności ogniw dla wysokich gęstości prądu ładowania/wyładowania. Ponadto, zastosowana modyfikacja umożliwiła zgromadzenie nawet do 43 % większej ilości energii podczas cyklu ładowania w porównaniu do elektrody referencyjnej.

Abstract

The presented doctoral dissertation describes the results of a research on the layers of carbon nanomaterials obtained using Langmuir methods. The aim of the research was to determine the influence of the process of preparing a suspension and/or the size of carbon nanomaterials and of the presence of a dye on the electrical and optical properties of the layers, as well as to show the possibility of using selected layers to improve the operating parameters of lithium-ion cells. The results obtained were presented in four scientific articles published in periodicals listed in *Journal Citation Reports*.

To study the influence of the suspension preparation process on the properties of the layers obtained therefrom, the mixture of graphene and dichloromethane was ultrasonicated at 60 W and 20 W power for a period of time from 1 min to 180 min. Layers were then produced from the suspensions obtained using the Langmuir-Schaefer method. The study of electrical properties showed a significant increase in the surface resistivity of the obtained layers when a higher ultrasound power was used during the preparation of the suspension. The origin of the increase in surface resistivity was explained on the basis of the analysis of results obtained with Raman scattering spectroscopy and scanning electron microscopy (SEM). It was shown that it was not the increase in the number of defects, as initially assumed, but rather their type which was responsible for the increase in surface resistivity. These studies allowed for optimization of the suspension preparation process.

In the further stage of the research, suspensions of multi-walled carbon nanotubes (MWCNT) with different statistical distributions of diameters were prepared. For the layers produced by the Langmuir-Schaefer method, surface resistivity and transmittance spectra in the ultraviolet-visible (UV-vis) range were measured. Then, using the oscillating barrier method, the values of the complex compressibility and complex shear moduli for Langmuir layers were determined. The analysis of the results obtained showed that due to plastic deformation of MWCNT layers in the direction perpendicular to the layer compression direction, an increase in resistivity anisotropy with a decreasing MWCNT diameter is not always observed. In addition, the correlation between the MWCNT wall thickness and the shift in the absorption band maximum in the UV range was noticed.

In the next stage of the work, an attempt was made to increase the transmittance coefficient of the MWCNT layers. To achieve this, an organic dye was used, which was added to the MWCNT suspension and layered therefrom. The use of zinc phthalocyanine, which in the layer exhibits low absorbance in the UV-vis range and strong fluorescence, allowed for an increase in the transmittance of the obtained mixed layers to about 98 %. Furthermore, information was also obtained on the interactions between MWCNT and zinc phthalocyanine. Strong attractive interactions between MWCNT and the macrocycle and weak repulsive interactions between MWCNT and tert-butyl groups of phthalocyanine were observed. The possibility of using Langmuir techniques to determine percolation thresholds expressed as mass fraction, surface fraction, and surface density was demonstrated. On the basis of the results obtained, a material selection strategy was proposed, which allows for optimizing the surface resistivity values of mixed layers. A method has been developed that allows for a relatively easy and accurate way to determine the surface fractions occupied by each of the layer components without the need for time-consuming microscopic examinations. This method may have a significant impact on the further development of research related to the determination of percolation thresholds.

The last stage of the research was related to the applicability of MWCNT layers in the production technology of lithium-ion cells and their influence on the working parameters of the cell. For this purpose, the cathode current collector was modified by depositing a thin MWCNT film on its surface. The introduced modification made it possible to reduce the internal resistance of the cell, which caused an increase in the cell capacity for high charge/discharge current densities. Moreover, the applied modification allowed to accumulate up to 43 % more energy during the charging cycle compared to the reference electrode.

1. Forma rozprawy doktorskiej

Rozprawa doktorska pt. „Opracowanie metod wytwarzania elektrod z nanomateriałów węglowych technikami Langmuira-Schaefera i ich charakteryzacja” składa się z czterech artykułów naukowych opublikowanych w recenzowanych czasopismach znajdujących się na liście *Journal Citation Reports* (JCR). Poniżej zamieszczono zestawienie ww. artykułów wraz z liczbą punktów przyznanych dla danego czasopisma przez Ministerstwo Edukacji i Nauki (MEiN) oraz współczynnikiem wpływu *Impact Factor* (IF), Prezentowany cykl artykułów dotyczy metod wytwarzania i charakteryzacji cienkich warstw nanomateriałów węglowych oraz potencjalnych możliwości ich zastosowań.

[Rytel, PCCP 2018] K. Rytel, M. Widelicka, D. Łukawski, F. Lisiecki, K. Kędziński, D. Wróbel, *Ultrasonication-induced sp^3 hybridization defects in Langmuir-Schaefer layers of turbostratic graphene*, *Phys. Chem. Chem. Phys.* 20 (2018) 12777–12784. doi:10.1039/c8cp01363b. (MEiN 40, IF 3.567)

[Rytel, PCCP 2020] K. Rytel, K. Kędziński, B. Barszcz, M. Widelicka, A. Stachowiak, A. Biadasz, Ł. Majchrzycki, E. Coy, D. Wróbel, *The influence of diameter of multiwalled carbon nanotubes on mechanical, optical and electrical properties of Langmuir-Schaefer films*, *Phys. Chem. Chem. Phys.* 22 (2020) 22380–22389. doi:10.1039/d0cp03687k. (MEiN 100, IF 3.676)

[Rytel JoML 2022] K. Rytel, K. Kędziński, B. Barszcz, B. Biadasz, Ł. Majchrzycki, D. Wróbel, *The influence of zinc phthalocyanine on the formation and properties of multiwalled carbon nanotubes thin films on the air-solid and air-water interface*, *J. Mol. Liq.* 350 (2022) 118548-1–118548-8. doi:10.1016/j.molliq.2022.118548 (MEiN 100, IF 6,165)

[Rytel Electr 2016] K. Rytel, D. Waszak, K. Kędziński, D. Wróbel, *Novel method of current collector coating by multiwalled carbon nanotube Langmuir layer for enhanced power performance of $LiMn_2O_4$ electrode of Li-ion batteries*, *Electrochim. Acta.* 222 (2016) 921–925. doi:10.1016/j.electacta.2016.11.058. (MEiN 40, IF 4,798)

Wkład autora rozprawy w przygotowanie każdego z wyżej wymienionych artykułów był znaczący i polegał na: zaplanowaniu oraz koordynacji prac badawczych, przeprowadzeniu

większości prac eksperymentalnych, opracowaniu i analizie otrzymanych wyników oraz przygotowaniu manuskryptu. Stosowne oświadczenia współautorów zostały zamieszczone w końcowej części rozprawy.

2. Motywacja i cel rozprawy doktorskiej

Nanomateriały są to naturalnie występujące lub wytworzone materiały, których przynajmniej jeden z wymiarów jest mniejszy od 100 nm (zgodnie z zaleceniem 2011/696/UE dotyczącym definicji nanomateriału). Ze względu na możliwość tworzenia stabilnych wiązań chemicznych o trzech różnych hybrydyzacjach (sp^1 , sp^2 , sp^3), węgiel posiada wiele odmian alotropowych. Powszechnie znanymi odmianami alotropowymi węgla są węgiel amorficzny, diament, grafit, grafen, fuleren i nanorurka węglowa (CNT). W literaturze można też znaleźć doniesienia o bardziej „egzotycznych” formach węgla takich jak grafedien, graphyn oraz węglowe kropki kwantowe. [1–4]

Wpływ na właściwości nanomateriału węglowego ma nie tylko hybrydyzacja wiązań C-C, ale też wiele innych czynników. Przykładowo jednościenne nanorurki węglowe (SWCNT) w zależności od kąta chiralnego oraz średnicy mogą posiadać właściwość metaliczne lub półprzewodnikowe. [5,6] Dodatkowo zarówno średnica i grubość ścianek nanorurek węglowych (CNT) może mieć wpływ na ich wytrzymałość mechaniczną [7] i właściwości optyczne. [8–10] Z kolei na właściwości grafenu największy wpływ ma ilość i rodzaj defektów w ich strukturze oraz liczba warstw. [11–13] Przykładem może być grafen turbostratyczny (dwie warstwy grafenu skrócone względem siebie o kąt w przedziale $0-30^\circ$), w którym w zależności od ilości defektów oraz kąta skrócenia warstw może występować przewodnictwo balistyczne. [14,15]

Różnorodność właściwości nanomaterialów wynikająca ze zmian strukturalnych lub czynników zewnętrznych otwiera wiele możliwości ich zastosowania, ale też przysparza wielu trudności przy produkcji wielkoskalowej. Zarówno nanorurki węglowe i grafen posiadają niezwykle właściwości mechaniczne i elektryczne. Moduł Younga dla tych materiałów wynosi około 1 TPa, a ich wytrzymałość na rozciąganie dochodzi do wartości wynoszących około 100 GPa. [7,16] Z kolei biorąc pod uwagę przewodnictwo balistyczne, które występuje zarówno w grafenie jak i w

CNT nie jest możliwe określenie teoretycznego górnego limitu wartości przewodności właściwej tych materiałów. [17,18]

Niestety, niezwykle trudne jest, aby układ złożony z większej liczby nanomateriałów miał właściwości będące wypadkową poszczególnych jego składników. Pogorszenie przewodności właściwej lub odporności na rozciąganie spowodowane jest wpływem defektów, zanieczyszczeń, brakiem uporządkowania poszczególnych składników lub też oddziaływaniami pomiędzy nimi. W związku z tym, budując urządzenie w oparciu o nanomateriały węglowe, istotne jest zrozumienie i zbadanie czynników wpływających na uzyskanie pożądanych parametrów jego pracy. Pomimo powyższych problemów nanomateriały węglowe znajdują zastosowanie w bateriach litowo-jonowych, sensorach, tranzystorach polowych i transparentnych elektrodach. [19–24]

Warunkiem koniecznym do zastosowania nanomateriałów węglowych jest możliwość wytworzenia z nich cienkiej warstwy. Najlepszej jakości warstwy można otrzymać za pomocą wyrafinowanych metod takich jak wzrost epitaksjalny czy metoda pirolizy katalitycznej (CVD). [25,26] Niestety wysokie koszty produkcji i wykorzystanie specjalistycznej aparatury ograniczają możliwości zastosowania tych metod w produkcji wielkoskalowej. Z drugiej strony często stosowane są znacznie tańsze oraz potencjalnie skalowalne metody otrzymywania cienkich warstw takie jak: powlekanie obrotowe, powlekanie natryskowe, metoda roll-to-roll, czy też metody Langmuira. [27–33]

W badaniach opisanych w niniejszej pracy doktorskiej do otrzymywania warstw zastosowano metody Langmuira. Metody te posiadają wiele unikalnych możliwości. Zarówno gęstość upakowania i morfologia warstwy może być kontrolowana poprzez ciśnienie powierzchniowe, przy którym warstwa jest badana *in situ* lub/i przenoszona na podłoże stałe. W przypadku zastosowania tlenku grafenu zależnie od wartości ciśnienia powierzchniowego można otrzymać warstwę złożoną z płatków o płaskiej, falistej, stojącej zapadniętej lub silnie zakrzywionej strukturze.[34] Zmiana struktury płatków powoduje, że powierzchnia właściwa warstwy rośnie wraz ze wzrostem ciśnienia powierzchniowego. W przypadku CNT anizotropia oporu elektrycznego warstwy rośnie wraz ze wzrostem wartości ciśnienia powierzchniowego. [27,35] Wpływ na anizotropię oporu elektrycznego warstwy ma również proces jej sprężania. Dodatkowy wpływ na proces porządkowania CNT w warstwie mają takie czynniki jak prędkość

filmu względem subfazy, lepkość subfazy oraz stosunek długości CNT do ich średnicy. [36] Inną zaletą metod Langmuira jest możliwość otrzymania warstwy o grubości porównywalnej ze średnicą CNT lub grubością płatków grafenowych oraz możliwość precyzyjnego określenia masy nanomateriału przypadającej na jednostkę powierzchni warstwy.

Zasadniczym celem badań opisanych w prezentowanej rozprawie doktorskiej było otrzymanie cienkich warstw z nanomateriałów węglowych charakteryzujących się jak najniższym oporem elektrycznym i jednocześnie jak najwyższą transmitancją oraz sprawdzenie czy ich zastosowanie wpłynie na poprawę parametrów pracy wybranego urządzenia. Podczas realizacji ww. zamierzeń wykonano badania prowadzące do:

- określenia wpływu mocy ultradźwięków stosowanych podczas przygotowania zawiesiny nanomateriałów węglowych na właściwości optyczne i elektryczne wytworzonej warstwy;
- zbadania jaki wpływ ma średnica CNT na właściwości optyczne i elektryczne warstwy oraz na możliwość uzyskania anizotropii ułożenia CNT;
- zwiększenia transmitancji poprzez zastosowanie dodatkowego, organicznego składnika w warstwie CNT;
- poprawy parametrów pracy ogniwa litowo-jonowego poprzez modyfikację powierzchni kolektora prądowego warstwą CNT.

3. Badane materiały oraz zastosowane techniki pomiarowe

Podczas badań w ramach pracy doktorskiej wykorzystano komercyjnie dostępne nanomateriały takie jak: grafen turbostratyczny (wielkość płatków: 150-500 nm, liczba warstw wg. danych producenta: 2-3), wielościennie nanorurki węglowe (MWCNT) o różnych średnicach (6-25 nm) i stałej długości (5 μm). Wszystkie badania (z wyjątkiem badań przeprowadzonych dla ogniw litowo-jonowych, metodą spektroskopii ramanowskiej oraz mikroskopii elektronowej) wykonano w laboratoriach Zakładu Fizyki Molekularnej w Instytucie Fizyki na Wydziale Inżynierii Materiałowej i Fizyki Technicznej Politechniki Poznańskiej.

Do przygotowania zawiesin nanomateriałów węglowych użyto homogenizatora ultradźwiękowego, a ich jakość oceniano na podstawie widm rejestrowanych w zakresie UV-Vis za pomocą spektrofotometru absorpcyjnego. Otrzymane zawiesiny wykorzystano do wytworzenia warstw na granicy faz woda-powietrze (technika Langmuira), dla których rejestrowano, podczas ich sprężania, zależność ciśnienia powierzchniowego w funkcji powierzchni warstwy (izoterma Π -A). Właściwości reologiczne warstw oceniono wykorzystując do badań metodę oscylujących barier oraz analizując izotermy Π -A. Przeprowadzone badania umożliwiły wyznaczenie optymalnych warunków transferu warstwy na podłoże stałe oraz określenie oddziaływań pomiędzy składnikami warstwy

Warstwy badanych nanomateriałów węglowych przenoszono na podłoża stałe (aluminium, kwarc, polichlorek winylu) wykorzystując metody Langmuira-Schaefera oraz Langmuira-Blodgett. Dla warstw na podłożach stałych rejestrowano widma absorpcji w zakresie UV-Vis, na ich podstawie wyznaczano transmitancję warstw oraz analizowano wpływ różnego rodzaju czynników, takich jak moc ultradźwięków, średnica i grubość ścianki CNT lub obecność dodatkowego składnika w warstwie, na położenie pasm plazmonowych nanomateriałów węglowych. Jakość/jednorodność pokrycia podłoża badaną warstwą była określana wykorzystując metody mikroskopii elektronowej oraz skaningowej mikroskopii konfokalnej, w trybie odbiciowym oraz fluorescencyjnym. Uzyskane informacje pozwoliły na optymalizację parametrów transferu warstwy oraz oszacowanie powierzchni warstwy koniecznej do wyznaczenia rezystancji powierzchniowej. Badania elektryczne wykonano zarówno w układach cztero- i dwu-elektrodowych za pomocą źródła mierzącego, a elektrody do badań elektrycznych wytworzono używając pasty srebrnej. Wyznaczenie rezystancji powierzchniowej otrzymanych warstw umożliwiło ocenę ich możliwości potencjalnego zastosowania jako transparentne elektrody. Ponadto, określono wpływ poszczególnych etapów procesu przygotowania/wytworzenia warstwy na wyznaczoną wartość rezystancji powierzchniowej oraz na anizotropię ułożenia badanych nanomateriałów w warstwach.

Pomiary z wykorzystaniem skaningowej mikroskopii elektronowej (SEM) wykonane zostały przez dr. inż. Łukasza Majchrzyckiego (Centrum Zaawansowanych Technologii Uniwersytetu im. Adama Mickiewicza w Poznaniu) oraz przez dr. inż. Filipa Lisickiego (Instytut Fizyki Molekularnej Polskiej Akademii Nauk w Poznaniu), a transmisyjnej mikroskopii elektronowej

(TEM) zostały wykonane przez dr. hab. inż. Emersona Coy'a, prof. UAM (Centrum NanoBioMedyczne Uniwersytetu im. Adama Mickiewicza w Poznaniu). Analiza uzyskanych obrazów mikroskopowych pozwoliła na precyzyjne wyznaczenie rozmiarów badanych nanomateriałów oraz na określenie morfologii warstw w nanoskali.

Pomiary widm rozproszenia Ramana zostały wykonane przez dr. inż. Bolesława Barszcza oraz przez dr inż. Małgorzatę Widelicką (Instytut Fizyki Molekularnej Polskiej Akademii Nauk w Poznaniu). Na podstawie uzyskanych wyników skontrolowano i oceniono jakość badanych nanomateriałów, w tym ilość oraz rodzaju defektów.

Montaż ogniw litowo-jonowych, pomiary galwanostatyczne, cykliczności pracy oraz pomiary z wykorzystaniem spektroskopii impedancyjnej zostały wykonane przez doktoranta, pod opieką dr. Daniela Waszaka, w Centralnym Laboratorium Akumulatorów i Ogniw Instytutu Metali Nieżelaznych, Oddział w Poznaniu (obecnie Sieć Badawcza Łukasiewicz – Instytut Metali Nieżelaznych). Wyniki tych badań umożliwiły ocenę wpływu cienkiej warstwy CNT modyfikującej kolektor prądowy na podstawowe parametry pracy ogniwa litowo-jonowego.

4. Krótki opis badań składających się na rozprawę doktorską

W pracy [Rytel, PCCP 2018] opisano badania dotyczące wpływu procesu homogenizacji ultradźwiękowej zawiesiny grafenu, wykorzystywanej do wytworzenia warstw Langmuira-Schaefera, na właściwości optyczne i elektryczne warstw. Homogenizacja ultradźwiękowa jest szeroko stosowaną metodą otrzymywania zawiesin w rozpuszczalnikach zarówno organicznych i nieorganicznych. Podczas gdy, większość zastosowań nanomateriałów węglowych nie wykorzystuje bezpośrednio zawiesin, to wiele z nich wymaga ich użycia na pewnym etapie procesu (np. osadzanie cienkich warstw lub wytwarzania materiałów kompozytowych). Istotne jest, aby proces homogenizacji ultradźwiękowej pozwolił na jak najlepszą dyspersję zastosowanego materiału i jednocześnie nie wpływał na zmianę jego właściwości strukturalnych. Celem przeprowadzonych badań było uzyskanie odpowiedzi na następujące pytania:

- Czy płatki grafenowe poddane procesowi homogenizacji ultradźwiękowej zmieniają rozmiar?

- Czy względnie niska moc ultradźwięków może wpływać na strukturę wiązań C-C i powodować zmianę hybrydyzacji?
- Jak przygotowanie zawiesiny, w tym czas trwania procesu homogenizacji oraz zastosowana moc ultradźwięków, może wpływać na rezystancję powierzchniową oraz transmitancję otrzymanych warstw?

Jako materiał do badań wybrano grafen turbostratyczny (G1B, Cambridge Nanosystems Ltd) o rozmiarach płatków (150-500 nm). Zauważono, że w przypadku małych rozmiarów płatków grafenowych ultradźwięki nie wpływają na zmianę ich rozmiaru, co w znaczącym stopniu ułatwia analizę otrzymanych wyników. Przygotowano dwie zawiesiny grafenu w dichlorometanie (DCM) o identycznym stężeniu, które następnie były wystawione na działanie ultradźwięków o mocy 60 W i 20 W, przez czas wynoszący odpowiednio 120 min i 180 min. Zawiesiny grafenu w DCM, o stałej objętości, wykorzystane do przygotowania warstw Langmuira były pobierane w ściśle określonym czasie.

Warstwy wytworzono poprzez nakropienie pobranej zawiesiny na powierzchnię wody, a po odparowaniu rozpuszczalnika warstwy sprężano. Podczas kompresji warstw rejestrowane były izotermy Π -A, na podstawie których obliczono moduły kompresowalności. Dla wszystkich wykonanych pomiarów zaobserwowano niemal identyczne zależności modułu kompresowalności od ciśnienia powierzchniowego. Maksimum modułu kompresowalności wynoszące około 120 mN m^{-1} występowało przy ciśnieniu powierzchniowym wynoszącym 40 mN m^{-1} . Warstwy przeniesiono na podłoża kwarcowe metodą Langmuira-Schaefera przy stałym ciśnieniu powierzchniowym odpowiadającym maksimum kompresowalności. Zaobserwowano, że wraz z wydłużającym się czasem homogenizacji ultradźwiękowej zawiesiny, powierzchnia warstw stopniowo rośnie przy stałym ciśnieniu powierzchniowym. Zmiana powierzchni warstwy związana była stopniem dyspersji grafenu, co potwierdziły wyniki badań morfologii warstwy uzyskane za pomocą mikroskopii elektronowej oraz spektroskopii absorpcyjnej w zakresie UV-Vis.

W celu dokładniejszego określenia wpływu procesu homogenizacji ultradźwiękowej zawiesiny grafenu na właściwości optyczne oraz gęstość upakowania jego płatków w warstwie wykonano pomiary transmitancji warstw w zakresie UV-Vis. Najwyższe wartości transmitancji warstw wynoszące 82,6 % (60 W) i 77,7 % (20 W) zaobserwowano przy długości fali 550 nm. Na

podstawie wartości transmitancji oszacowano liczbę płaszczyzn grafenowych w warstwie, która mieściła się w przedziale od 23,2 do 10,8 oraz od 12,8 do 8,2 dla mocy ultradźwięków wynoszących odpowiednio 20 W i 60 W.

Zależność rezystancji powierzchniowej od czasu trwania procesu homogenizacji zawiesiny miała charakter nasyceniowy dla mocy ultradźwięków wynoszącej 20 W. Z kolei dla mocy ultradźwięków wynoszącej 60 W zaobserwowano stopniowy wzrost rezystancji powierzchniowej wraz ze wzrostem czasu homogenizacji. Najniższe wartości rezystancji powierzchniowej wynoszące $68 \text{ k}\Omega \text{ kw}^{-1}$ oraz $87 \text{ k}\Omega \text{ kw}^{-1}$ zaobserwowano dla mocy ultradźwięków wynoszącej odpowiednio 20 W i 60 W.

Na podstawie wyników uzyskanych za pomocą spektroskopii rozproszenia Ramana, tj. położenia oraz szerokości połówkowej pasma 2D określono, że płatki grafenowe składały się z dwóch warstw. W celu wyjaśnienia przyczyn wzrostu rezystancji powierzchniowej warstw, obliczono także stosunki intensywności integralnych pasm D do G oraz pasm D' do D i stwierdzono, że czas homogenizacji nie wpływa na ilość defektów niezależnie od zastosowanej mocy ultradźwięków. Natomiast, zastosowanie ultradźwięków o mocy 60 W powoduje zmianę dominującego rodzaju defektów w strukturze płatków z wakansów na defekty o hybrydyzacji sp^3 .

W pracy [Rytel PCCP 2020] opisano badania dotyczące wpływu średnicy wielościennych nanorurek węglowych (MWCNT) na właściwości optyczne i elektryczne warstw Langmuira-Schaefera. Średnica jednościennych nanorurek węglowych (SWCNT) ma znaczący wpływ na ich właściwości, natomiast w przypadku MWCNT zmiany te są bardziej subtelne lub występują dodatkowe czynniki, które mogą determinować ich właściwości. Dobrym przykładem różnic pomiędzy MWCNT a SWCNT jest położenie pasm π -plazmonowych. Dla SWCNT pasma te przesuwają się w stronę niższych energii wraz ze wzrostem średnicy. Podczas gdy, w przypadku MWCNT przesunięcie pasm π -plazmonowych może, ale nie musi występować. Kolejną istotną kwestią jest możliwość otrzymania warstw o możliwie wysokim stopniu uporządkowania (wysokiej anizotropii) w kierunku horyzontalnym. Stosując metody Langmura możliwe jest otrzymanie warstw SWCNT o bardzo wysokiej anizotropii. W przypadku MWCNT, stosując te same metody, możliwe jest uzyskanie warstw o nieznacznym stopniu uporządkowania lub nawet jego braku.

Celem przeprowadzonych badań było uzyskanie odpowiedzi na następujące pytania:

- Jaki jest wpływ średnicy MWCNT na właściwości mechaniczne warstw?
- Co powoduje przesunięcie pasm π -plazmonowych dla różnych rodzajów MWCNT?
- Co powoduje, że anizotropia warstw SWCNT jest znacznie większa od tej obserwowanej dla MWCNT?
- Jaki jest wpływ średnicy MWCNT na rezystancję powierzchniową oraz transmitancję warstw?

Jako materiał do badań wybrano MWCNT (Carbon Nanotubes Plus) charakteryzujące się położeniami maksimum rozkładu statystycznego średnic wynoszącymi $8,86 \pm 0,45$ nm, $11,19 \pm 0,33$ nm, $15,81 \pm 0,28$ nm, $16,19 \pm 0,37$ nm oraz $18,1 \pm 0,5$ nm. Rozkład statystyczny średnic wyznaczono na podstawie pomiarów TEM dla próby statystycznej w przedziale od 100 do 200 pomiarów. Pomiarów te umożliwiły także wyznaczenie średnic wewnętrznych MWCNT. Dla wszystkich badanych materiałów stosunek średnicy wewnętrznej do zewnętrznej wynosił około 0,3.

Wszystkie zawiesiny MWCNT przygotowano stosując identyczny czas oraz moc ultradźwięków (20 min, 60 W). Stężenie MWCNT dobrano w taki sposób, aby po nakropieniu 10 ml zawiesiny możliwe było wytworzenie warstwy o powierzchni wynoszącej 200 cm^2 przy ciśnieniu powierzchniowym $37,5 \text{ mN m}^{-1}$. Podejście to umożliwiło uzyskanie powtarzalnych wyników podczas dalszych badań warstw. Pomiarów ciśnienia powierzchniowego w funkcji powierzchni przypadającej na μg MWCNT (izotermy Π - A_r) wykonano jednocześnie dla dwóch wzajemnie prostopadłych kierunków ułożenia płytki Wilhelmięgo. Na podstawie izoterm Π - A_r obliczono moduły kompresowalności warstw, co pozwoliło na dobranie optymalnego ciśnienia powierzchniowego do transferu warstw na podłoża stałe. Zaobserwowano wyraźną zależność zarówno kształtu izoterm Π - A_r jak i wartości modułu kompresowalności od kierunku ułożenia płytki Wilhelmięgo. Badania właściwości mechanicznych warstw rozszerzono wykorzystując metodę oscylujących barier i wyznaczono wartości zespolonych modułów kompresowalności oraz zespolonych modułów ścinania. Zaobserwowano wzrost wartości parametrów mechanicznych warstw wraz ze wzrostem średnicy MWCNT..

Wykorzystując skaningową mikroskopię elektronową określono morfologię warstw wytworzonych na podłożach stałych. Zaobserwowano, że wraz ze wzrostem średnicy MWCNT rośnie gęstość ich upakowania w warstwie, natomiast nie wykazano wyraźniej anizotropii ułożenia MWCNT w badanych warstwach.

Dla warstw na podłożu stałym zarejestrowano także widma absorpcji w zakresie UV-Vis, w świetle spolaryzowanym i niespolaryzowanym. Zaobserwowano wyraźną zależność położenia maksimum absorpcji od średnicy MWCNT. Wydaje się, że najbardziej prawdopodobną przyczyną przesunięcia maksimum absorpcji jest zmiana grubości ścianki badanych MWCNT. Wraz ze wzrostem grubości ścianki MWCNT przesunięciu ulega nisko-energetyczna składowa pasma π -plazmonowego. Dodatkowo, podczas badań w świetle spolaryzowanym zaobserwowano różnicę w wartościach transmitancji warstw oraz położenia maksimum pasm absorpcji w zależności od kierunku polaryzacji światła. Analiza wyników sugeruje istnienie niewielkiej anizotropii ułożenia MWCNT w warstwach na podłożach stałych.

W celu uzyskania dodatkowych informacji o właściwościach anizotropowych, dla badanych warstw zmierzono rezystancję powierzchniową w dwóch wzajemnie prostopadłych kierunkach. W celu minimalizacji wpływu zanieczyszczeń, warstwy wygrzano w atmosferze argonowej pod obniżonym ciśnieniem, co zgodnie z oczekiwaniem spowodowało spadek wartości rezystancji powierzchniowej. Analiza widm Ramana potwierdziła, że ilość defektów nie miała wpływu na uzyskane wartości rezystancji powierzchniowej. Najniższą rezystancję powierzchniową ($35,8 \pm 2,4$ k Ω /kw) zaobserwowano dla MWCNT o średnicy 11 nm. Wartość anizotropii elektrycznej otrzymanych warstw oszacowano na podstawie stosunków wartości rezystancji powierzchniowej dla dwóch wzajemnie prostopadłych kierunków. Najwyższą wartość anizotropii elektrycznej warstw wynoszącą $2,5 \pm 0,3$ zaobserwowano dla MWCNT o średnicy 11 nm. Warstwy MWCNT o średnicach 16 nm i 18 nm uznano za izotropowe.

Na podstawie obliczonych wartości anizotropii elektrycznej oraz wartości zespolonych modułów ścinających udowodniono, że głównym czynnikiem uniemożliwiającym uzyskanie wysokiej anizotropii ułożenia MWCNT w warstwach są odkształcenia plastyczne w kierunku prostopadłym do kierunku kompresji warstwy.

W pracy przeanalizowano także możliwość zastosowania wytworzonych warstwy jako transparentnych elektrod. Na podstawie otrzymanych wyników wydaje się, że najlepsze do tego celu będą warstwy utworzone z MWCNT o jak najmniejszych średnicach. W przypadku stosowania MWCNT o małych średnicach, zalecane jest stosowanie procesu wygrzewania warstw, aby uzyskać dla nich możliwe najniższą rezystancję powierzchniową. Ponadto, uzyskane wyniki pokazały, że jeśli uda się wytworzyć warstwy o bardzo wysokiej anizotropii ułożenia MWCNT, to możliwe jest otrzymanie warstw MWCNT o rezystancji powierzchniowej mniejszej niż $100 \Omega \text{ km}^{-1}$ i transmitancji około 90 %.

W pracy [Rytel JoML 2022] opisano wpływ ftalocyjaniny cynkowej (FC) na właściwości optyczne i elektryczne warstw MWCNT. W badaniach opisanych powyżej wykazano, że wartość transmitancji warstw nanomateriałów węglowych wytworzonych za pomocą metod Langmuira może być zbyt niska, aby możliwe było zastosowanie ich jako transparentnych elektrod. Zwiększenie wartości transmitancji warstw nanomateriałów węglowych możliwe jest, jeśli zwiększeniu ulegnie odległość pomiędzy nanomateriałami węglowymi, przy jednoczesnym zachowaniu możliwie dużej liczby połączeń elektrycznych między nimi. Efekt ten można uzyskać na przykład poprzez obniżenia ciśnienia powierzchniowego, przy którym warstwa jest przenoszona na podłoże stałe. Niestety, stosując to podejście możliwe jest uzyskanie wzrostu wartości transmitancji tylko w niewielkim zakresie. Alternatywą metodą uzyskania wyższych wartości transmitancji jest wprowadzenie w strukturę warstwy dodatkowych (najlepiej w pełni transparentnych) materiałów. Jednakże, taka modyfikacja struktury może spowodować wzrost wartości rezystancji powierzchniowej warstwy dwuskładnikowej. Aby proces modyfikacji wykonać i uzyskać oczekiwane efekty, należy wcześniej zbadać i zrozumieć oddziaływania pomiędzy składnikami warstwy. W związku z tym przeprowadzono badania, które miały na celu:

- Wykazanie, że na podstawie analizy izoterm Π - A_r możliwe jest wyznaczenie siły oraz kierunku oddziaływań pomiędzy składnikami warstwy;
- Sprawdzenie, czy możliwe jest określenie, które grupy chemiczne ftalocyjaniny cynkowej odpowiedzialne są za oddziaływania z MWCNT;
- Zbadanie, czy oddziaływania pomiędzy składnikami warstwy wpływają na jej morfologię;

- Określenie jak stężenie barwnika wpływa na wartości transmitancji i rezystancji powierzchniowej warstw.

Jako materiały do wytworzenia warstw wybrano MWCNT o rozkładzie statystycznym średnic w przedziale od 6 nm do 9 nm (Sigma-Aldrich) oraz 2,9,16,23-tetra-tert-butyl-29H,31H-ftalocyjaninę cynku (Sigma-Aldrich). Rolą MWCNT w warstwie było przewodzenie ładunku elektrycznego. Natomiast, PC została wybrana do pełnienia roli separatora MWCNT w warstwach Langmuira w celu zwiększenia ich transmitancji. PC w monowarstwach wykazuje wysoką transmitancję, a dodatkowo charakteryzuje się wydajną fluorescencją, co stwarza możliwości zastosowania mikroskopii fluorescencyjnej w celu rozszerzenia badań morfologii warstw.

Do badań przygotowano zawiesinę MWCNT ($20 \mu\text{g ml}^{-1}$) oraz roztwór PC ($160,4 \mu\text{g ml}^{-1}$) w dichlorometanie, które wykorzystano do wytworzenia dziewięciu mieszanin o stosunku masy MWCNT do PC w przedziale od 0 do 1. Mieszaniny te wykorzystano do utworzenia warstw na granicy faz woda-powietrze, dla których zarejestrowano izotermy Π - A_r . Na podstawie izoterm Π - A_r wyznaczono zależność modułu kompresowalności od ciśnienia powierzchniowego, nadmiarowe energie Gibbsa, powierzchnie nadmiarowe oraz ułamki powierzchniowe zajmowane przez składniki mieszaniny.

Położenie maksimum modułu kompresowalności pozwoliło na określenie optymalnego ciśnienia przenoszenia warstwy. Warstwy przenoszono przy ciśnieniach powierzchniowych odpowiadających położeniu maksimum modułu kompresowalności, które zmieniało się w zależności od składu mieszaniny. Zastosowane podejście zapewniło możliwie wysokie upakowanie MWCNT oraz PC, zapobiegając jednocześnie tworzeniu się wielowarstwy.

Dla badanych mieszanin, problematyczne okazało się obliczenie nadmiarowych energii Gibbsa, ze względu na to, że do obliczeń konieczna jest znajomość stężenia molowego poszczególnych składników. Niestety niemożliwe było precyzyjne określenie stężenia molowego zawiesiny MWCNT, dlatego rozwiązano ten problem wykorzystując do obliczeń stężenia masowe zamiast molowych. Konsekwencją tego podejścia jest zmiana jednostki nadmiarowej energii Gibbsa z $[\text{J} / \text{molekułę}]$ na $[\text{J} / \text{jednostkę masy składników mieszaniny}]$.

Zaproponowano także, metodę obliczania ułamka powierzchniowego zajmowanego przez wybrany składnik mieszaniny (AF) na dowolnym etapie kompresji warstwy oraz przy dowolnym składzie mieszaniny. Do obliczenia wartości AF konieczna jest znajomość parametrów warstwy referencyjnej (współczynnik wypełnienia oraz powierzchnia na jednostkę masy wybranego składnika mieszaniny). Zastosowanie tej metody w znaczący sposób ułatwia i przyspiesza analizę wyników wymagającą określenia, jaką część powierzchni warstwy zajmuje każdy z jej składników.

Na podstawie analizy wartości opisanych powyżej parametrów wyjaśniono, jaki wpływ mają oddziaływania pomiędzy PC i MWCNT na formowanie się warstwy. Proces wypełniania warstwy MWCNT przez PC można podzielić na trzy etapy. Dla niskich stężeń barwnika dominujące są siły odpychające pomiędzy grupą tetr-butylową barwnika a MWCNT, co powoduje, że PC rozmieszczona jest regularnie wewnątrz warstwy. Dla średnich stężeń barwnika dominujące stają się oddziaływania przyciągające pomiędzy makrocyklem PC a MWCNT i obserwuje się powstawanie inkluzji barwnika w warstwie (klastrów). Wraz z dalszym wzrostem stężenia PC dochodzi do wzrostu rozmiarów inkluzji, co w konsekwencji prowadzi do utworzenia ciągłej warstwy PC. Wnioski te zostały także potwierdzone badaniami za pomocą mikroskopii elektronowej oraz mikroskopii konfokalnej (w trybie materiałowym oraz fluorescencyjnym).

Wykonane zostały również badania optyczne i elektryczne wytworzonych warstw mieszanych. Zgodnie z oczekiwaniami, zaobserwowano wzrost wartości rezystancji powierzchniowej oraz transmitancji w zakresie UV-Vis wraz ze wzrostem stężenia barwnika w warstwach. Na podstawie zależności rezystancji powierzchniowej od stężenia MWCNT wyznaczono progi perkolacji elektrycznej. Wykazano, że stosując metody Langmuira do wytworzenia warstw możliwe jest względnie łatwe wyznaczenie progów perkolacji wyrażonych za pomocą trzech różnych jednostek tj.: ułamka masowego, ułamka powierzchniowego oraz gęstości powierzchniowej materiału przewodzącego. W przypadku innych metod, wyznaczenie progów perkolacji wyrażonego jako ułamek powierzchniowy może być niezwykle skomplikowane lub niemożliwe zwłaszcza, gdy trudno jest odróżnić materiały wchodzące w skład warstwy na podstawie obrazów uzyskanych za pomocą mikroskopii optycznej. Problem ten jednak nie występuje w zastosowanej przez nas metodzie.

W pracy [Rytel Electr 2016] postanowiono wykorzystać warstwy MWCNT do poprawy parametrów pracy ogniwa litowo-jonowego. W tym celu zbadano wpływ cienkiej warstwy MWCNT modyfikującej kolektor prądowy na podstawowe parametry pracy ogniwa. Baterie litowo-jonowe są powszechnie wykorzystywane do zasilania większości urządzeń mobilnych. Swoją komercyjny sukces zawdzięczają w głównej mierze wysokiej pojemności w stosunku masy własnej oraz wysokiej gęstości prądu wyładowania. Niestety, w większości przypadków wzrost gęstości prądu ładowania lub wyładowania powoduje obniżenie pojemności baterii. Dodatkowo zbyt wysokie prądy ładowania lub wyładowania mogą prowadzić do zapłonu baterii. Problemy te można częściowo wyeliminować poprzez redukcję oporów wewnętrznych urządzenia. Najprostszym sposobem na redukcję oporów wewnętrznych baterii jest zwiększenie ilości materiału przewodzącego w stosunku do masy aktywnej. Ze względu na to, że materiał przewodzący w katodzie nie bierze udziału w magazynowaniu energii, zwiększenie jego ilości powoduje niepotrzebny wzrost masy urządzenia. W ramach niniejszej pracy doktorskiej podjęto próbę rozwiązania tego problemu.

Jako materiał aktywny katody wybrano litowany tlenek manganu o strukturze spinelu (LiMn_2O_4) ze względu na to, że jest on szczególnie podatny na utratę pojemności wraz ze wzrostem gęstości prądu wyładowania oraz z grubością elektrody. Do modyfikacji kolektora prądowego wykorzystano MWCNT o rozkładzie statystycznym średnic w przedziale od 6 nm do 9 nm (Sigma-Aldrich). Modyfikację kolektora prądowego wykonano poprzez przeniesienie warstwy MWCNT z granicy faz woda-powietrze na folię aluminiową za pomocą metody Langmuira-Schaefera (LS) oraz metody stemplowej (S). Biorąc pod uwagę stężenie zawiesiny MWCNT oraz powierzchnię zajmowaną przez warstwę w momencie transferu na podłoże stałe, oszacowano jej gęstość powierzchniową na mniej niż $1 \mu\text{g cm}^{-2}$.

Dla zbadania wpływu wykonanej modyfikacji na parametry pracy ogniwa, przygotowano kilka katod o gęstości powierzchniowej pokrycia masą aktywną w przedziale od $1,3 \text{ mg cm}^{-2}$ do $12,7 \text{ mg cm}^{-2}$. Następnie, przygotowano ogniwa ze zmodyfikowanym kolektorem prądowym, których załadunek masy wynosił $7,1 \text{ mg cm}^{-2}$ dla metody LS i $6,7$ dla metody S. Należy w tym miejscu podkreślić, że masa MWCNT jest zanedbywalnie mała w porównaniu do masy aktywnej ogniwa.

Wszystkie badania otrzymanych katod wykonano w układzie dwuelektrodowym w odniesieniu do litu metalicznego. W pierwszym etapie, wykonano badania chronopotencjometryczne dla gęstości prądu w przedziale od 30 mA g⁻¹ do 400 mA g⁻¹. Analiza porównawcza otrzymanych wyników wykazała, że potencjał pracy ogniwa względem litu metalicznego w przypadku zastosowania kolektora zmodyfikowanego metodą LS nie uległ zmianie, natomiast w przypadku modyfikacji S uległ niewielkiemu wzrostowi. Ponadto, zaobserwowano wzrost potencjału pracy ogniwa pomimo nieznacznie większego załadunku masy aktywnej. Następnie, na podstawie profili wyładowania obliczono pojemności właściwe otrzymanych ogniw. Dla gęstości prądów wyładowania mniejszych niż 200 mA g⁻¹ nie zaobserwowano znaczących różnic pomiędzy ogniwami referencyjnymi, a zmodyfikowanym. Modyfikacje ogniw okazały się skuteczne dopiero dla gęstości prądu wynoszącej 400 mA g⁻¹ powodując wzrost pojemności właściwych o 18% i 33%, odpowiednio dla modyfikacji LS i S względem ogniwa o podobnym załadunku masy aktywnej. Dodatkową zaletą wprowadzonych modyfikacji był wzrost energii zgromadzonej w ogniwach, podczas cyklu ładowania względem pozostałych badanych ogniw.

W celu wyjaśnienia przyczyn poprawy parametrów pracy zmodyfikowanych ogniw wykonano badania za pomocą spektroskopii impedancyjnej. Powodem poprawy parametrów pracy ogniw było w głównej mierze obniżenie wartości rezystancji przeniesienia ładunku. Obniżenie wartości tego parametru umożliwiło bardziej wydajną migrację jonów litu do wewnętrznej części elektrody.

5. Podsumowanie i wnioski

Przedmiotem badań, w ramach niniejszej rozprawy doktorskiej, były warstwy nanomateriałów węglowych na granicy faz woda-powietrze oraz na podłożach stałych. Badania miały na celu obniżenie rezystancji powierzchniowej warstw oraz zwiększenie ich transmitancji w zakresie UV-Vis. Na podstawie wyników badań określono, jak wybrane elementy procesu przygotowania i kompozycji warstw wpływają na ich właściwości optyczne, mechaniczne i elektryczne oraz pokazano możliwość zastosowania warstw z nanomateriałów węglowych w ogniwach litowo-jonowych.

Najważniejszymi osiągnięciami wynikającymi z przeprowadzonych badań są:

- zwiększenie pojemności właściwych ogniw litowo-jonowych poprzez modyfikację kolektorów prądowych warstwą MWCNT;
- wykazanie, że wzrost pojemności właściwych ogniw litowo-jonowych spowodowany był obniżeniem ich rezystancji wewnętrznych;
- pokazanie, że zastosowanie zbyt dużej mocy ultradźwięków podczas przygotowania zawiesiny wpływa na zmianę hybrydyzacji wiązań C-C w płatkach grafenowych;
- wykazanie, że konieczne jest poszerzenie analizy widm rozproszenia Ramana o wyznaczenie stosunku pasm D' do D, w celu określenia jakości badanego grafenu;
- optymalizacja procesu homogenizacji zawiesiny nanomateriałów węglowych powodująca minimalizację wartości rezystancji powierzchniowej i maksymalizację wartości transmitancji w zakresie UV-Vis warstw MWCNT;
- określenie wpływu średnicy MWCNT na wartości rezystancji powierzchniowej i wartości transmitancji w zakresie UV-Vis badanych warstw;
- lepsze zrozumienie procesu porządkowania się MWCNT podczas procesu ich sprężania na granicy faz woda-powietrze;
- identyfikacja głównego czynnika uniemożliwiającego uzyskanie warstw MWCNT o wysokiej anizotropii elektrycznej ;
- identyfikacja czynników mających wpływ na położenie pasm π -plazmonowych warstw MWCNT;
- wykazanie możliwości poprawy transmitancji warstw MWCNT poprzez wprowadzenie dodatkowego składnika do ich struktury;
- określenie kierunku oraz wartości sił wzajemnych oddziaływań pomiędzy PC a MWCNT;
- wskazanie grup chemicznych, w strukturze molekularnej barwnika odpowiedzialnych za oddziaływanie PC z MWCNT;
- określenie wpływu oddziaływań pomiędzy MWCNT i PC na strukturę warstwy;
- wyznaczenie progów perkolacji elektrycznej dla warstw mieszanych MWCNT/PC;
- opracowanie metody wyznaczania ułamka powierzchniowego zajmowanego przez każdy ze składników warstwy;
- określenie wpływu stężenia barwnika na otrzymane wartości transmitancji i rezystancji powierzchniowej warstw.

Podsumowując, opisane w rozprawie doktorskiej badania i ich wyniki dostarczyły ważnych informacji na temat właściwości warstw utworzonych z nanomateriałów węglowych, które są szczególnie istotne z aplikacyjnego punktu widzenia. Wykazano praktyczną możliwość wykorzystania badanych warstw do poprawy parametrów pracy ogniw litowo-jonowych. Zrozumienie jaki wpływ ma procesu homogenizacji ultradźwiękowej na właściwości materiałów węglowych pozwoliło na optymalizację tego procesu. Podczas badań wykazano po raz pierwszy, że średnica MWCNT ma istotne znaczenie jako parametr determinujący właściwości warstw wytwarzanych z nanorurek. Lepsze zrozumienie procesu porządkowania MWCNT podczas ich kompresji na granicy faz woda-powietrze pozwoliło na wytyczenie nowych kierunków badań mających na celu zwiększenie anizotropii otrzymanych warstw. Natomiast, wyniki badań dotyczące wpływu PC na formowanie się warstw MWCNT pokazały nie tylko możliwość zwiększenia transmitancji otrzymanych warstw, ale też dostarczyły informacji pozwalających na zrozumienie oddziaływań pomiędzy barwnikiem i nanorurkami. Rozszerzenie możliwości analizy nadmiarowych energii Gibbsa dla materiałów o nieznannej masie molowej, pozwoli na zastosowanie jej do poszukiwania lepszych dyspersantów nanomateriałów, dla których szczególnie trudne jest określenie masy molowej. Dodatkowo, zaproponowana metoda określania ułamków powierzchniowych zajmowanych przez każdy ze składników mieszaniny w znaczącym stopniu ułatwi wyznaczanie progów perkolacji, co może przyczynić się do redukcji ilości zastosowanych nanomateriałów.

Literatura

- [1] D. Malko, C. Neiss, F. Viñes, A. Görling, Competition for graphene: Graphynes with direction-dependent dirac cones, *Phys. Rev. Lett.* 108 (2012) 1–4.
doi:10.1103/PhysRevLett.108.086804.
- [2] Y. Li, L. Xu, H. Liu, Y. Li, Graphdiyne and graphyne: From theoretical predictions to practical construction, *Chem. Soc. Rev.* 43 (2014) 2572–2586. doi:10.1039/c3cs60388a.
- [3] A. Wang, L. Li, X. Wang, H. Bu, M. Zhao, Graphyne-based carbon allotropes with tunable properties: From Dirac fermion to semiconductor, *Diam. Relat. Mater.* 41 (2014) 65–72.
doi:10.1016/j.diamond.2013.10.009.

- [4] S.Y. Lim, W. Shen, Z. Gao, Carbon quantum dots and their applications, *Chem. Soc. Rev.* 44 (2015) 362–381. doi:10.1039/c4cs00269e.
- [5] K. Harigaya, Electronic states of metallic and semiconducting carbon nanotubes with bond and site disorder, *Phys. Rev. B - Condens. Matter Mater. Phys.* 60 (1999) 1452–1455. doi:10.1103/PhysRevB.60.1452.
- [6] H. Suzuura, T. Ando, Chirality-dependent resistivity in carbon nanotubes, *Mol. Cryst. Liq. Cryst. Sci. Technol. Sect. A Mol. Cryst. Liq. Cryst.* 340 (2000) 731–736. doi:10.1080/10587250008025555.
- [7] A. Takakura, K. Beppu, T. Nishihara, A. Fukui, T. Kozeki, T. Namazu, et al., Strength of carbon nanotubes depends on their chemical structures, *Nat. Commun.* 10 (2019) 1–7. doi:10.1038/s41467-019-10959-7.
- [8] Y. Murakami, E. Einarsson, T. Edamura, S. Maruyama, Polarization dependent optical absorption properties of single-walled carbon nanotubes and methodology for the evaluation of their morphology, *Carbon N. Y.* 43 (2005) 2664–2676. doi:10.1016/j.carbon.2005.05.036.
- [9] P.L. A. Lucas, L. Henrard, Computation of the ultraviolet absorption and electron inelastic scattering cross section of multishell fullerenes, *Phys. Rev. B - Condens. Matter Mater. Phys.* 49 (1994) 2888–2896. doi:10.1103/PhysRevB.49.2888.
- [10] G.A. Rance, D.H. Marsh, R.J. Nicholas, A.N. Khlobystov, UV-vis absorption spectroscopy of carbon nanotubes: Relationship between the π -electron plasmon and nanotube diameter, *Chem. Phys. Lett.* 493 (2010) 19–23. doi:10.1016/j.cplett.2010.05.012.
- [11] G. Rajasekaran, P. Narayanan, A. Parashar, Effect of Point and Line Defects on Mechanical and Thermal Properties of Graphene: A Review, *Crit. Rev. Solid State Mater. Sci.* 41 (2016) 47–71. doi:10.1080/10408436.2015.1068160.
- [12] M. Carbone, L. Gorton, R. Antiochia, An overview of the latest graphene-based sensors for glucose detection: The effects of graphene defects, *Electroanalysis.* 27 (2015) 16–31. doi:10.1002/elan.201400409.

- [13] T. Xu, L. Sun, Structural defects in graphene, *Defects Adv. Electron. Mater. Nov. Low Dimens. Struct.* 5 (2018) 137–160. doi:10.1016/B978-0-08-102053-1.00005-3.
- [14] J.A. Garlow, L.K. Barrett, L. Wu, K. Kisslinger, Y. Zhu, J.F. Pulecio, Large-Area Growth of Turbostratic Graphene on Ni(111) via Physical Vapor Deposition, *Sci. Rep.* 6 (2016) 1–11. doi:10.1038/srep19804.
- [15] J.M.B. Lopes Dos Santos, N.M.R. Peres, A.H. Castro Neto, Graphene bilayer with a twist: Electronic structure, *Phys. Rev. Lett.* 99 (2007) 19–22. doi:10.1103/PhysRevLett.99.256802.
- [16] Q. Zhao, M.B. Nardelli, J. Bernholc, Ultimate strength of carbon nanotubes: A theoretical study, *Phys. Rev. B - Condens. Matter Mater. Phys.* 65 (2002) 1–6. doi:10.1103/PhysRevB.65.144105.
- [17] B.G. Sidharth, A. Das, Ballistic transport in carbon nanotubes, *Spacetime Energy A Twenty First Century Perspect.* 323 (2019) 81–87.
- [18] A.S. Mayorov, R. V. Gorbachev, S. V. Morozov, L. Britnell, R. Jalil, L.A. Ponomarenko, et al., Micrometer-scale ballistic transport in encapsulated graphene at room temperature, *Nano Lett.* 11 (2011) 2396–2399. doi:10.1021/nl200758b.
- [19] K.T. Lee, D.H. Park, H.W. Baac, S. Han, Graphene- and carbon-nanotube-based transparent electrodes for semitransparent solar cells, *Materials (Basel)*. 11 (2018) 1503–1523. doi:10.3390/ma11091503.
- [20] F.J. Sonia, M. Aslam, A. Mukhopadhyay, Understanding the processing-structure-performance relationship of graphene and its variants as anode material for Li-ion batteries: A critical review, *Carbon N. Y.* 156 (2020) 130–165. doi:10.1016/j.carbon.2019.09.026.
- [21] P. Sehrawat, C. Julien, S.S. Islam, Carbon nanotubes in Li-ion batteries: A review, *Mater. Sci. Eng. B Solid-State Mater. Adv. Technol.* 213 (2016) 12–40. doi:10.1016/j.mseb.2016.06.013.
- [22] Q. Cao, Carbon nanotube transistor technology for More-Moore scaling, *Nano Res.* 14

- (2021) 3051–3069. doi:10.1007/s12274-021-3459-z.
- [23] D.R. Kauffman, A. Star, Graphene versus carbon nanotubes for chemical sensor and fuel cell applications, *Analyst*. 135 (2010) 2790–2797. doi:10.1039/c0an00262c.
- [24] F. Schwierz, Graphene transistors, *Nat. Nanotechnol.* 5 (2010) 487–496. doi:10.1038/nnano.2010.89.
- [25] S. Xu, L. Zhang, B. Wang, R.S. Ruoff, Chemical vapor deposition of graphene on thin-metal films, *Cell Reports Phys. Sci.* 2 (2021) 100372. doi:10.1016/j.xcrp.2021.100372.
- [26] Q. Zhang, N. Wei, P. Laiho, E.I. Kauppinen, Recent Developments in Single-Walled Carbon Nanotube Thin Films Fabricated by Dry Floating Catalyst Chemical Vapor Deposition, *Top. Curr. Chem.* 375 (2017) 1–30. doi:10.1007/s41061-017-0178-8.
- [27] M.K. Massey, C. Pearson, D.A. Zeze, B.G. Mendis, M.C. Petty, The electrical and optical properties of oriented Langmuir-Blodgett films of single-walled carbon nanotubes, *Carbon N. Y.* 49 (2011) 2424–2430. doi:10.1016/j.carbon.2011.02.009.
- [28] S. Kang, K. Lim, H. Park, J.B. Park, S.C. Park, S.P. Cho, et al., Roll-to-Roll Laser-Printed Graphene-Graphitic Carbon Electrodes for High-Performance Supercapacitors, *ACS Appl. Mater. Interfaces*. 10 (2018) 1033–1038. doi:10.1021/acsami.7b13741.
- [29] S. Zhang, B.E. Leonhardt, N. Nguyen, A. Oluwalowo, C. Jolowsky, A. Hao, et al., Roll-to-roll continuous carbon nanotube sheets with high electrical conductivity, *RSC Adv.* 8 (2018) 12692–12700. doi:10.1039/c8ra01212a.
- [30] D. Jamwal, R.K. Gupta, A. Khosla, R. Vaid, Spin-coated single walled carbon nanotubes confirms p–n junction diode behavior, *Microsyst. Technol.* 24 (2018) 4211–4215. doi:10.1007/s00542-018-3713-9.
- [31] Z. Qingbin, I. Wai Hing, L. Xiuyi, Y. Nariman, Y. Kan Kan, L. Zhigang, et al., Transparent conductive films consisting of ultralarge graphene sheets produced by Langmuir-Blodgett assembly, *ACS Nano*. 5 (2011) 6039–6051. doi:10.1021/nn2018683.
- [32] N.S. Struchkov, E. V. Alexandrov, A. V. Romashkin, G.O. Silakov, M.K. Rabchinskii,

Uniform graphene oxide films fabrication via spray-coating for sensing application, Fullerenes Nanotub. Carbon Nanostructures. 28 (2020) 214–220. doi:10.1080/1536383X.2019.1686623.

- [33] X. Zhou, A.M. Cao, L.J. Wan, Y.G. Guo, Spin-coated silicon nanoparticle/graphene electrode as a binder-free anode for high-performance lithium-ion batteries, Nano Res. 5 (2012) 845–853. doi:10.1007/s12274-012-0268-4.
- [34] Q. Zheng, L. Shi, P.C. Ma, Q. Xue, J. Li, Z. Tang, et al., Structure control of ultra-large graphene oxide sheets by the Langmuir-Blodgett method, RSC Adv. 3 (2013) 4680–4691. doi:10.1039/c3ra22367a.
- [35] K. Kędzierski, K. Rytel, Ł. Majchrzycki, D. Wróbel, Conductive and transparent films of oriented multi-walled carbon nanotubes by Langmuir-Schaefer method, Thin Solid Films. 589 (2015) 701–706 . doi:10.1016/j.tsf.2015.06.050.
- [36] L. Jia, Y. Zhang, J. Li, C. You, E. Xie, Aligned single-walled carbon nanotubes by Langmuir-Blodgett technique, J. Appl. Phys. 104 (2008) 074318–6. doi:10.1063/1.2996033.

Dorobek naukowy

Publikacje naukowe (* – autor korespondencyjny, IF – Impact Factor):

1. K. Kędzierski*, K. Rytel, Ł. Majchrzycki, D. Wróbel, Conductive and transparent films of oriented multi-walled carbon nanotubes by Langmuir-Schaefer method, Thin Solid Films 589 (2015) 701-706 [IF 2,183]
2. K. Rytel, D. Waszak, K. Kędzierski, D. Wróbel*, Novel method of current collector coating by multiwalled carbon nanotube Langmuir layer for enhanced power performance of LiMn_2O_4 electrode of Li-ion batteries, Electrochimica Acta 222 (2016) 921–925 [IF 6,901]

3. K. Kędzierski*, **K. Rytel**, B. Barszcz, A. Gronostaj, Ł. Majchrzycki, D. Wróbel, On the temperature dependent electrical resistivity of CNT layers in view of Variable Range Hopping models, *Organic Electronics*, 43 (2017) 253-261 [IF 3,721]
4. B. Bursa*, **K. Rytel**, M. Skrzypiec, K. Prochaska, D. Wróbel, Thin film of CdTeSe/ZnS quantum dots on water subphase: Thermodynamics and morphology studies, *Dyes and Pigments*, 155 (2018) 36-41 [IF 4,889]
5. **K. Rytel***, M. Widelicka, D. Łukawski, F. Lisiecki, K. Kędzierski, D. Wróbel, Ultrasonication-induced sp³ hybridization defects in Langmuir–Schaefer layers of turbostratic graphene, *Physical Chemistry Chemical Physics*, 20 (2018) 12777-12784, [IF 3,676]
6. K. Kędzierski*, **K. Rytel**, B. Barszcz, A. Gronostaj, Ł. Majchrzycki, D. Wróbel, Unusual conductivity temperature dependence of multiwalled carbon nanotube thin film, *Chemical Physics Letters*, 712 (2018) 144–148, [IF 2,328]
7. Kertmen, E. Barbé, M. Szkoda, K. Siuzdak, V. Babacic, P. Torruella, I. Iatsunskyi, M. Kotkowiak, **K. Rytel**, S. Estradé, F. Peiró, S. Jurga, Y. Li, E. Coy, Photoelectrochemically active N-adsorbing ultrathin TiO₂ layers for water-splitting applications prepared by pyrolysis of oleic acid on iron oxide nanoparticle surfaces under nitrogen environment, *Advanced Materials Interfaces*, 1801286 (2018) 1-10 [IF 6,147]
8. A. Biadasz*, **K. Rytel**, K. Kędzierski, A. Adamski, M. Kotkowiak, A. Stachowiak, B. Barszcz, H. Y. Jeong, T. Kim, The liquid crystal induced J-type aggregation of diketopyrrolopyrrole derivatives in monolayer, *Journal of Molecular Liquids*, 285 (2019) 598–606 [IF 6,165]
9. **K. Rytel***, K. Kędzierski, B. Barszcz, M. Widelicka, A. Stachowiak, A. Biadasz, Ł. Majchrzycki, E. Coy, D. Wróbel, The influence of diameter of multiwalled carbon nanotubes

on mechanical, optical and electrical properties of Langmuir-Schaefer films, *Physical Chemistry Chemical Physics*, 39 (2020) 22380–22389 [IF 3,676]

10. B. Barszcz*, T. N. Starodub, A. Mizera, R. Świetlik, **K. Rytel**, V. O. Iaroshenko, V. A. Starodub, Structure, optical and electro-physical properties of tetramerized anion-radical salt (N-Xy-Qn)(TCNQ)₂, *Spectrochimica Acta Part A*, 270 (2022) 120822-120834 [IF 4,098]
11. **K. Rytel***, K. Kędziński, B. Barszcz, A. Biadasz, Ł. Majchrzycki, D. Wróbel, The influence of zinc phthalocyanine on the formation and properties of multiwalled carbon nanotubes thin films on the air–solid and air–water interface, *Journal of Molecular Liquids*, 350 (2022) 118548–118555 [IF 6,165]

Rozdziały w monografiach naukowych:

1. D. Łukawski, **K. Rytel**, W. Grześkowiak, F. Lisiecki, A. Dudkowiak, Grafen, nanorurki węglowe i ich zastosowanie w ochronie przed ogniem, w: *Innowacje w polskiej nauce w obszarze nauk technicznych, Przegląd aktualnej tematyki badawczej*, red. J. Doskocz, T. Janiczek, Wydawnictwo Nauka i Biznes 2016, s. 116-125, ISBN: 978-83-947095-4-9

Zgłoszenia patentowe

1. D. Łukawski, A. Martin, **K. Rytel**, P.439007, Sposób wytworzenia podgrzewanej drewnopochodnej płyty meblowej.
2. A. Biadasz, D. Łukawski, **K. Rytel**, K. Kędziński, M. Kotkowiak, P.440689, Układ przesyłu gazu o kontrolowanej wilgotności.

Inne osiągnięcia naukowe:

a) Kierowanie grantami badawczymi:

1. Preludium, NCN, 2017-2021, 2016/21/N/ST8/03557, Opracowanie metod otrzymywania transparentnych elektrod na bazie nanorurek węglowych i grafenu technikami Langmuira,

2. DSMK, 2018, 06/62/DSMK/6204, Warstwy Langmuira-Schaefera nanorurek węglowych wzbogacone sferycznymi nanocząstkami srebra.

b) Uczestnictwo w grantach badawczych:

1. Tango, NCBR, 2020-2021, TANGO-IV-A/0014/2019-00, Opracowanie technologii wytwarzania mebli drewnianych z funkcją grzania z wykorzystaniem technologii cienkowarstwowych
2. DSMK, 2016, 06/62/DSMK/0199, Warstwy Langmuira na granicy faz ciekły gal – powietrze, wykonawca
3. DSMK, 2019, 06/62/DSMK/62507, Badanie właściwości struktury elektronowej wybranych barwników ftalocyjaninowych w postaci roztworów i cienkich warstw, wykonawca

c) Staże naukowe:

1. Instytut Metali Nieżelaznych oddział w Poznaniu, Centralne Laboratorium Akumulatorów i Ogniw, 2014 (12 miesięcy)
2. Prevac sp. z o.o., Rogów, 2013 (1 miesiąc)

d) Prezentacja wyników na konferencjach /sympoziach/ warsztatach naukowych

1. D. Waszak, **K. Rytel**, M. Walkowiak, K. Wasiński, P. Pórolniczak, D. Wróbel, K. Kędzierski, A. Czerwiński, B. Hamankiewicz, Aluminum current collector for Li-ion batteries modified with monolayer of carbon nanotubes, Challenges in Chemical Renewable Energy, Rio de Janeiro, Brazylia, 2015 – **plakat**
2. D. Łukawski, **K. Rytel**, A. Dudkowiak, Wpływ ultra-cienkich warstw węglowych na palność polimerów, II KK Grafen2D, Szczecin, 2016 – **plakat**
3. K. Rytel, D. Waszak, K. Kędzierski, D. Wróbel, Modyfikacje powierzchni kolektora prądowego warstwami Langmuira wielościennych nanorurek węglowych w ogniwach litowo-jonowych, XX Ogólnopolska Konferencja Krysztaly Molekularne, Kazimierz Dolny, 2016 – **wystąpienie ustne**

4. K. Kędzierski, K. Rytel, Ł. Majchrzycki, Warstwy Langmuira-Schaefera jednościennych nanorożków węglowych, Ogólnopolska Konferencja Kryształy Molekularne, Kazimierz Dolny, 2016 – **plakat**
5. **K. Rytel**, B. Barszcz, K. Kędzierski, A. Gronostaj, Badanie przewodnictwa elektrycznego w funkcji temperatury warstw Langmuira nanorurek węglowych na podłożach z polichloroku winylu, Kazimierz Dolny, 2016 – **plakat**
6. **K. Rytel**, B. Barszcz, K. Kędzierski, K. Szulc, Warstwy Langmuira na granicy faz ciekły gal-powietrze, XV OSKNF, Poznań 2016 – **plakat**
7. **K. Rytel**, B. Barszcz, K. Kędzierski, A. Gronostaj, Badanie przewodnictwa elektrycznego w funkcji temperatury warstw Langmuira nanorurek węglowych na podłożach z polichloroku winylu, Doktoranckie Sympozjum Nanotechnologii NanoMat, Łódź, 2017 – **plakat**
8. M. Widelicka, **K. Rytel**, D. Łukawski, K. Kędzierski, D. Lisiecki, Badanie wpływu sonikacji grafenu na formowanie się warstw Langmuira, Doktoranckie Sympozjum Nanotechnologii NanoMat, Łódź, 2017 – **plakat**
9. **K. Rytel**, P. Błaszkiwicz, M. Widelicka, Warstwy Langmuira-Schaefera nanorurek węglowych wzbogacone sferycznymi nanocząstkami srebra, IV Konferencja Kryształki Molekularne, Łódź, 2017 – **plakat**
10. K. Kędzierski, **K. Rytel**, B. Barszcz, A. Gronostaj, Ł. Majchrzycki, D. Wróbel, Electrical conductivity of carbon nanotube thin films, 13th Interregional Workshop on Advanced Nanomaterials, Poznań, 2017 – **plakat**
11. **K. Rytel**, B. Barszcz, K. Kędzierski, D. Wróbel, Properties and application of carbon nanotube Langmuir-Schaefer thin films, XII Copernican International Young Scientists Conference, Toruń, 2018 – **plakat**
12. **K. Rytel**, M. Widelicka, D. Łukawski, F. Lisiecki, K. Kędzierski, D. Wróbel, Ultrasonication induced sp^3 hybridization defects in Langmuir-Schaefer layers of turbostratic graphene, XII Copernican International Young Scientists Conference, Toruń, 2018 – **plakat**
13. K. Kędzierski, **K. Rytel**, D. Wróbel, Cienkie warstwy układów hybrydowych nanorurka węglowa-barwnik organiczny, XXI Kryształy Molekularne, Łódź-Kolumna, 2018 – **plakat**
14. **K. Rytel**, B. Barszcz, K. Kędzierski, D. Wróbel, Properties and application of carbon nanotube Langmuir-Schaefer thin films, 19th International Conference on the Science and Application of Nanotubes and Low-Dimensional Materials, Pekin, Chiny, 2018 – **plakat**

15. **K. Rytel**, M. Widelicka, D. Łukawski, K. Kędzierski, F. Lisiecki, Defekty o hybrydyzacji sp^3 indukowane ultrasonikacją w warstwach grafenu turbostratycznego otrzymanych metodą Langmuira-Schaefera, III Ogólnopolska Studencka Fizyczno-Optyczna Konferencja FOKA, Wrocław, 2018 – **wystąpienie ustne**
16. M. Ziółkowski, K. Kędzierski, **K. Rytel**, Cienkie warstwy układów hybrydowych nanorurka węglowa-barwnik organiczny, III Ogólnopolska Studencka Fizyczno-Optyczna Konferencja FOKA, Wrocław, 2018 – **plakat**
17. **K. Rytel**, M. Widelicka, K. Kędzierski, Defekty o hybrydyzacji sp^3 indukowane ultrasonikacją w warstwach grafenu turbostratycznego otrzymanych metodą Langmuira-Schaefera, V Ogólnopolska Konferencja Kryształki Molekularne, Łódź, 2019 – **wystąpienie ustne**
18. **K. Rytel**, K. Kędzierski, B. Barszcz, M. Ziółkowski, Właściwości i zastosowania cienkich warstw nanorurek węglowych otrzymanych metodą Langmuira-Schaefera, V Ogólnopolska Konferencja Kryształki Molekularne, Łódź, 2019 – **plakat**
19. **K. Rytel**, K. Kędzierski, B. Barszcz, M. Widelicka, M. Ziółkowski, Wpływ średnicy wielościennych nanorurek węglowych na właściwości mechaniczne elektryczne i optyczne warstw Langmuira-Schaefera, V Ogólnopolska Konferencja Kryształki Molekularne, Łódź, 2019 – **plakat**
20. K. Kędzierski, **K. Rytel**, Mechanizmy transportu ładunku w cienkich warstwach nanorurek węglowych, V Ogólnopolska Konferencja Kryształki Molekularne, Łódź, 2019 – **plakat**

Załączniki

Oświadczenia współautorów o wkładzie w publikacje naukowe doktoranta

Poznań, dnia 04.04.2022

prof. dr hab. Danuta Wróbel

Oświadczenie

Oświadczam, że w niniejszych publikacjach:

K. Rytel, M. Widelicka, D. Łukawski, F. Lisiecki, K. Kędziński, D. Wróbel, Ultrasonication-induced sp^3 hybridization defects in Langmuir-Schaefer layers of turbostratic graphene, Phys. Chem. Chem. Phys. 20 (2018) 12777–12784.

K. Rytel, K. Kędziński, B. Barszcz, M. Widelicka, A. Stachowiak, A. Biadasz, Ł. Majchrzycki, E. Coy, D. Wróbel, The influence of diameter of multiwalled carbon nanotubes on mechanical, optical and electrical properties of Langmuir-Schaefer films, Phys. Chem. Chem. Phys. 22 (2020) 22380–22389

K. Rytel, K. Kędziński, B. Barszcz, B. Biadasz, Ł. Majchrzycki, D. Wróbel, The influence of zinc phthalocyanine on the formation and properties of multiwalled carbon nanotubes thin films on the air-solid and air-water interface, J. Mol. Liq. 350 (2022) 118548

K. Rytel, D. Waszak, K. Kędziński, D. Wróbel, Novel method of current collector coating by multiwalled carbon nanotube Langmuir layer for enhanced power performance of LiMn₂O₄ electrode of Li-ion batteries, Electrochim. Acta. 222 (2016) 921–925.

mój udział polegał na nadzorowaniu prac badawczych, analizie i dyskusji końcowej wersji manuskryptu oraz pracach redakcyjnych.

Wyrażam zgodę na przedłożenie ww. pracy przez mgr. inż. Karol Rytla jako część rozprawy doktorskiej w formie zbioru opublikowanych i powiązanych tematycznie artykułów naukowych.



(podpis współautora)

Poznań, dnia 04.04.2022

dr hab. inż. Emerson Coy

Oświadczenie

Oświadczam, że w niniejszej publikacji:

*K. Rytel, K. Kędzierski, B. Barszcz, M. Widelicka, A. Stachowiak, A. Biadasz, Ł. Majchrzycki, E. Coy, D. Wróbel, The influence of diameter of multiwalled carbon nanotubes on mechanical, optical and electrical properties of Langmuir-Schaefer films, **Physical Chemistry Chemical Physic**, 39 (2020) 22380–22389*

mój udział polegał na wykonaniu pomiarów TEM oraz ich analizie.

Wyrażam zgodę na przedłożenie ww. pracy przez mgr. inż. Karol Rytla jako część rozprawy doktorskiej w formie zbioru opublikowanych i powiązanych tematycznie artykułów naukowych.

Declaration

I declare that in this publication:

*K. Rytel, K. Kędzierski, B. Barszcz, M. Widelicka, A. Stachowiak, A. Biadasz, Ł. Majchrzycki, E. Coy, D. Wróbel, The influence of diameter of multiwalled carbon nanotubes on mechanical, optical and electrical properties of Langmuir-Schaefer films, **Physical Chemistry Chemical Physic**, 39 (2020) 22380–22389*

my contribution consisted in making TEM measurements and their analysis.

I agree to submit the above work by Karol Rytel, as a part of the Ph.D. dissertation in the form of a collection of published and thematically related scientific articles.



(podpis współautora)
(co-author's signature)

Poznań, dnia 04.04.2022

dr inż. Bolesław Barszcz

Instytut Fizyki Molekularnej Polskiej Akademii Nauk
ul. Mariana Smoluchowskiego 17, 60-179 Poznań

Oświadczenie

Oświadczam, że w niniejszych publikacjach:

1. K. Rytel, K. Kędzierski, B. Barszcz, M. Widelicka, A. Stachowiak, A. Biadasz, Ł. Majchrzycki, E. Coy, D. Wróbel, The influence of diameter of multiwalled carbon nanotubes on mechanical, optical and electrical properties of Langmuir-Schaefer films, **Physical Chemistry Chemical Physic**, 39 (2020) 22380–22389

2. K. Rytel, K. Kędzierski, B. Barszcz, A. Biadasz, Ł. Majchrzycki, D. Wróbel, The influence of zinc phthalocyanine on the formation and properties of multiwalled carbon nanotubes thin films on the air–solid and air–water interface, **Journal of Molecular Liquids**, 350 (2022) 118548–118555

mój udział polegał na:

ad 1. Zarejestrowaniu widm rozpraszania ramanowskiego, obróbce uzyskanych wyników i częściowej ich interpretacji. Ponadto uczestniczyłem w dyskusji wyników uzyskanych innymi technikami oraz brałem udział w przygotowaniu tekstu artykułu.

ad 2. Dyskusji i częściowej analizie uzyskanych wyników. Ponadto brałem udział w przygotowaniu tekstu artykułu.

Wyrażam zgodę na przedłożenie ww. prac przez mgr. inż. Karola Rytla jako część rozprawy doktorskiej w formie zbioru opublikowanych i powiązanych tematycznie artykułów naukowych.



(podpis współautora)

Poznań, dnia 04.04.2022

dr inż. Andrzej Michał Biadasz
Instytut Fizyki
Politechnika Poznańska
ul. Piotrowo 3
60-965 Poznań
andrzej.biadasz@put.poznan.pl

Oświadczenie

Oświadczam, że w niniejszych publikacjach:

K. Rytel, K. Kędzierski, B. Barszcz, M. Widelicka, A. Stachowiak, A. Biadasz, Ł. Majchrzycki, E. Coy, D. Wróbel, The influence of diameter of multiwalled carbon nanotubes on mechanical, optical and electrical properties of Langmuir-Schaefer films, Phys. Chem. Chem. Phys. 22 (2020) 22380–22389.

K. Rytel, K. Kędzierski, B. Barszcz, B. Biadasz, Ł. Majchrzycki, D. Wróbel, The influence of zinc phthalocyanine on the formation and properties of multiwalled carbon nanotubes thin films on the air-solid and air-water interface, J. Mol. Liq. 350 (2022) 118548.

Mój udział polegał na pomocy w analizie danych z warstw Langmuira.

Wyrażam zgodę na przedłożenie ww. pracy przez mgr. inż. Karol Rytla jako część rozprawy doktorskiej w formie zbioru opublikowanych i powiązanych tematycznie artykułów naukowych.



(podpis współautora)

Poznań, dnia 12.04.2022

dr inż. Kamil Kędzierski

Oświadczenie

Oświadczam, że w niniejszych publikacjach:

K. Rytel, M. Widelicka, D. Łukawski, F. Lisiecki, K. Kędzierski, D. Wróbel, Ultrasonication-induced sp^3 hybridization defects in Langmuir-Schaefer layers of turbostratic graphene, Phys. Chem. Chem. Phys. 20 (2018) 12777–12784. doi:10.1039/c8cp01363b.

K. Rytel, K. Kędzierski, B. Barszcz, M. Widelicka, A. Stachowiak, A. Biadasz, Ł. Majchrzycki, E. Coy, D. Wróbel, The influence of diameter of multiwalled carbon nanotubes on mechanical, optical and electrical properties of Langmuir-Schaefer films, Phys. Chem. Chem. Phys. 22 (2020) 22380–22389. doi:10.1039/d0cp03687k.

K. Rytel, K. Kędzierski, B. Barszcz, B. Biadasz, Ł. Majchrzycki, D. Wróbel, The influence of zinc phthalocyanine on the formation and properties of multiwalled carbon nanotubes thin films on the air-solid and air-water interface, J. Mol. Liq. 350 (2022)

K. Rytel, D. Waszak, K. Kędzierski, D. Wróbel, Novel method of current collector coating by multiwalled carbon nanotube Langmuir layer for enhanced power performance of LiMn₂O₄ electrode of Li-ion batteries, Electrochim. Acta. 222 (2016) 921–925. doi:10.1016/j.electacta.2016.11.058.

mój własny wkład merytoryczny w przygotowanie, przeprowadzenie i opracowanie badań oraz przedstawienie prac w formie publikacji to asysta przy wykonywaniu cienkich warstw nanostruktur węglowych oraz uczestnictwo w analizie otrzymanych wyników i redagowaniu manuskryptów.

Wyrażam zgodę na przedłożenie ww. pracy przez mgr. inż. Karol Rytla jako część rozprawy doktorskiej w formie zbioru opublikowanych i powiązanych tematycznie artykułów naukowych.

Kamil Kędzierski

(podpis współautora)

Poznań, dnia 04.04.2022

dr inż. Damian Łukawski

Oświadczenie

Oświadczam, że w niniejszej publikacji:

*K. Rytel, M. Widelicka, D. Łukawski, F. Lisiecki, K. Kędziński, D. Wróbel, Ultrasonication-induced sp^3 hybridization defects in Langmuir-Schaefer layers of turbostratic graphene, **Physical Chemistry Chemical Physics**, 20 (2018) 12777–12784*

mój udział polegał na przygotowaniu części próbek oraz współpracy przy dyskusji wyników.

Wyrażam zgodę na przedłożenie ww. pracy przez mgr. inż. Karol Rytla jako część rozprawy doktorskiej w formie zbioru opublikowanych i powiązanych tematycznie artykułów naukowych.

Damian Łukawski
.....

(podpis współautora)

Poznań, dnia 04.04.2022

dr inż. Filip Lisiecki

Oświadczenie

Oświadczam, że w niniejszej publikacji:

*K. Rytel, M. Widelicka, D. Łukawski, F. Lisiecki, K. Kędzierski, D. Wróbel, Ultrasonication-induced sp^3 hybridization defects in Langmuir-Schaefer layers of turbostratic graphene, **Physical Chemistry Chemical Physics**, 20 (2018) 12777–12784*

mój udział polegał na wykonaniu zdjęć próbek przy pomocy skaningowego mikroskopu elektronowego (SEM).

Wyrażam zgodę na przedłożenie ww. pracy przez mgr. inż. Karol Rytla jako część rozprawy doktorskiej w formie zbioru opublikowanych i powiązanych tematycznie artykułów naukowych.

Lisiecki Filip.....

(podpis współautora)

Poznań, dnia 04.04.2022

dr inż. Łukasz Majchrzycki

Oświadczenie

Oświadczam, że w niniejszych publikacjach:

K. Rytel, K. Kędziński, B. Barszcz, M. Widelicka, A. Stachowiak, A. Biadasz, Ł. Majchrzycki, E. Coy, D. Wróbel, The influence of diameter of multiwalled carbon nanotubes on mechanical, optical and electrical properties of Langmuir-Schaefer films, Phys. Chem. Chem. Phys. 22 (2020) 22380–22389. doi:10.1039/d0cp03687k.

K. Rytel, K. Kędziński, B. Barszcz, B. Biadasz, Ł. Majchrzycki, D. Wróbel, The influence of zinc phthalocyanine on the formation and properties of multiwalled carbon nanotubes thin films on the air-solid and air-water interface, J. Mol. Liq. 350 (2022)

mój udział polegał na obrazowaniu materiałów z wykorzystaniem Skaningowej Mikroskopii Elektronowej.

Wyrażam zgodę na przedłożenie ww. pracy przez mgr. inż. Karol Rytla jako część rozprawy doktorskiej w formie zbioru opublikowanych i powiązanych tematycznie artykułów naukowych.



(podpis współautora)

Poznań, dnia 02.06.2022

dr inż. Małgorzata Widelicka

Oświadczenie

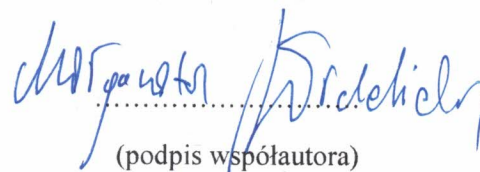
Oświadczam, że w niniejszych publikacjach:

*K. Rytel, K. Kędzierski, B. Barszcz, M. Widelicka, A. Stachowiak, A. Biadasz, Ł. Majchrzycki, E. Coy, D. Wróbel, The influence of diameter of multiwalled carbon nanotubes on mechanical, optical and electrical properties of Langmuir-Schaefer films, **Physical Chemistry Chemical Physics**, 39 (2020) 22380–2238,*

*K. Rytel, M. Widelicka, D. Łukawski, F. Lisiecki, K. Kędzierski, D. Wróbel, Ultrasonication-induced sp^3 hybridization defects in Langmuir-Schaefer layers of turbostratic graphene, **Physical Chemistry Chemical Physics**, 20 (2018) 12777–12784*

mój udział polegał na rejestracji i analizie widm ramanowskich oraz opisie otrzymanych wyników spektroskopii Ramana.

Wyrażam zgodę na przedłożenie ww. pracy przez mgr. inż. Karol Rytla jako część rozprawy doktorskiej w formie zbioru opublikowanych i powiązanych tematycznie artykułów naukowych.



(podpis współautora)

Warszawa, dnia 04.04.2022

dr Daniel Waszak

Oświadczenie

Oświadczam, że w niniejszej publikacji

*K. Rytel, D. Waszak, K. Kędziński, D. Wróbel**, Novel method of current collector coating by multiwalled carbon nanotube Langmuir layer for enhanced power performance of LiMn_2O_4 electrode of Li-ion batteries, *Electrochimica Acta* 222 (2016) 921–925

mój udział polegał na nadzorowaniu prac związanych z przygotowaniem i badaniem ogniw litowo-jonowych oraz pomocy w przygotowaniu manuskryptu.

Wyrażam zgodę na przedłożenie ww. pracy przez mgr. inż. Karol Rytla jako część rozprawy doktorskiej w formie zbioru opublikowanych i powiązanych tematycznie artykułów naukowych.



(podpis współautora)

Poznań, dnia 04.04.2022

mgr inż. Alicja Stachowiak

Oświadczenie

Oświadczam, że w niniejszej publikacji:

K. Rytel, K. Kędzierski, B. Barszcz, M. Widelicka, A. Stachowiak, A. Biadasz, Ł. Majchrzycki, E. Coy, D. Wróbel, The influence of diameter of multiwalled carbon nanotubes on mechanical, optical and electrical properties of Langmuir-Schaefer films, Phys. Chem. Chem. Phys. 22 (2020) 22380–22389. doi:10.1039/d0cp03687k. (MEiN 100, IF 3.802)

mój udział polegał na wykonaniu pomiarów transmitancji warstw Langmuira-Schafera wielościennych nanorurek węglowych o różnych średnicach.

Wyrażam zgodę na przedłożenie ww. pracy przez mgr. inż. Karol Rytla jako część rozprawy doktorskiej w formie zbioru opublikowanych i powiązanych tematycznie artykułów naukowych.



(podpis współautora)

Przedruk publikacji [Rytel, PCCP 2018]

K. Rytel, M. Widelicka, D. Łukawski, F. Lisiecki, K. Kędzierski, D. Wróbel,
Ultrasonication-induced sp^3 hybridization defects in Langmuir-Schaefer layers of turbostratic graphene, *Phys. Chem. Chem. Phys.* **20** (2018) 12777–12784.

doi:10.1039/c8cp01363b.

(MEiN 40, IF 3.567)



Cite this: *Phys. Chem. Chem. Phys.*,
2018, 20, 12777

Ultrasonication-induced sp^3 hybridization defects in Langmuir–Schaefer layers of turbostratic graphene†

K. Rytel,^a M. Widelicka,^b D. Łukawski,^a F. Lisiecki,^b K. Kędzierski^a and D. Wróbel^a

Ultrasonic homogenization is the method of choice for producing and dispersing graphene. In this paper, we show that sp^3 hybridization defects introduced by long high-power sonication cause a significant decrease in electrical conductivity. In order to show this, two turbostratic graphene (TG) dispersions were sonicated at two power settings of the tip sonifier at 20 W and 60 W, and for different periods varying from 1 min to 180 min. Afterwards, TG thin films were prepared by the Langmuir technique and transferred onto a quartz substrate by the Langmuir–Schaefer method. The thin films were investigated by electrical conductivity measurement, UV-VIS, Raman spectroscopy and scanning electron microscopy. We found that the relative performance of the TG thin films in terms of transparency and sheet resistance was higher than that for similarly prepared pristine graphene flakes, reported in our previous work. Moreover, despite the increase in transmittance, the electrical conductance significantly decreases with the time of sonication, especially for the 60 W sonication power. The results of Raman spectroscopy indicate that this particular behavior can be explained by the introduction of sp^3 hybridization defects into the TG flakes during high power sonication.

Received 1st March 2018,
Accepted 13th April 2018

DOI: 10.1039/c8cp01363b

rsc.li/pccp

Introduction

Graphene has attracted wide interest owing to its remarkable mechanical, electrical and thermal properties, which make it promising for low cost transparent electrodes and electrical devices, or as an efficient reinforcement in composite materials.^{1–3} Defect-free monolayer graphene flakes are characterized by ballistic electrical conductivity. However, the production and application of monolayer graphene is complex and very expensive.⁴ On the other hand, making few-layer graphene flakes is cheaper and simpler. Unfortunately, an increase in the number of graphene layers modifies the dispersion of electronic states, which leads to opening of the band gap. Therefore, the electrical transport is disturbed causing deterioration in the parameters of electrical devices made from few-layer graphene.⁵ However, if the subsequent layers are twisted relative to each other, so-called turbostratic graphene (TG) is formed, which is characterized by an electronic structure similar to that of a single layer of graphene, leading to restoration of the ballistic transport.^{6,7}

Several methods have been proposed for the production of graphene layers. The best quality layers are obtained by sophisticated methods, such as mechanical exfoliation, epitaxial growth or molecular beam assembly, but high production costs still restrict their use to specialized applications.^{8–10} On the other hand, many authors have focused on cheaper and potentially scalable methods, such as spin-coating, spray-coating, transfer printing, and the Langmuir–Schaefer and Langmuir–Blodgett methods.^{11–15} The advantage of using Langmuir deposition techniques is the ability to precisely control the film density and structure.^{14–17} However, Langmuir deposition techniques are highly dependent on the quality of the used suspension. Thus, we have decided to use the Langmuir–Schaefer deposition technique to study the influence of the graphene sonication process on the TG film properties.

While most applications do not employ graphene dispersions directly, many of them require graphene to be dispersed at some stage of the process (*e.g.* the deposition of thin films or composite materials)^{18,19} and this may lead to material damage, causing deterioration of the electrical properties.²⁰ Three types of defects can be distinguished: boundary-like defects, vacancy-like defects, and defects associated with the change in carbon hybridization from sp^2 to sp^3 .^{3,21} The sonication process should be sufficient to properly disperse graphene, while at the same time being minimally invasive, so that the structure of the graphene flakes is not damaged.

^a Faculty of Technical Physics, Institute of Physics, Poznan University of Technology, Piotrowo 3, 60-965 Poznań, Poland. E-mail: karol.t.rytel@doctorate.put.poznan.pl

^b Institute of Molecular Physics, Polish Academy of Sciences, Smoluchowskiego 17, 60-179 Poznań, Poland

† Electronic supplementary information (ESI) available. See DOI: 10.1039/c8cp01363b

Moreover, the most common parameter used for the evaluation of the quality of graphene flakes is the D to G peak intensity ratio in Raman spectroscopy, which can be misinterpreted. Usually, a lower D to G ratio corresponds to a greater distance between defects, but when the mean distance between defects reaches about 3 nm, the ratio begins to decrease.^{22,23} Thus, a low value of the D to G peak intensity ratio is insufficient to estimate the quality of graphene flakes. Therefore, the graphene samples prepared using high-power ultrasonic homogenization can be incorrectly interpreted as low defect flakes. The aim of this research is to investigate the influence of the power and time of sonication on the electrical and morphological properties of TG thin films. Moreover, we would like to draw attention to the impact of ultrasonic homogenization on the graphene flake quality, which cannot be neglected.

TG thin films were prepared by the Langmuir technique and transferred onto a quartz substrate by the Langmuir–Schaefer method. We found that the optoelectronic quality of the transparent electrode obtained for the TG thin films decreases significantly with the time of sonication, due to a significant drop in electrical conductance, especially for the sample sonicated at 60 W power. In this paper we have used the D and D' peak integral intensity ratio to explain the optoelectronic quality changes. The results of the Raman spectroscopy studies indicate that this particular behavior can be explained by the introduction of sp^3 hybridization defects into the TG flakes during high power sonication.

Materials and methods

Materials

In this work thin films of turbostratic graphene of flake size 150–500 nm (G1B, Cambridge Nanosystems Ltd) were investigated. A suspension was prepared by adding 13.33 mg of graphene powder to 200 ml of spectrally pure dichloromethane (DCM). Then, the sample was sonicated. Ultrasonication was carried out by a probe sonicator (Hielscher 400St, 24 kHz) in an ice bath to minimize solvent evaporation. Two suspensions were prepared with the use of different sonication powers. The first suspension was sonicated by a 3 mm diameter sonotrode at 20 W power and the second suspension was sonicated by a 14 mm diameter sonotrode at 60 W power. The suspension was sonicated for a preset period of time (Fig. 1) and then 10 ml of suspension was collected for thin film preparation. Afterwards, the sonication process was repeated for the remaining suspension, for the next preset time period, as presented in Fig. 1. Finally, the total sonication time, after a few repetitions, reached 120 min and 180 min, for the sonication powers of 20 W and 60 W, respectively. The suspension volume changed during each sonication step. The power densities and the corresponding time intervals are given in Fig. 1 illustrating the sample preparation procedure. Furthermore, in order to prevent misunderstanding, we decided to label the samples according to the power and total time of sonication. The labels are also given in Fig. 1. It should be mentioned that the sample labels refer to the

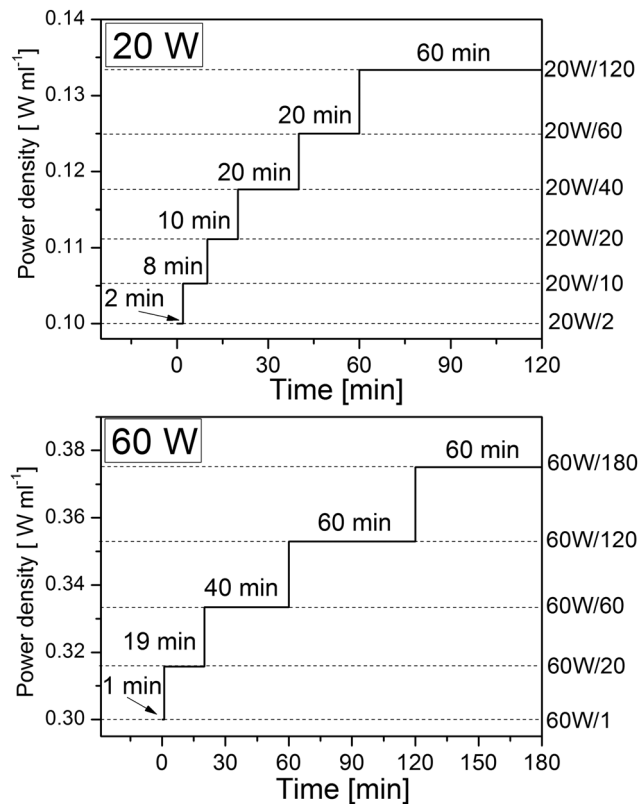


Fig. 1 Sonication history of the samples; in the sample labels the sonication power is followed after the slash by a number that stands for the total time of sonication.

prepared TG suspensions and also to the films obtained using these suspensions.

Film preparation

The TG thin films were obtained on a KSV instruments Ltd 2000 Langmuir–Blodgett System with a Teflon trough of 750 cm² area (15 cm × 50 cm), under laminar flow at a stabilized temperature of 20 ± 0.5 °C. In our experiments the subphase was deionized water (electrical resistivity 18.2 MΩ cm) obtained with an ultrapure water purification system (Millipore Corp.). To obtain a floating film, 10 ml of the TG suspension was carefully spread onto the subphase and DCM was allowed to evaporate. The floating film was compressed symmetrically from both sides at a rate of 150 mm² min⁻¹ of surface compression change. The layers were transferred onto a quartz substrate (76 mm × 26 mm) by horizontal transfer, carried out by removal of the substrate from the subphase, in a similar way as in previous studies.^{24–26} The substrate was removed at a constant speed of 1 mm min⁻¹. Before transfer, the floating films were relaxed at a specified surface pressure for 30 min to obtain a uniform layer.

Experimental methods

The electrical resistance measurements (Keithley 2400-LV) were performed using a standard two-probe method. The contacts were made of silver wire (diameter 250 μm) and they were

attached to the sample using silver paint. Measurements for each film were made at 12 different locations and the measurement uncertainty was calculated as the standard deviation. A Cary 4000 spectrophotometer (Varian) was applied for the recording of transmission spectra in the range of 220–900 nm. Transmission measurements were repeated several times at different sites of the samples and no difference was observed, which proves the uniform coverage of the substrates. The SEM images were recorded by means of an FEI Nova NanoSEM 650 scanning electron microscope operating at 5 kV in immersion mode. The Raman spectra were collected with a Jobin Horiba LabRAM HR 800 spectrometer connected with a CCD detector, in the 1200–1800 cm^{-1} and 2000–2800 cm^{-1} range. During the measurements, a 633 nm He–Ne laser excitation line was used. To avoid degradation of the samples, the laser power at the sample was below 1 mW.

Thermodynamics of Langmuir films

The surface pressure (π) vs. area (A) isotherms was recorded during the film compression (Fig. 2) to provide repeatability of the transferred layers. The compressibility modulus C_s^{-1} was calculated as:^{27,28}

$$C_s^{-1} = -A \left(\frac{d\pi}{dA} \right),$$

where π is the pressure and A is the trough area. The surface compressibility modulus of an insoluble layer is a measure of the film stiffness. The compressibility modulus vs. surface pressure is shown in the inset of Fig. 2. The increase in the compressibility modulus corresponds to stronger interaction between the graphene flakes. It reached a maximum value at about 40 mN m^{-1} of surface pressure. At higher surface pressure, the film started to crack and overlap, causing the surface compressibility module to decrease. A similar effect was observed and explained for graphene oxide layers.^{29,30} The dependence of the surface compressibility module on the surface pressure did not change in the range of surface pressure from 0 mN m^{-1} to 40 mN m^{-1} either with the time of sonication or its power. The surface pressure of 40 mN m^{-1} for transferring the layers was

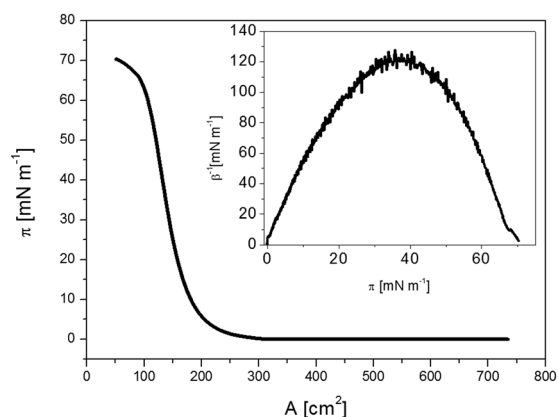


Fig. 2 The π – A isotherm of the TG film and compressibility vs. surface pressure (inset).

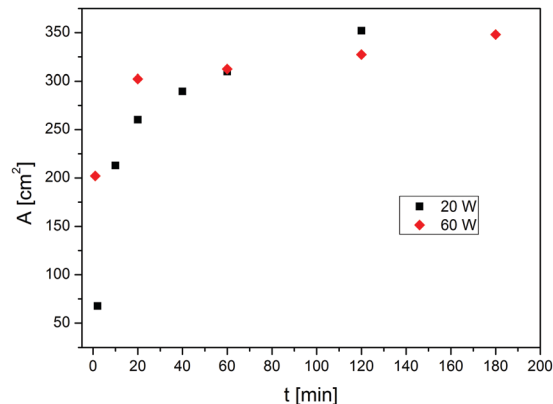


Fig. 3 Area occupied by the graphene film at a surface pressure of 40 mN m^{-1} at various sonication times.

chosen because it ensures the best homogeneity with the lowest surface resistance.

The area occupied by the TG films at the surface pressure of 40 mN m^{-1} for all tested samples is shown in Fig. 3. The area occupied by the TG film increased with increasing sonication time for both sonication powers. At the sonication power of 20 W, nonlinear changes in the area occupied by the TG films can be observed. The character of these changes implies that the material becomes better dispersed with increasing sonication time. The evaporation process was reduced by decreasing the solvent temperature in the ice bath. The suspensions obtained at 20 W sonication power and a time longer than 120 min occupied too large an area of the Langmuir trough to obtain repetitive results.

TG film morphology

The graphene layers prepared from suspensions made at different sonication powers (20 W and 60 W) for various sonication times, were transferred onto quartz substrates. Then, they were studied by SEM (Fig. 4). Sample 60 W/1 showed a small amount of agglomerated TG on the substrate, as well as some uncovered spots of the substrate. After 20 min of sonication (sample 60 W/20), the amount of agglomerates dropped significantly, but a longer sonication time only slightly improved the TG dispersion. Samples 60 W/60, 60 W/120 and 60 W/180 were more uniformly dispersed, without any large graphene agglomerates, but some uncovered areas were also found. A more significant difference in layer uniformity in the samples obtained for different sonication times was observed for layers prepared with the sonication power of 20 W. After 2 minutes of sonication (sample 20 W/2), large agglomerates and many uncovered areas were visible and distinctly broader than those for sample 60 W/1. The layer uniformity was improved after 20 minutes of sonication (sample 20 W/20), although some smaller agglomerates were still visible. For samples 20 W/60 and 20 W/120, no further changes were observed. The longest sonication time resulted in a similar morphology to the layers obtained at 20 W and 60 W sonication power. Because most of the TG flakes can overlap, it was impossible to determine

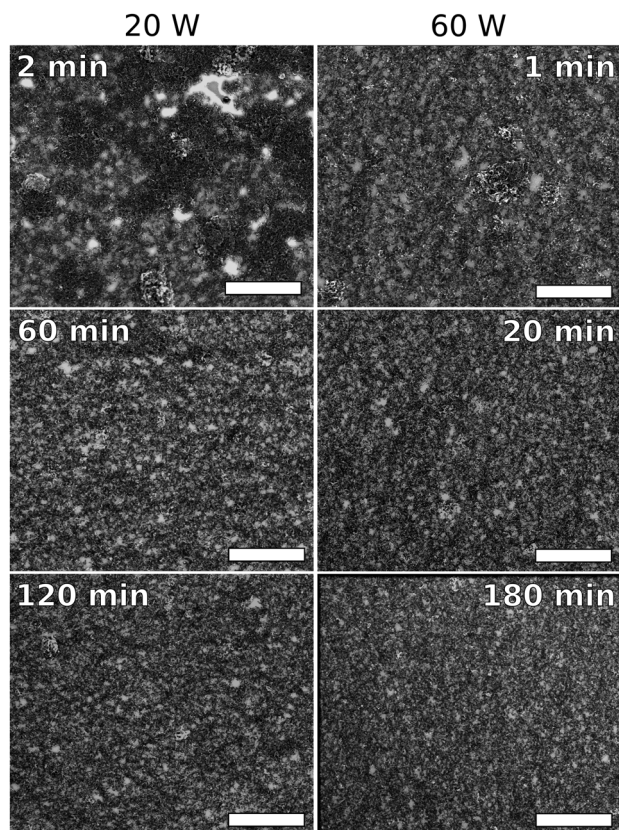


Fig. 4 SEM images of the TG layers transferred onto quartz substrates; the scale bars represent 5 μm.

accurately their size, but the visible flake sizes in all samples were within the size range given by the manufacturer. All SEM images of the TG layers at three different magnifications are shown in the ESI† (Fig. S1 and S2).

Optoelectrical properties

In order to determine the optical properties of the TG layers, the transmittance at 550 nm was recorded (Fig. 5A). The transmittance spectra in the range of 220–900 nm for the longest and the shortest sonication times are shown in the ESI† (Fig. S3, ESI†). At a sonication power of 60 W and at a sonication time above 20 min, some minor changes in transmittance (from 80.4 to 82.6) were observed. The reason was that the TG in the suspension was almost fully dispersed. A similar value of transmittance has been observed by other researchers in the Langmuir–Schaefer graphene layers.¹⁵ A significant change with time was observed in the transmittance (from 58.2% to 77.7%) of the samples sonicated at 20 W power. The changes tend to saturation and the layer transmittance after a sufficiently long time should be close to that of the samples obtained at 60 W of sonication power. To more accurately analyze the above data, the equivalent average number of graphene layers, N , per unit area was calculated as:

$$N = \log_{T_s} T,$$

where T_s is the transmittance of a single graphene layer and T is the measured transmittance of the TG film. Taking into

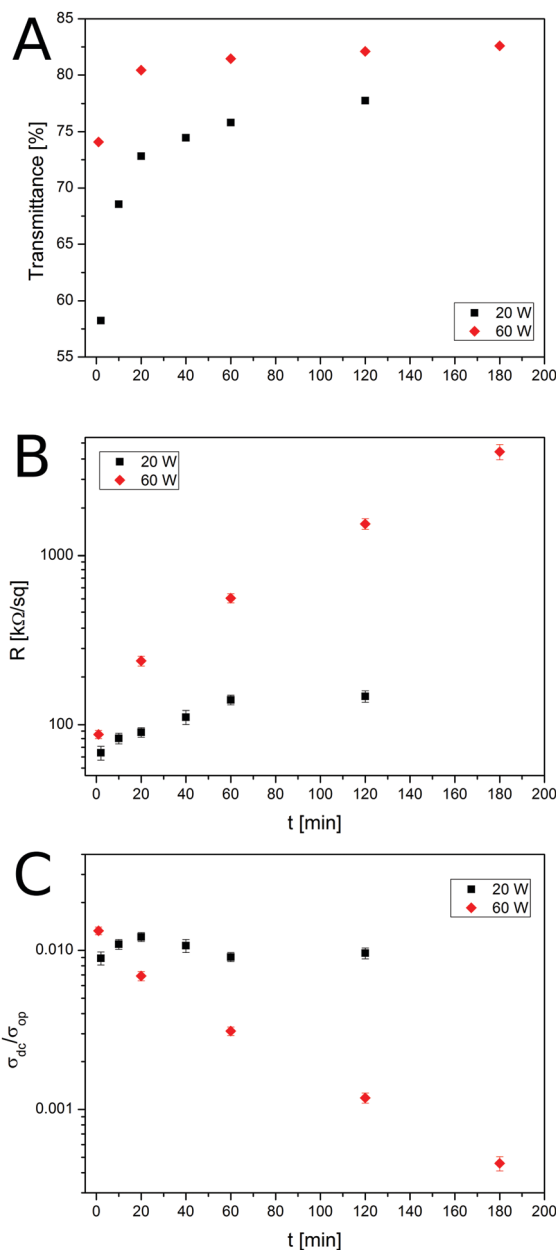


Fig. 5 Comparison of the optoelectrical properties of the TG films obtained at various sonication powers and times: transmittance (A), surface resistance (B) and direct current conductivity to optical conductivity ratio (C) vs. time.

account the T_s of 0.977³¹ and the measured transmittance of the deposited films, the equivalent average number of graphene layers decreased with sonication time from 23.2–10.8 and 12.8–8.2 for the samples sonicated at 20 W and 60 W, respectively. However, the equivalent average number of graphene layers does not reflect the number of layers in one graphene flake (according to the manufacturer, in one flake 3 ± 2 graphene layers were measured *via* TEM and AFM). This is due to the fact that some of the flakes may be bent or stack on each other causing overestimation of the calculated equivalent average number of layers. On the other hand, SEM images

reveal some uncovered areas which contributed to a reduction in this number. Despite these problems, changes in the equivalent average number of graphene layers are a decent approximation of the packing density.

The conclusion that arises from the presented data is that for samples 60 W/1 and 20 W/40, a similar optoelectrical quality can be expected. Moreover, minor changes in the number of equivalent graphene layers were observed after the first two sonication steps (~ 1 and ~ 2 for samples sonicated at 60 W and 20 W power, respectively).

Fig. 5B presents the surface resistivity of the transferred TG films. For all samples, linear current–voltage characteristics were observed in the measured current range (from $-1 \mu\text{A}$ to $1 \mu\text{A}$). As expected, the lowest surface resistance of $68 \text{ k}\Omega \text{ sq}^{-1}$ and $87 \text{ k}\Omega \text{ sq}^{-1}$ was noted for the 20 W/2 and 60 W/1 samples, respectively. The surface resistivity of sample 20 W/2 almost doubled when compared with that of sample 20 W/60, while the difference in the surface resistivity of samples 20 W/60 and 20 W/120 was within the measurement uncertainty ($140 \pm 10 \text{ k}\Omega \text{ sq}^{-1}$ vs. $147 \pm 11 \text{ k}\Omega \text{ sq}^{-1}$, respectively). This observation may be explained by the fact that better electrical conduction channels were provided by the graphene agglomerates and together with the better dispersion of TG they were responsible for the surface resistance increase. A completely different nature of surface resistivity changes was observed for the samples sonicated at the power of 60 W. When the sonication time increased, the surface resistance increased exponentially throughout the examined time range, reaching the maximum value of $4100 \pm 400 \text{ k}\Omega \text{ sq}^{-1}$. Taking into account the SEM images, such a significant change in surface resistivity for the samples sonicated at 60 W power cannot be explained by the removed graphene agglomerates.

In order to characterize the relative performance of the TG films in terms of transparency and sheet resistance, the ratio of direct current conductivity to optical conductivity was calculated as:

$$\frac{\sigma_{\text{DC}}}{\sigma_{\text{OP}}} = \frac{Z_0}{2R_s(T^{-0.5} - 1)}$$

where $Z_0 = 377 \Omega$ is the impedance of free space, T is the transmittance at 550 nm and R_s is the surface resistance. The value of the $\sigma_{\text{DC}}/\sigma_{\text{OP}}$ ratio can be used as a parameter to compare transparent electrodes of different thicknesses and prepared using different synthesis routes or materials.²⁹ The higher the $\sigma_{\text{DC}}/\sigma_{\text{OP}}$ ratio, the better the quality of the materials as transparent electrodes. The highest $\sigma_{\text{DC}}/\sigma_{\text{OP}}$ ratios of 0.0132 ± 0.0007 and 0.0122 ± 0.0008 were obtained for samples 60 W/1 and 20 W/20, respectively. According to other studies, for pristine graphene transferred *via* Langmuir techniques, the $\sigma_{\text{DC}}/\sigma_{\text{OP}}$ ratios were 0.011 and 0.0004.^{15,32} However, the highest $\sigma_{\text{DC}}/\sigma_{\text{OP}}$ ratio of 7.29 was reported for ultra-large graphene oxide layers after oxide reduction.²⁹ Increasing the sonication time (sonication power of 20 W) causes some minor changes in the $\sigma_{\text{DC}}/\sigma_{\text{OP}}$ ratio. On the other hand, for the sonication power of 60 W, the $\sigma_{\text{DC}}/\sigma_{\text{OP}}$ ratio was decreased by two orders of magnitude within the studied sonication time range (Fig. 5C).

This implies that the changes in surface resistivity cannot be explained by the reduction of graphene agglomerates or by the equivalent average number of graphene layers.

Raman spectra

To explain the reason for the surface resistance drop at the sonication power of 60 W, Raman spectroscopy was performed. The exemplary Raman spectrum of the TG layer with the highest $\sigma_{\text{DC}}/\sigma_{\text{OP}}$ ratio (60 W/1) is presented in Fig. 6. The four basic graphene peaks, D ($\sim 1333 \text{ cm}^{-1}$), G ($\sim 1585 \text{ cm}^{-1}$), D' ($\sim 1618 \text{ cm}^{-1}$) and 2D ($\sim 2657 \text{ cm}^{-1}$), are observed. The D peak corresponds to the breathing modes of carbon hexagons and requires a defect for its activation. The G peak can be assigned to the E_{2g} phonon at the Brillouin-zone center. The D' peak is an overtone of the D peak. The 2D peak is the second order of the D peak and originates from the process in which momentum conservation is satisfied by two phonons with opposite wave vectors and no defects are required for their activation. Thus the 2D peak is always present.^{5,22}

The shape of the 2D peak is symmetrical and it occurs in the spectra of either the single layer graphene or TG irrespective of the number of graphene flakes.^{21,23} Its position is $\sim 2670 \text{ cm}^{-1}$ for a single layer of graphene and $\sim 2670 \text{ cm}^{-1}$ for a TG layer.²³ The full width at half maximum (FWHM) of the 2D peak for a single layer was reported as $\sim 30 \text{ cm}^{-1}$ and this value increased with an increasing number of graphene layers reaching $50\text{--}55 \text{ cm}^{-1}$ and $55\text{--}58 \text{ cm}^{-1}$ for bi- and tri-layered graphene, respectively.³³ In the spectrum of the TG layer, its FWHM is almost doubled in comparison to that of the peak for a single layer of graphene. Moreover, Kim *et al.* have reported that the 2D position and FWHM vary with rotational angle in bilayer TG.³⁴ In our work, the 2D peak position of $\sim 2656 \text{ cm}^{-1}$ was observed for the films obtained at 20 W of sonication power (all peak parameters are shown in the ESI,† Table S1). From the comparison of our results with literature data, it can be concluded that the positions of the Raman peaks correspond to two TG layers.³⁵ For the films obtained at 60 W sonication power, the 2D peak position was upshifted to $\sim 2658 \text{ cm}^{-1}$, which suggests that the average number of graphene layers was slightly greater than

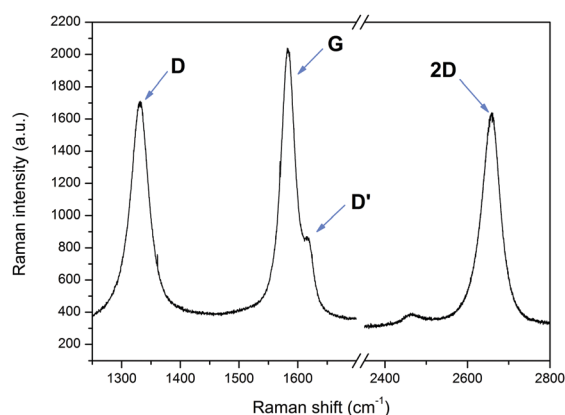


Fig. 6 Raman spectra of the TG layer characterized by the highest $\sigma_{\text{DC}}/\sigma_{\text{OP}}$ ratio value.

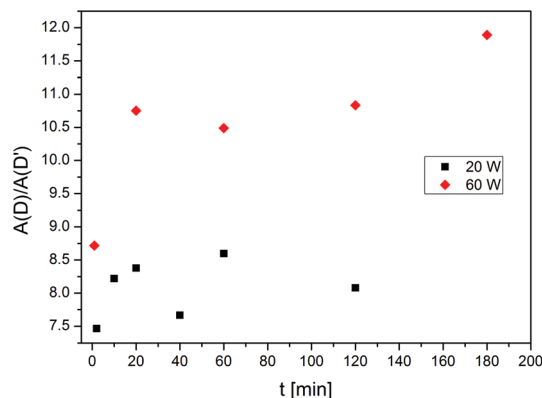


Fig. 7 The $A(D)/A(D')$ ratio vs. sonication time.

that for the sample obtained at 20 W, but did not exceed three.¹⁵ Moreover, the 2D peak position did not change with the time of sonication. For both sonication powers, the FWHM was in the range of 52–58 cm^{-1} (ESI,† Fig. S4). This parameter decreases with the time of sonication, which may be caused by the change in the number of TG layers or in rotational angle. Taking into account the fact that a slight difference between the data collected for the samples obtained at both sonication powers was observed and the sonication process may change the rotational angle and average number of graphene layer, we can conclude that the changes in the number of graphene layers were almost identical. In the next step, we analyzed the influence of defects on the conductivity properties.

The integral intensity ratios of the D and G peaks $A(D)/A(G)$ (ESI,† Fig. S5, ESI†) were used to quantify the defects in the graphene-related systems. In this work, the $A(D)/A(G)$ ratios were in the range of 0.8–1.1, irrespective of the sonication power or time. This implies that the average number of defects does not increase and changes in the $\sigma_{\text{DC}}/\sigma_{\text{OP}}$ ratio were caused by another effect. According to Eckmann *et al.*, the integral intensity ratio of the D and D' peaks $A(D)/A(D')$ can be used to probe the nature of the defects in graphene and it does not change with the number of defects. They found that an $A(D)/A(D')$ ratio of ~ 3.5 was associated with boundary-like defects. When the number of vacancy-like defects was dominant, this value increased to ~ 7 , reaching a maximum value of ~ 13 for dominant defects with sp^3 hybridization. The $A(D)/A(D')$ ratio vs. sonication time is presented in Fig. 7. As it can be seen, for all samples prepared at 20 W sonication power, an $A(D)/A(D')$ ratio of ~ 8 was observed. Irrespective of the sonication time, in these samples, the vacancy defects were dominant, which explains the minor $\sigma_{\text{DC}}/\sigma_{\text{OP}}$ ratio changes. On the other hand, for the sonication power of 60 W, this ratio increased from 8.7 to 11.8, resulting in the lowering of the $\sigma_{\text{DC}}/\sigma_{\text{OP}}$ value. These changes were caused by the increasing contribution of sp^3 hybridization defects in the examined films. The value of the $\sigma_{\text{DC}}/\sigma_{\text{OP}}$ ratio depends on the type of defects and not their quantity. Increasing the contribution of sp^3 hybridization defects leads to a decrease in the value of the $\sigma_{\text{DC}}/\sigma_{\text{OP}}$ ratio and an increase in the film's resistance.

Conclusions

Two TG dispersions were prepared using two power settings of 20 W and 60 W. Despite the small flake size (150–500 nm), the TG thin films obtained by the Langmuir method showed relatively high $\sigma_{\text{DC}}/\sigma_{\text{OP}}$ ratios, in comparison to those described in earlier reports.^{15,32} With an increase in sonication time, the transmittance at 550 nm increased and the electrical conductance decreased. Thus, the $\sigma_{\text{DC}}/\sigma_{\text{OP}}$ ratio was nearly constant, despite the increasing sonication time. This effect is easily explained by the SEM images, showing the existence of TG agglomerates in the samples sonicated for shorter than 60 min. In contrast, for the samples obtained at 60 W, a longer sonication time induced a slight rise in transmittance and a significant drop in electrical conductivity. The sheet resistance increased from $87 \pm 5 \text{ k}\Omega \text{ sq}^{-1}$ for 1 min sonication, to $4.1 \pm 4 \text{ M}\Omega \text{ sq}^{-1}$ for 120 min sonication. Therefore, the $\sigma_{\text{DC}}/\sigma_{\text{OP}}$ ratio after 120 min of sonication was equal to $(9.5 \pm 0.6) \times 10^{-3}$ and $(1.18 \pm 0.05) \times 10^{-3}$ for 20 W and 60 W power, respectively. This particular behavior of dispersion in the samples obtained at 60 W may not be described on the basis of the SEM images. However, the analysis of the $A(D)/A(D')$ ratio explains that high power sonication of TG flakes causes the appearance of sp^3 hybridization defects, which are responsible for lowering the electrical conductivity of the TG thin films.

Conflicts of interest

There are no conflicts to declare.

Acknowledgements

The authors would like to thank Dr Boleslaw Barszcz (Institute of Molecular Physics, Polish Academy of Sciences) and MSC Mikołaj Bilski (Faculty of Mechanical Engineering and Management, Poznan University of Technology) for useful discussion. This project was financially supported by The National Science Centre of Poland (grant no. 2016/21/N/ST8/03557, K. R.) and Poznan University of Technology (grant no. 06/62/DSPB/2181, D. W., K. K.).

References

- 1 K. S. Novoselov, V. I. Fal'ko, L. Colombo, P. R. Gellert, M. G. Schwab and K. Kim, A roadmap for graphene, *Nature*, 2012, **490**, 192–200.
- 2 K. Hu, D. D. Kulkarni, I. Choi and V. V. Tsukruk, Graphene-polymer nanocomposites for structural and functional applications, *Prog. Polym. Sci.*, 2014, **39**, 1934–1972.
- 3 O. M. Istrate, K. R. Paton, U. Khan, A. O'Neill, A. P. Bell and J. N. Coleman, Reinforcement in melt-processed polymer-graphene composites at extremely low graphene loading level, *Carbon*, 2014, **78**, 243–249.
- 4 X. Du, I. Skachko, A. Barker and E. Y. Andrei, Approaching ballistic transport in suspended graphene, *Nat. Nanotechnol.*, 2008, **3**, 491–495.

- 5 K. F. Mak, M. Y. Sfeir, J. A. Misewich and T. F. Heinz, The evolution of electronic structure in few-layer graphene revealed by optical spectroscopy, *Proc. Natl. Acad. Sci. U. S. A.*, 2010, **107**, 14999–15004.
- 6 J. M. B. Lopes Dos Santos, N. M. R. Peres and A. H. Castro Neto, Graphene bilayer with a twist: Electronic structure, *Phys. Rev. Lett.*, 2007, **99**, 0–3.
- 7 J. A. Garlow, L. K. Barrett, L. Wu, K. Kisslinger, Y. Zhu and J. F. Pulecio, Large-Area Growth of Turbostratic Graphene on Ni(111) via Physical Vapor Deposition, *Sci. Rep.*, 2016, **6**, 1–11.
- 8 K. S. Novoselov, A. K. Geim, S. V. Morozov, D. Jiang, Y. Zhang, S. V. Dubonos, I. V. Grigorieva, A. A. Firsov and K. S. Novoselov, Electric Field Effect in Atomically Thin Carbon Films, *Science*, 2007, **306**, 183–191.
- 9 K. V. Emtsev, A. Bostwick, K. Horn, J. Jobst, G. L. Kellogg, L. Ley, J. L. McChesney, T. Ohta, S. A. Reshanov, J. Röhrl, E. Rotenberg, A. K. Schmid, D. Waldmann, H. B. Weber and T. Seyller, Towards wafer-size graphene layers by atmospheric pressure graphitization of silicon carbide, *Nat. Mater.*, 2009, **8**, 203–207.
- 10 J. Park, W. C. Mitchel, L. Grazulis, H. E. Smith, K. G. Eyink, J. J. Boeckl, D. H. Tomich, S. D. Pacley and J. E. Hoelscher, Epitaxial graphene growth by Carbon Molecular Beam Epitaxy (CMBE), *Adv. Mater.*, 2010, **22**, 4140–4145.
- 11 E. Kymakis, E. Stratakis, M. M. Stylianakis, E. Koudoumas and C. Fotakis, Spin coated graphene films as the transparent electrode in organic photovoltaic devices, *Thin Solid Films*, 2011, **520**, 1238–1241.
- 12 S. Gilje, S. Han, M. Wang, K. L. Wang and R. B. Kaner, A chemical route to graphene for device applications, *Nano Lett.*, 2007, **7**, 3394–3398.
- 13 S. J. Wang, Y. Geng, Q. Zheng and J. K. Kim, Fabrication of highly conducting and transparent graphene films, *Carbon*, 2010, **48**, 1815–1823.
- 14 Q. Zheng, L. Shi, P.-C. Ma, Q. Xue, J. Li, Z. Tang and J. Yang, Structure control of ultra-large graphene oxide sheets by the Langmuir–Blodgett method, *RSC Adv.*, 2013, **3**, 4680.
- 15 A. Fahimi, I. Jurewicz, R. J. Smith, C. S. Sharrock, D. A. Bradley, S. J. Henley, J. N. Coleman and A. B. Dalton, Density controlled conductivity of pristine graphene films, *Carbon*, 2013, **64**, 435–443.
- 16 T. Da Ros, M. Prato, M. Carano, P. Ceroni, F. Paolucci, S. Roffia, L. Valli and D. Guldi, Synthesis, electrochemistry, Langmuir–Blodgett deposition and photophysics of metal-coordinated fullerene-porphyrin dyads, *J. Organomet. Chem.*, 2000, **599**, 62–68.
- 17 S. Conoci, D. M. Guldi, S. Nardis, R. Paolesse, K. Kordatos, M. Prato, G. Ricciardi, M. G. H. Vicente, I. Zilbermann and L. Valli, Langmuir–Schaefer transfer of fullerenes and porphyrins: formation, deposition, and application of versatile films, *Chem. – Eur. J.*, 2004, **10**, 6523–6530.
- 18 H. Becerril, J. Mao, Z. Liu and R. Stoltenberg, Evaluation of solution-processed reduced graphene oxide films as transparent conductors, *ACS Nano*, 2008, **2**, 463–470.
- 19 T. Kuilla, S. Bhadra, D. Yao, N. H. Kim, S. Bose and J. H. Lee, Recent advances in graphene based polymer composites, *Prog. Polym. Sci.*, 2010, **35**, 1350–1375.
- 20 D. W. Johnson, B. P. Dobson and K. S. Coleman, A manufacturing perspective on graphene dispersions, *Curr. Opin. Colloid Interface Sci.*, 2015, **20**, 367–382.
- 21 A. Eckmann, A. Felten, A. Mishchenko, L. Britnell, R. Krupke, K. S. Novoselov and C. Casiraghi, Probing the nature of defects in graphene by Raman spectroscopy, *Nano Lett.*, 2012, **12**, 3925–3930.
- 22 L. G. Cançado, A. Jorio, E. H. M. Ferreira, F. Stavale, C. A. Achete, R. B. Capaz, M. V. O. Moutinho, A. Lombardo, T. S. Kulmala and A. C. Ferrari, Quantifying defects in graphene via Raman spectroscopy at different excitation energies, *Nano Lett.*, 2011, **11**, 3190–3196.
- 23 A. C. Ferrari and D. M. Basko, Raman spectroscopy as a versatile tool for studying the properties of graphene, *Nat. Nanotechnol.*, 2013, **8**, 235–246.
- 24 K. Rytel, D. Waszak, K. Kędzierski and D. Wróbel, Novel method of current collector coating by multiwalled carbon nanotube Langmuir layer for enhanced power performance of LiMn₂O₄ electrode of Li-ion batteries, *Electrochim. Acta*, 2016, **222**, 921–925.
- 25 K. Kędzierski, K. Rytel, B. Barszcz, A. Gronostaj, Ł. Majchrzycki and D. Wróbel, On the temperature dependent electrical resistivity of CNT layers in view of Variable Range Hopping models, *Org. Electron.*, 2017, **43**, 253–261.
- 26 K. Kędzierski, K. Rytel, Ł. Majchrzycki and D. Wróbel, Conductive and transparent films of oriented multi-walled carbon nanotubes by Langmuir–Schaefer method, *Thin Solid Films*, 2015, **589**, 701–706.
- 27 E. Piosik, M. Kotkowiak, I. Korbecka, Z. Galewski and T. Martyński, Photo-switching of a non-ionic azobenzene amphiphile in Langmuir and Langmuir–Blodgett films, *Phys. Chem. Chem. Phys.*, 2017, **19**, 23386–23396.
- 28 A. Wamke, K. Dopierała, K. Prochaska, H. Maciejewski, A. Białasz and A. Dudkowiak, Characterization of Langmuir monolayer, Langmuir–Blodgett and Langmuir–Schaefer films formed by POSS compounds, *Colloids Surf., A*, 2015, **464**, 110–120.
- 29 Q. Zheng, W. H. Ip, X. Lin, N. Yousefi, K. K. Yeung, Z. Li and J. K. Kim, Transparent conductive films consisting of ultra-large graphene sheets produced by Langmuir–Blodgett assembly, *ACS Nano*, 2011, **5**, 6039–6051.
- 30 M. M. Jaafar, G. P. M. K. Ciniciato, S. A. Ibrahim, S. M. Phang, K. Yunus, A. C. Fisher, M. Iwamoto and P. Vengadesh, Preparation of a Three-Dimensional Reduced Graphene Oxide Film by Using the Langmuir–Blodgett Method, *Langmuir*, 2015, **31**, 10426–10434.
- 31 S. E. Zhu, S. Yuan and G. C. A. M. Janssen, Optical transmittance of multilayer graphene, *EPL*, 2014, **108**, 17007.
- 32 A. Matković, I. Milošević, M. Miličević, T. Tomašević-Ilić, J. Pešić, M. Musić, M. Spasenović, D. Jovanović, B. Vasić, C. Deeks, R. Panajotović, M. R. Belić and R. Gajić, Enhanced sheet conductivity of Langmuir–Blodgett assembled graphene thin films by chemical doping, *2D Mater.*, 2016, **3**, 15002.

- 33 Y. Hao, Y. Wang, L. Wang, Z. Ni, Z. Wang, R. Wang, C. K. Koo, Z. Shen and J. T. L. Thong, Probing layer number and stacking order of few-layer graphene by Raman Spectroscopy, *Small*, 2010, **6**, 195–200.
- 34 K. Kim, S. Coh, L. Z. Tan, W. Regan, J. M. Yuk, E. Chatterjee, M. F. Crommie, M. L. Cohen, S. G. Louie and A. Zettl, Raman spectroscopy study of rotated double-layer graphene: misorientation-angle dependence of electronic structure, *Phys. Rev. Lett.*, 2012, **108**, 1–6.
- 35 D. R. Lenski and M. S. Fuhrer, Raman and optical characterization of multilayer turbostratic graphene grown *via* chemical vapor deposition, *J. Appl. Phys.*, 2011, **110**, 013720.

Ultrasonication induced sp^3 hybridization defects in Langmuir-Schaefer layers of turbostratic graphene

*K. Rytel^a, M. Widelicka^b, D. Łukawski^a, F. Lisiecki^b, K. Kędzierski^a, D. Wróbel^a

^a Faculty of Technical Physics, Institute of Physics, Poznan University of Technology,
Piotrowo 3, 60-965 Poznań, Poland

^b Institute of Molecular Physics, Polish Academy of Sciences,
Smoluchowskiego 17, 60-179 Poznań, Poland

Corresponding authors

Karol Rytel e-mail:karol.t.rytel@doctorate.put.poznan.pl

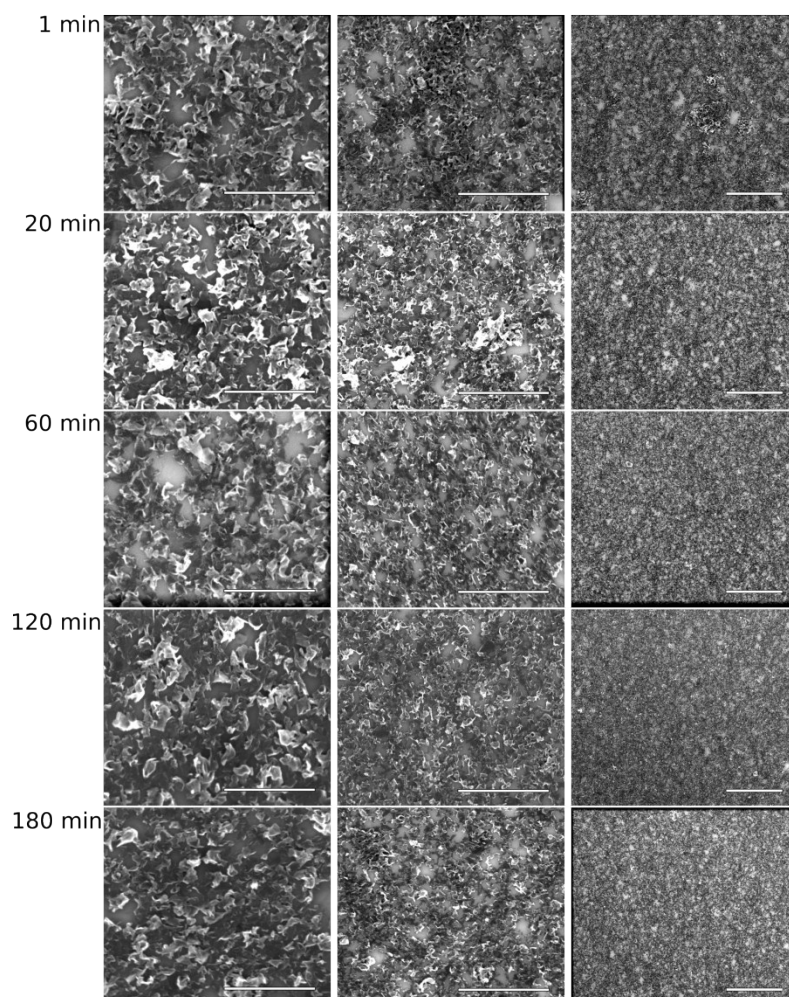


Fig. S1 SEM images of TG films transferred onto quartz substrate after 60 W sonication power and various sonication time; scale bar represents 1 μm, 2 μm and 5 μm left, middle and right column, respectively

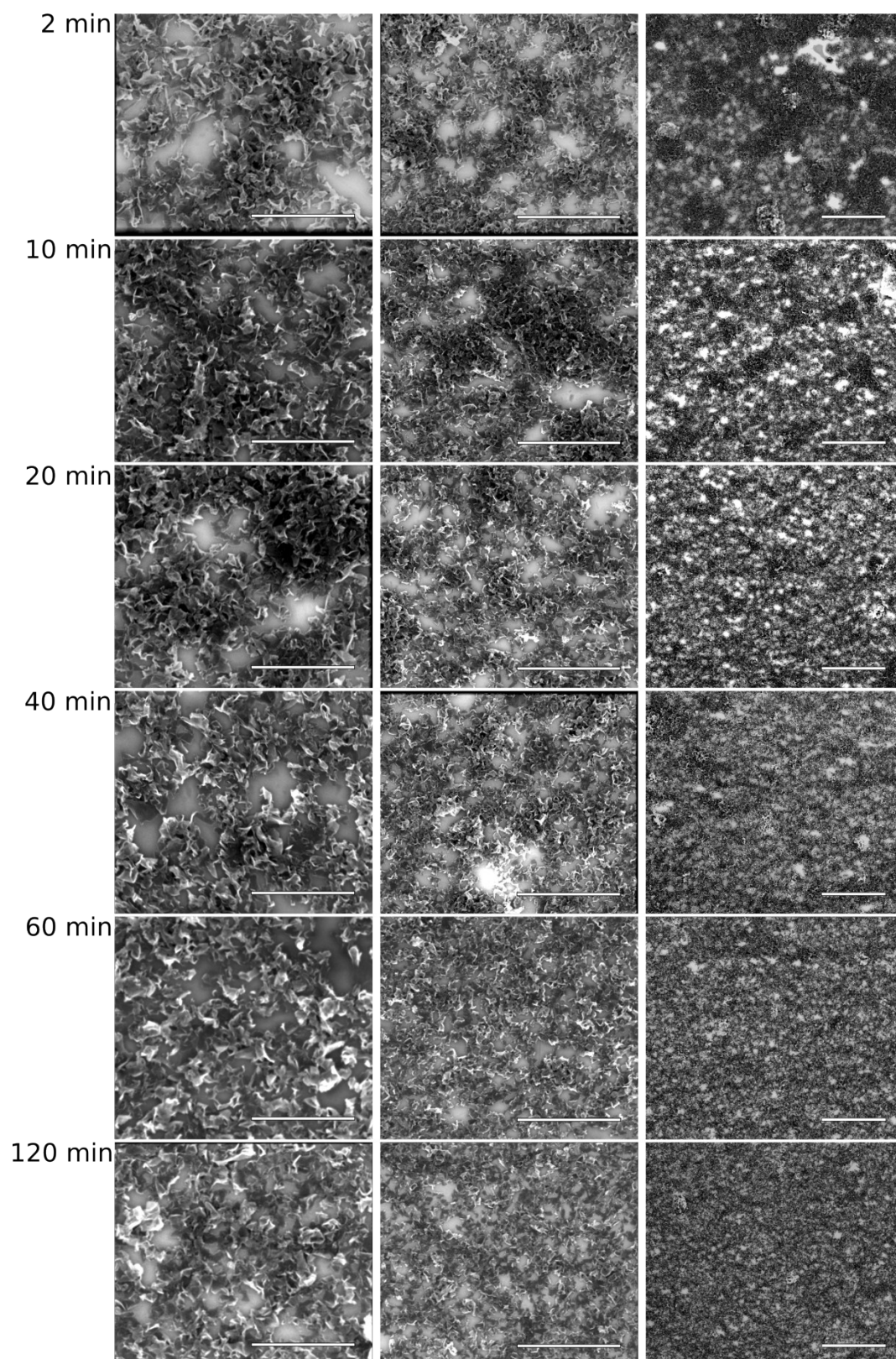


Fig. S2 SEM images of TG films transferred onto quartz substrate after 20 W sonication power and various sonication time; scale bar represents 1 μm , 2 μm and 5 μm left, middle and right column, respectively

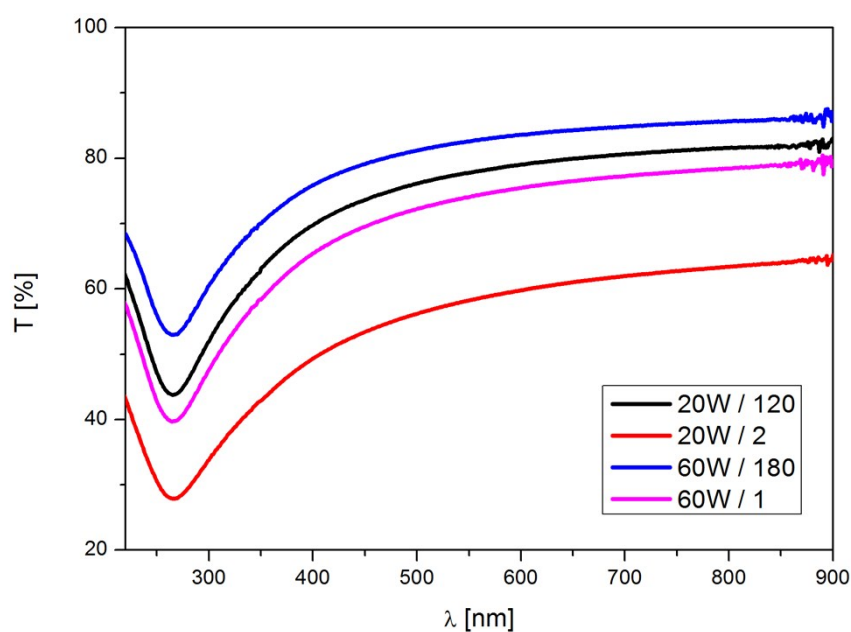


Fig. S3 Transmittance spectra of TG films; in sample labels the sonication power is followed after slash with the number that stands for the total time of sonication

Tab. S1 Raman peak parameters

Sample	D		G		D'		2D	
	C [cm ⁻¹]	A [a.u. cm ⁻¹]	C [cm ⁻¹]	A [a.u. cm ⁻¹]	C [cm ⁻¹]	A [a.u. cm ⁻¹]	C [cm ⁻¹]	A [a.u. cm ⁻¹]
20W/2	1331	49892	1584	59605	1619	6683	2656	94839
20W/10	1330	46669	1583	51889	1618	5677	2656	81779
20W/20	1331	49151	1584	47046	1618	5867	2656	72980
20W/40	1330	52157	1583	57296	1617	6804	2655	95387
20W/60	1330	45830	1582	51839	1617	5330	2656	82275
20W/120	1330	42146	1583	40422	1617	5216	2656	69400
60W/1	1331	36558	1584	39726	1618	4193	2657	63454
60W/20	1332	19964	1584	22221	1619	1856	2658	33496
60W/60	1332	21243	1584	22700	1619	2025	2658	31986
60W/120	1332	20773	1584	24771	1619	1917	2658	34658
60W/180	1332	24687	1584	31130	1618	2076	2658	40546

C – peak position, A – integral intensity

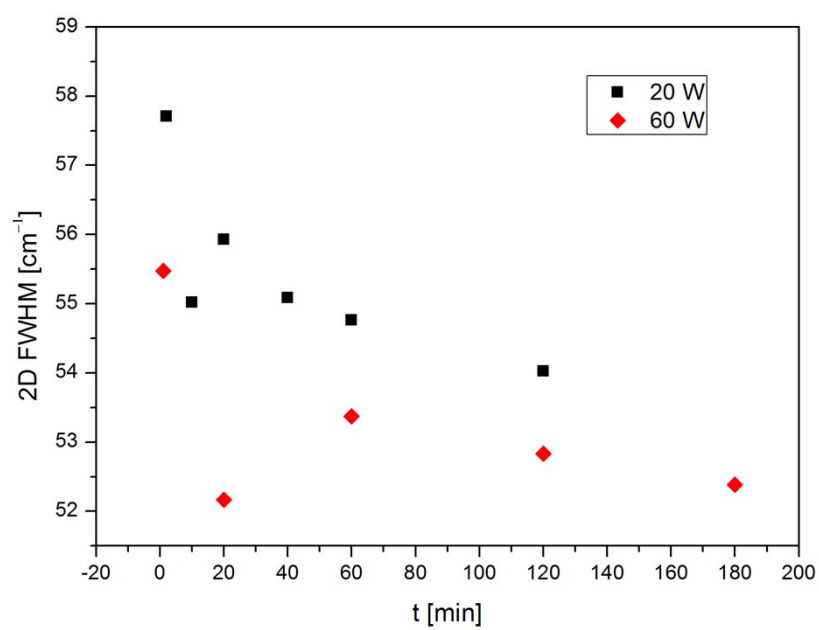


Fig. S4 Full width at half maximum of 2D peak vs. sonication time for 20 W and 60 W sonication power

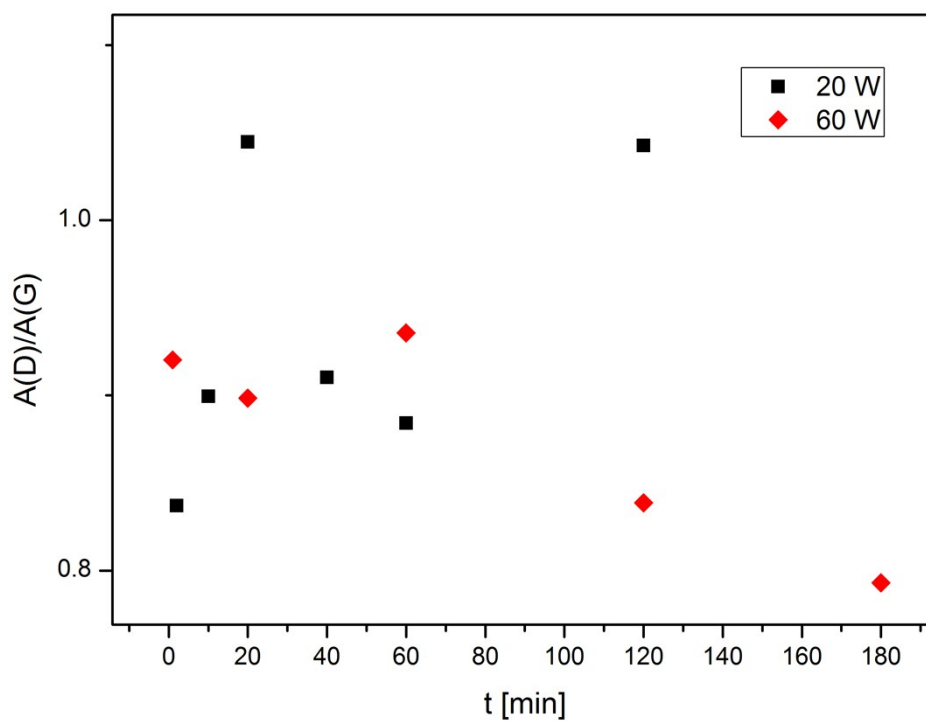


Fig. S5 Integral intensities ratio of D and G peak vs. sonication time for sample 20 W and 60 W

Przedruk publikacji [Rytel, PCCP 2020]

K. Rytel, K. Kędzierski, B. Barszcz, M. Widelicka, A. Stachowiak, A. Biadasz, Ł. Majchrzycki, E. Coy, D. Wróbel, *The influence of diameter of multiwalled carbon nanotubes on mechanical, optical and electrical properties of Langmuir-Schaefer films*, Phys. Chem. Chem. Phys. 22 (2020) 22380–22389.

doi:10.1039/d0cp03687k.

(MEiN 100, IF 3.676)



Cite this: *Phys. Chem. Chem. Phys.*,
2020, 22, 22380

The influence of diameter of multiwalled carbon nanotubes on mechanical, optical and electrical properties of Langmuir–Schaefer films†

Karol Rytel,^{a*} Kamil Kędzierski,^a Bolestaw Barszcz,^b Małgorzata Widelicka,^b Alicja Stachowiak,^a Andrzej Biadasz,^a Łukasz Majchrzycki,^c Emerson Coy^d and Danuta Wróbel^a

In this paper results of a study of mechanical, optical and electrical properties of thin films made of multiwall carbon nanotubes (MWCNT) of various types were reported. The MWCNT films were obtained on quartz substrates using the Langmuir–Schaefer (LS) method. A gradual increase in transmittance was recorded with decreasing diameters of MWCNT used. Moreover, a blue shift of the π -plasmon band position was observed with increasing MWCNT diameter. In all tested films, anisotropy of electrical surface resistivity was revealed, which was more pronounced for MWCNT of low diameters, except for the MWCNT sample of the smallest diameters. Results of oscillatory barrier measurements of various MWCNT films at the air water interface were used to calculate the complex compression and shear moduli. It is worth emphasizing that the values of these moduli were obtained for the first time for carbon nanotubes films. Moreover, the obtained results allowed identification of the main factor blocking the alignment process, which turned out to be the shear loss tangent.

Received 10th July 2020,
Accepted 20th September 2020

DOI: 10.1039/d0cp03687k

rsc.li/pccp

1. Introduction

The remarkable electrical, chemical and thermal properties of carbon nanotubes (CNT) have been well known for many years and allow their use in a wide range of applications, such as: lithium-ion batteries, supercapacitors, chemical sensors, electron field emitters, field effect transistors, transparent electrodes.^{1–7} Depending on the chirality of the single-walled carbon nanotubes (SWCNT), metallic and semiconducting SWCNT can be distinguished. Usually both semiconducting and metallic SWCNT are obtained simultaneously in the process of synthesis at the ratio of 1:2, respectively. Although the synthesis and purification methods currently used allow obtaining SWCNT with specific chirality, these methods are expensive and the material yield is low.^{8,9} While much research has been focused on application of

semiconducting SWCNT in the field effect transistors, the application of metallic SWCNT still remains insufficiently explored mainly due to their high production cost. Thus multi-walled carbon nanotubes (MWCNT) are often used as a cheaper alternative.

A precondition for the use of CNT in industrial applications is the possibility to obtain large scale and cheap homogeneous thin films, which is still problematic. Moreover, the one-dimensional character of CNT leads to extremely anisotropic mechanical, optical and electrical properties and most of their desired properties are better along the tube axis than in the direction perpendicular to the tube axis orientation.^{10–14} Two approaches can be applied in order to achieve horizontally aligned CNT films. The first is the *in situ* growth realized by direct growth of aligned CNT induced by arc discharge and chemical vapor deposition (CVD). The second approach is applied post synthesis to CNT suspensions in which the alignment process is realized in the most cases by the use of shear force, magnetic field, electric field or *via* barrier movement in Langmuir techniques.^{15,16} While the aligned films obtained using the direct approach are characterized by fewer defects in CNT and overall better quality, scaling up production and control of packing density still remains a problem. On the other hand, in the post synthesis approaches, external materials such as surfactants, polymers or functionalization of CNT are needed.^{17–19} However, this approach allows prior modification and/or purification of the used CNT.

^a Faculty of Materials Engineering and Technical Physics, Institute of Physics, Poznan University of Technology, Piotrowo 3, 60-965 Poznań, Poland.
E-mail: karol.rytel@put.poznan.pl

^b Institute of Molecular Physics, Polish Academy of Sciences, Smoluchowskiego 17, 60-179 Poznań, Poland

^c NanoBioMedical Centre, Adam Mickiewicz University, Wszechnicy Piastowskiej 3, 61-614 Poznań, Poland

^d NanoBioMedical Centre, Adam Mickiewicz University, Umultowska 85, 61-614 Poznań, Poland

† Electronic supplementary information (ESI) available. See DOI: 10.1039/d0cp03687k

One of the most interesting techniques of obtaining anisotropic CNT films in the post synthesis approach are the Langmuir–Blodgett (LB) and Langmuir–Schaefer (LS) ones. The advantage of using Langmuir deposition techniques is the ability to precisely control the film density, structure and production scalability. In this case, the alignment process can be carried out by multiple cycles of compressions and expansions of the film. During compression and expansion of the film, the drag torque induces the CNT to be aligned in parallel with respect to the barriers. Moreover, the CNT orientation can be enhanced by the LB transfer method in which the substrate is placed in the perpendicular orientation to the barriers.¹⁹ Unfortunately, the LB method is not suitable for the production of large surface films, especially without the use of surfactants, therefore the LS method in some cases can be a better alternative. Although almost perfectly aligned SWCNT were obtained using Langmuir techniques, MWCNT layers obtained by the same methods exhibit minor or even no anisotropy.^{11,12,20,21} Despite the barely visible alignment of individual MWCNT in the films, the films exhibit a strong anisotropy of their properties. Thus in this case it is better to evaluate the anisotropy by investigating the properties of the layers obtained.

In this study we wanted to find out why SWCNT are easier to align than MWCNT. To this end we examined mechanical, optical and electrical properties of thin MWCNT films prepared using the LS method. We found that electrical anisotropy increases as the diameter of the used MWCNT decreases. Interestingly, the electrical anisotropy for the smallest diameter MWCNT used deviates from the above dependence. In order to explain this anomaly, oscillatory barrier measurements were carried out. These measurements allowed the calculation of complex compression and shear moduli for the first time for CNT films. The obtained results permitted identification of the shear loss tangent as the main factor blocking the alignment process. In addition to these experiments we found the reverse π -plasmon band shift with changing diameter of the used MWCNT. The main factor causing the band shift was the wall thickness.

2. Experimental section

2.1. Materials

The MWCNT with various diameters were obtained from the Carbon Nanotubes Plus. The suspensions were prepared by adding MWCNT powder to 200 ml of spectrally pure dichloromethane (DCM). The obtained concentration of MWCNT powder varied from $23.5 \mu\text{g ml}^{-1}$ to $66.3 \mu\text{g ml}^{-1}$ (see Fig. 1). Then, the samples were sonicated. Ultrasonication was carried out by a probe sonicator (Hielscher 400St, 24 kHz) in an ice bath to minimize solvent evaporation. All suspensions were sonicated by a 14 mm diameter sonotrode at 60 W power for 20 min. Then a few drops of the suspensions were drop casted on commercially available CuTEM grids (TedPella). Transmission electron microscopy (TEM) images were obtained with a Jeol ARM 200F microscope operated at 200 kV. The number of nanotubes to determine the histogram was between 100 and 200 and histograms are shown in Fig. 1. The obtained results were fitted using the

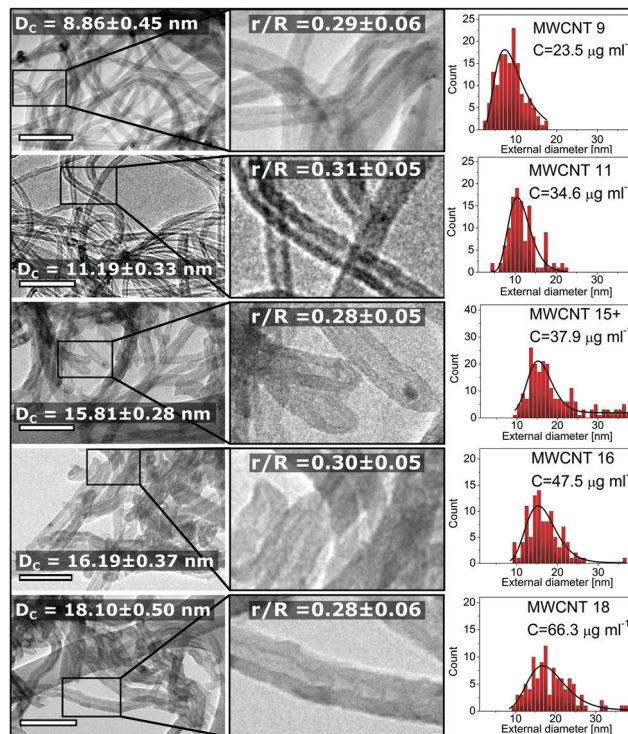


Fig. 1 TEM images of various diameters MWCNT with samples name (scale represents 100 nm distance), histograms of measured diameters, center of mass (D_c) fitted by lognormal function, ratio of internal to external diameter (r/R) and the concentration of MWCNT in DCM (C).

lognormal function implemented in Origin 8.1 and the final results are shown in Fig. 1. All samples were found to be relatively homogeneous in terms of diameter, except for the sample labelled as MWCNT 15+ in which a fraction of MWCNT of larger diameters in the range 25–50 nm was found. This sample was distinguished by addition of the ‘+’ symbol at the end of the sample name. The lengths of the all tested MWCNT were in accordance with the manufacturer’s data and for all samples were in the range of 0.2–2 μm .

2.2. Film preparation

The MWCNT thin films were obtained using a 2000 Langmuir–Blodgett System (KSV instruments Ltd) with a Teflon trough of 750 cm^2 area ($15 \text{ cm} \times 50 \text{ cm}$), under laminar flow at a stabilized temperature of $20 \pm 0.5 \text{ }^\circ\text{C}$. In our experiments the subphase was deionized water (electrical resistivity $18.2 \text{ M}\Omega \text{ cm}$) obtained with an ultrapure water purification system (Millipore Corp.). To obtain a floating film, 10 ml of the MWCNT suspension was carefully spread onto the subphase and left for 30 min to allow DCM to evaporate. The MWCNT concentration was selected in such a way that 10 ml of the suspension used would make a layer occupying the area as close as possible to 200 cm^2 at the surface pressure of 37.5 mN m^{-1} . This procedure was performed in order to obtain more repeatable results. The floating film was compressed symmetrically from both sides at a rate of $150 \text{ mm}^2 \text{ min}^{-1}$ of surface compression change. The layers were transferred simultaneously onto two quartz substrates ($7.6 \text{ cm} \times 2.6 \text{ cm}$)

and aluminum foil (2 cm × 2 cm) by horizontal transfer. One of the quartz substrates was placed in parallel and the other in perpendicular to the barrier. The transfer process was carried out by removal of the substrate from the subphase, in the same way as in our previous studies.^{20,22,23} The substrate was removed at a constant speed of 1 mm min⁻¹. Before the transfer, the floating films were relaxed at a specified surface pressure for 30 min to obtain a uniform layer.

2.3. Measurements

A Cary 4000 spectrophotometer (Varian) was used to record transmission spectra in the range of 190–900 nm. The transmission measurements were repeated several times at different sites of the films and no difference between them was observed, which confirmed the uniform coverage of all substrates. The electrical resistance measurements were performed using a standard two-probe method via 2400-LV source meter (Keithley). The contacts were made of silver wire (diameter 0.25 mm) and were attached to the film using a silver paint. The electrodes were placed in such a way to ensure the perpendicular or parallel current flow, with respect to the position of the barrier at the Langmuir trough (see Fig. 2). Measurements for each film were made at 12 different locations for each current flow direction and the measurement uncertainty was calculated as the standard deviation. After all measurements for as deposited samples were made, films with electrodes were annealed. Annealing process was performed for 5 hours in argon atmosphere under pressure of 1 mbar and at 250 °C and all electrical and optical measurements were repeated. The film areas were measured using a laser scanning microscopy LSM 710 (Zeiss) working in the material mode. The SEM images were recorded by means of the HeliosNanoLab 660 (FEI) scanning electron microscope operating at 1 kV.

The Raman spectra were collected with a Horiba Jobin Yvon-LabRAM HR 800 spectrometer connected to a liquid nitrogen-cooled CCD detector, in the 1200–1800 cm⁻¹ and 2000–2800 cm⁻¹ ranges. During the measurements, a 633 nm He–Ne laser excitation line was used. To avoid degradation of the films, the laser power at the film was kept below 1.5 mW. The spectra were fitted with a Lorentzian band shape function using the Fityk software.²⁴

2.4. Oscillatory barrier measurements

For oscillatory barrier measurements, two platinum Wilhelmy plates were used to measure the surface pressure at the same time, placed as illustrated in Fig. 2. The floating films were compressed to the surface pressure value of $\Pi_{\parallel} = 37.5$ mN m⁻¹. The amount of used MWCNT suspension was readjusted to

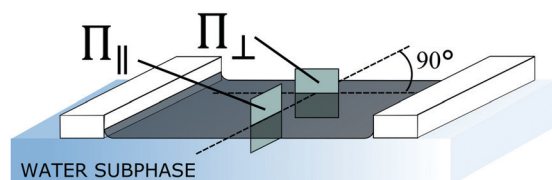


Fig. 2 Schematic of Langmuir trough showing Wilhelmy plate configurations; surface pressure measured in parallel (Π_{\parallel}) and perpendicular (Π_{\perp}) direction with respect to the barrier position.

achieve a layer of exactly 200 cm² at this surface pressure. The surface pressure was maintained for 30 min in order to improve homogeneity of the layer and to reproduce the same conditions as used in the transfer process. Then a series of 10 barrier oscillations at a rate of 20 mHz with a strain of 0.5% ($\Delta A/A_0$, where ΔA is the amplitude of the film surface area change and A_0 is the film surface area at which changes occur) were performed and the Π - A (surface pressure vs. area) measurements were recorded. The strain and pressure were selected to ensure that during measurements the pressure would not exceed the value at which the compressibility module starts to decrease to avoid the risk of the film damage. These measurements were made several times for each suspension. The obtained results were within the limits of the calculated measurement uncertainty.

3. Results and discussion

3.1. Thermodynamics of Langmuir layers

In Fig. 3 the surface pressure (Π) in relation to the area per mass unit of the used MWCNT (A_r) was shown (Π - A_r isotherms). The surface pressure was measured simultaneously in the parallel (Π_{\parallel})

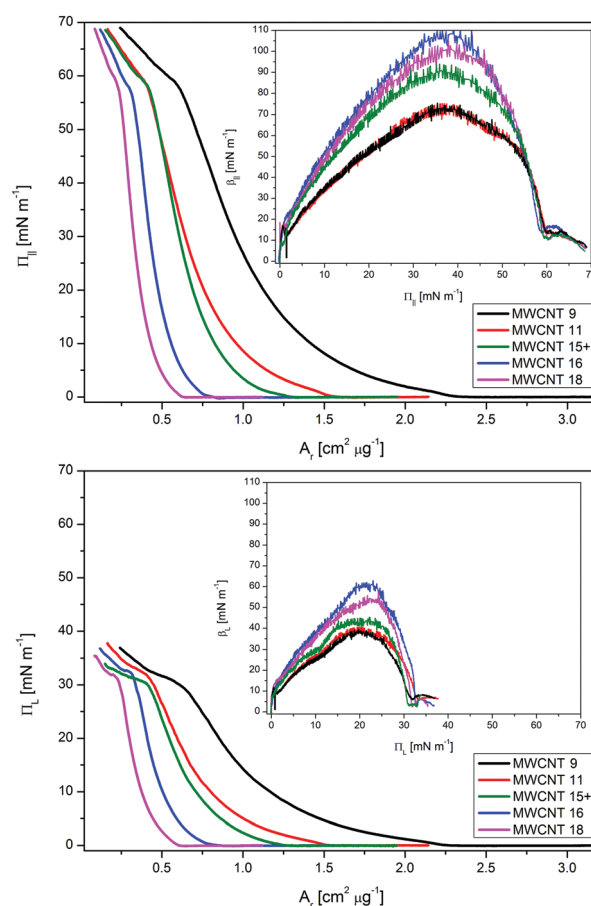


Fig. 3 Dependence of surface pressure measured in parallel (top; Π_{\parallel}) and perpendicularly (bottom; Π_{\perp}) direction on the surface area per 1 μ g of used MWCNT (A_r). The inserts contain the compressibility modules of the corresponding films measured in parallel (top; β_{\parallel}) and perpendicularly (bottom; β_{\perp}) direction.

and perpendicular (Π_{\perp}) direction. For the MWCNT suspension in concentrations lower than those used for further studies, the Π - A_r isotherms were almost identical to those presented in Fig. 3, which indicates that the material was well dispersed. The anisotropy of surface pressure with respect to the Wilhelmy plate position was clearly visible. Almost twice higher surface pressure was recorded in parallel direction when compared to that in perpendicular direction in the same area at any given point for all MWCNT films. The observed difference suggests that the layer is characterized by a finite shear modulus. With increasing MWCNT diameters, a significant decrease in A_r value can be observed. It is explained as a result of growing films density with raising MWCNT diameter and increased empty spaces in the layer composed of MWCNT with small diameters (see Fig. 4). In order to determine the repeatable conditions for transferring process, the compressibility modulus (β) was calculated as:²⁵

$$\beta = -A_r \left(\frac{\partial \Pi}{\partial A_r} \right)$$

where Π is the surface pressure measured with respect to the barriers placement and A_r is the trough area per unit mass of used MWCNT. The compressibility modulus vs. surface pressure is shown in the insert of Fig. 3. The maximum value of β_{\parallel} was observed for Π_{\parallel} at about 40 mN m^{-1} regardless of the used MWCNT material. On the other hand, in perpendicular direction the maximum value of β_{\perp} was measured at a surface pressure between 20 mN m^{-1} and 23.5 mN m^{-1} and this value increased with increasing MWCNT diameter. Therefore, the anisotropy of the layers should depend on the diameter of the used MWCNT. It was not possible to define a correlation between the maximum values of β and MWCNT diameter due to the facts described below. The compression rate need to be quasi-static since the value of β does not take into account the influence of dissipative forces and the existence of a finite shear modulus.^{26,27}

Despite this drawback the compressibility modulus can be used as an indicator of the Langmuir layers morphology. The increase in the compressibility modulus leads to obtaining more densely packed layers, however when the maximum value of the modulus is exceeded, the layer begins to crack or its fragments overlap. The surface pressure $\Pi_{\parallel} = 37.5 \text{ mN m}^{-1}$ was chosen taking into account the following factors:

1. Π_{\parallel} value at maximum β_{\parallel} was constant irrespective of the MWCNT diameter in the layers, in contrast to Π_{\perp} value at maximum β_{\perp} , so the constant parameters were chosen which allows better control of the transfer process,

2. Observed anisotropy increased with increasing surface pressure so the highest possible Π_{\parallel} value was chosen,

3. In order to protect the film against irreversible changes the oscillatory barrier measurements have to be performed for Π_{\parallel} not exceeding 40 mN m^{-1} at any given point. The highest possible surface pressure ensuring meeting this condition was 37.5 mN m^{-1} .

Results of the oscillatory barrier measurements allow determination of the complex compression (ε^*) and shear (G^*) moduli. The real components represent the energy stored as

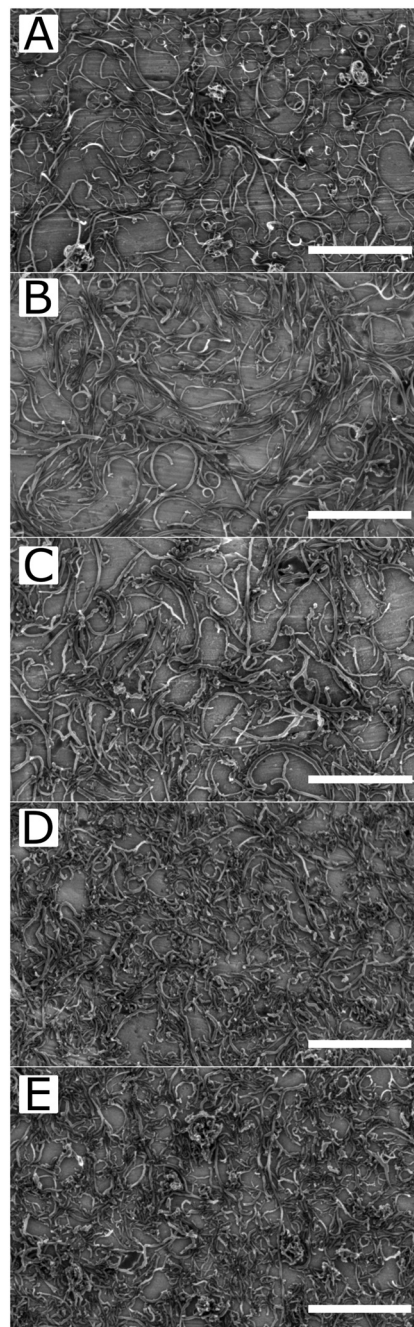


Fig. 4 SEM images of various MWCNT films transferred at surface pressure of 37.5 mN m^{-1} onto aluminum foil (A – MWCNT 9, B – MWCNT 11, C – MWCNT 15+, D – MWCNT 16, E – MWCNT 18); scale represents $1 \mu\text{m}$.

purely elastic fraction, while the imaginary components represent the energy dissipated in system as friction or plastic deformations. All the components can be calculated using the following set of equations:^{27,28}

$$|\varepsilon^* + G^*| = A_0 \frac{\Delta \Pi_{\parallel}}{\Delta A}$$

$$|\varepsilon^* - G^*| = A_0 \frac{\Delta \Pi_{\perp}}{\Delta A}$$

Table 1 Mechanical parameters where: ε^* is the complex compression modulus with its corresponding real (ε') and imaginary (ε'') part and G^* is the complex shear modulus with its corresponding real (G') and imaginary (G'') part

Film name	ε' [mN m ⁻¹]	ε'' [mN m ⁻¹]	G' [mN m ⁻¹]	G'' [mN m ⁻¹]	$ \varepsilon^* + G^* $ [mN m ⁻¹]	$ \varepsilon^* - G^* $ [mN m ⁻¹]
MWCNT 9	171.9 ± 1.3	59.5 ± 1.1	71.3 ± 1.1	23.6 ± 1.1	256.6 ± 0.9	106.6 ± 0.4
MWCNT 11	171.8 ± 1.2	60.4 ± 1.1	87.6 ± 1.2	25.8 ± 1.1	273.4 ± 0.8	90.9 ± 0.3
MWCNT 15+	250.6 ± 1.5	92.7 ± 1.1	97.0 ± 1.4	31.0 ± 1.1	369.0 ± 1.1	165.5 ± 0.5
MWCNT 16	296.7 ± 1.5	106.5 ± 1.1	107.2 ± 1.5	37.8 ± 1.1	428.9 ± 1.4	201.5 ± 0.5
MWCNT 18	252.5 ± 1.5	99.5 ± 1.1	101.2 ± 1.5	39.6 ± 1.1	380.0 ± 1.2	162.6 ± 0.5

$$\varepsilon' = \frac{1}{2} A_0 \left[\frac{\Delta \Pi_{\parallel}}{\Delta A} \cos(\varphi_{\parallel}) + \frac{\Delta \Pi_{\perp}}{\Delta A} \cos(\varphi_{\perp}) \right]$$

$$G' = \frac{1}{2} A_0 \left[\frac{\Delta \Pi_{\parallel}}{\Delta A} \cos(\varphi_{\parallel}) - \frac{\Delta \Pi_{\perp}}{\Delta A} \cos(\varphi_{\perp}) \right]$$

$$\varepsilon'' = \frac{1}{2} A_0 \left[\frac{\Delta \pi_{\parallel}}{\Delta A} \sin(\varphi_{\parallel}) + \frac{\Delta \pi_{\perp}}{\Delta A} \sin(\varphi_{\perp}) \right]$$

$$G'' = \frac{1}{2} A_0 \left[\frac{\Delta \pi_{\parallel}}{\Delta A} \sin(\varphi_{\parallel}) - \frac{\Delta \pi_{\perp}}{\Delta A} \sin(\varphi_{\perp}) \right]$$

where A_0 is the constant area of the Langmuir film around which the surface of ΔA amplitude is changed, φ are the phase shifts values between barrier motion and its corresponding surface pressure response $\Delta \Pi$, with respect to the barriers placement. The fitting procedure and determination of the measurements uncertainty was described in detail in ESI† and all obtained results are summarized in Table 1. Significantly higher $|\varepsilon^* + G^*|$ and $|\varepsilon^* - G^*|$ values were observed when compared with β_{\parallel} and β_{\perp} , respectively, while maintaining the trends shown in Fig. 3. The difference between these values was due to the relaxation process which made the layer more densely packed. MWCNT of greater diameters are more resistant to bending than those of smaller diameters, so the mechanical parameters of the films should increase with increasing MWCNT diameter. It was observed for all films except that with MWCNT diameters of 18 nm. However, this might be the effect of slightly more agglomerated structures in film MWCNT 18 than in film MWCNT 16 (see Fig. 4).

3.2. Films morphology

Fig. 4 presents SEM images of the MWCNT thin layers transferred on the aluminum foil. The layers consisted of tangled nanotubes with barely visible anisotropy of alignment. The individual MWCNT and nanotubes bundles create disordered nets with multiple carbon nanotubes junctions. The images show the presence of uncovered substrate whose area is reduced with growing diameters of nanotubes in the films. In other words, the layer packing density increases with increasing MWCNT diameter. A significant difference in the packing density can be observed for MWCNT 9 and MWCNT 18 films presented in Fig. 4A and E, respectively. Furthermore, MWCNT 9 and MWCNT 11 films (Fig. 4A and B) have similar arrangement in shape of loops and bundles with a small curvature. In the films marked as MWCNT 15+, MWCNT 16 and MWCNT 18 (Fig. 4C–E) the shapes of MWCNT bundles are much more irregular, when compared to those in the MWCNT 9 and MWCNT 11 (Fig. 4A and B) in which smooth loops and twists are much more common.

3.3. Optical properties

In order to determine the optical properties of the MWCNT layers, the transmittance spectra in the range of 190–900 nm were recorded (Fig. 5). With increasing diameter of MWCNT, the transmittance of the obtained film decreased. The lower transmittance of the films consisting of MWCNT of greater diameters was a consequence of both higher packing of MWCNT in films and higher probability of light absorption by the material with greater wall thickness. The obtained spectra showed the bands assigned to π to π^* interband transitions (400–900 nm) and the π -plasmon band located in the UV range.³⁰ The position of the π -plasmon band is related to the carbon nanotubes diameters. For SWCNT a red shift was observed as the diameters increased. The energy of the plasmon band is inversely proportional to the square of the diameter.²⁹ It is a well-known phenomenon and can be also observed in metallic nanorods.^{31–33} In our studies, a blue shift instead of a red shift of the π -plasmon band was observed with increasing MWCNT diameter.

The derivative of transmittance spectra (ESI,† Fig. S1) indicates a shift of the π -plasmon band from about 273 nm (4.54 eV) for the film MWCNT 9 to 258 nm (4.81 eV) for MWCNT 18. The differences in the π -plasmon band positions were relatively small (see insert in the Fig. 5), but they cannot be neglected. Moreover the π -plasmon band position and the corresponding transmittance value in polarized light vs. the diameter of the used MWCNT is shown in ESI,† in Fig. S2.

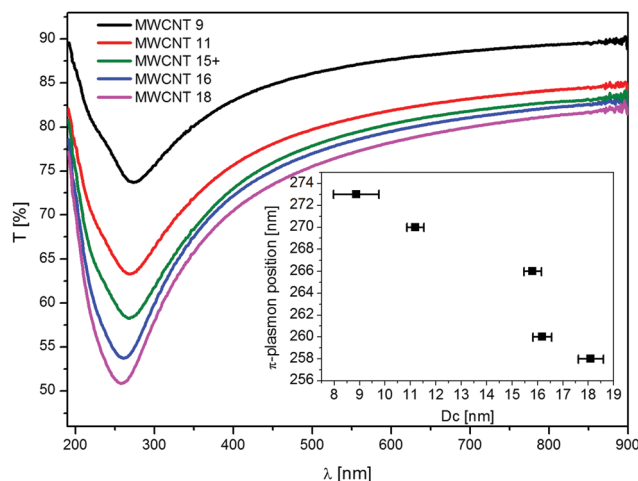


Fig. 5 UV-vis transmittance spectra for LS films of various MWCNT diameters. The insert contain π -plasmon band position vs. outer diameter (D_c) of the used MWCNT.

The position of the π -plasmon band may be affected by other factors than the outer diameter of MWCNT. Brzhezinskaya *et al.* have reported a red shift of the π -plasmon peak with increasing dose of Ar⁺ radiation.³⁴ A significant change in this band position was observed for doses below 100 $\mu\text{C cm}^{-2}$. Above this value, the band position remained almost unchanged. The radiation dose can be strictly correlated with the amount of defects in MWCNT. The number of defects can be evaluated on the basis of the ratio of the intensities of D and G bands I_D/I_G obtained by Raman spectroscopy measurement.³⁵ The obtained results of Raman investigation of all tested MWCNT films in both powder and film form are shown in ESI† (Tables S2, S3 and Fig. S5, S6). For the powders MWCNT 9, MWCNT 11 and MWCNT 15+ the obtained I_D/I_G ratios were very close to 1.9, while a slight increase in these values was observed for the remaining two samples. Moreover, the values of I_D/I_G ratios obtained for the films were almost the same as those obtained for the powders, which confirms that the sonication process did not cause damage. Taking into account the above, if the number of defects was the dominant factor determining the π -plasmon band position, the position of this band for MWCNT 9 film would be blue shifted relative to its positions in the other films, which was not observed. For this reason we believe that the number of defects is not the dominant factor of the plasmon band wavelength shift.

The derivative transmittance spectra (ESI,† Fig. S1) show isosbestic point at about 244 nm, which suggests the presence of at least two components in the recorded π -plasmon bands. Two well resolved maxima in the UV band have been reported for SWCNT, in spectra of graphite and other carbon allotropes.^{36,37} According to literature data, the π -plasmon band of SWCNT consists of two components: a high energy one located at 236 nm (5.26 eV) and a low energy one located between 275 nm (4.2 eV) and 295 nm (4.5 eV). The low energy component originates from the plasmon excitation along the tube axis, while the high energy one originates from the plasmon excitation in the perpendicular direction.^{36,38} Moreover, relative intensity of both plasmon bands depends on the orientation of CNT with respect to the light electric vector polarization. According to Murakami *et al.*, the absorbance at 275 nm increases when the angle between the electric vector and the tube axis decrease, while the absorbance at 236 nm remains unchanged.³⁶ This effect suggest that the π -plasmon band shift can be a result of the MWCNT alignment and thus the relative change in the intensity of its two components. This theory is partially contradicted by the data obtained from UV-vis spectra in polarized light. The band shift resulting from MWCNT orientation (see ESI,† Fig. S2) is a major factor in the obtained results.

According to Lucas *et al.*, for the multishell fullerenes the plasmon band position depends on the ratio of the inner to outer diameter (r/R).³⁹ They postulate that while the r/R ratio decreases, the plasmon band position is shifted towards UV, reaching saturation for $r/R < 0.5$. For the MWCNT studied, the r/R ratios were of about 0.3 for all films (see Fig. 1), which suggests that the observed band should not be shifted. However, Lucas *et al.* have performed calculations assuming a

constant value of the outer diameter of fullerenes ($R = 10$ nm). The outer diameter of the MWCNT we studied varied from 8.86 nm to 18.1 nm. In order to be able to compare the obtained results, it is necessary to consider the influence of the wall thickness of both materials. The wall thickness of the MWCNT we studied varied in the range between 3 nm and 6 nm. Comparing the results obtained for both materials we obtain the position of the bands at 203–238 nm (depending on the surrounding environment of fullerene) vs. 258 nm (MWCNT on quartz) for 6 nm wall thickness and 229–258 nm (depending on the surrounding environment of fullerene) vs. 272 nm (MWCNT on quartz) for 3 nm wall thickness. While the direction of the band position shift along with the change in wall thickness is the same as for fullerenes, their positions differ for the two types of samples. However, it is important to realize that unlike the plasmon band for fullerene, the one for MWCNT consists of two components, which affects its position. In Fig. S4 (ESI†) position of three spectra components vs wall thickness were shown. The data were fitted by three Voigt function in the Fityk 1.3.1 software.²⁴ Energy of the two π -plasmon band components increases as the wall thickness increases. Minor changes in position of high energy component (212–216 nm; 5.74–5.84 eV), while the most significant changes were observed for the low energy component of π -plasmon band position (252–270 nm; 4.58–4.91 eV). This suggest that the low energy component can be correlated with the wall thickness. Unfortunately, the statistical distribution of wall thickness is too wide for such a correlation to be certain. However, we believe that the study of MWCNT with better defined wall thicknesses will allow to confirm this relationship in the future.

3.4. Electrical properties

Fig. 6 presents the surface resistivity of the transferred MWCNT films measured in the directions parallel ($R_{S\parallel}$) and perpendicular ($R_{S\perp}$) to the barrier position before and after the annealing process.²⁰ The latter process was performed for 5 hours in argon atmosphere under a pressure of 1 mbar and at 250 °C. For all

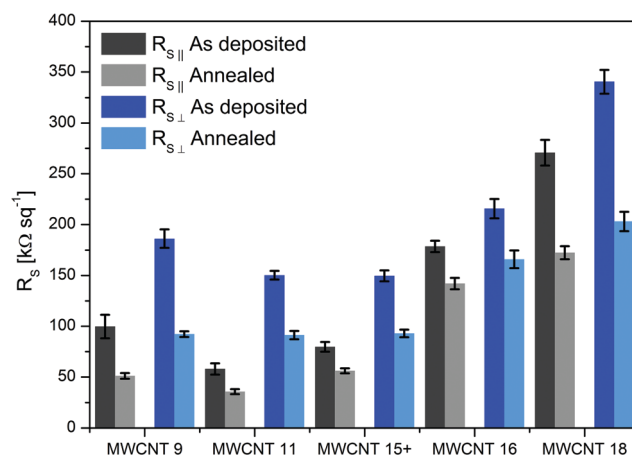


Fig. 6 Surface resistivity of annealed and as deposited MWCNT films measured in parallel (R_{\parallel}) and perpendicular (R_{\perp}) direction relative to the position of the barrier.

measurements, linear current–voltage characteristics were observed in the current range of measurements (from $-1 \mu\text{A}$ to $1 \mu\text{A}$). The lowest surface resistance of $58 \pm 6 \text{ k}\Omega \text{ sq}^{-1}$ and $35.8 \pm 2.4 \text{ k}\Omega \text{ sq}^{-1}$ in parallel to the barrier position was noted for the as deposited and annealed MWCNT 11 film, respectively. Moreover surface resistance gradually increased with increasing or decreasing diameters of MWCNT. On the other hand, the lowest surface resistance of $149 \pm 5 \text{ k}\Omega \text{ sq}^{-1}$ and $91 \pm 4 \text{ k}\Omega \text{ sq}^{-1}$ in perpendicular to the barrier position was noted for the as deposited MWCNT 15+ and the annealed MWCNT 11 films, respectively. Moreover, similar values of $R_{S\perp}$ were observed for the annealed MWCNT 9, MWCNT 11 and MWCNT 15+ films. The annealing process in all cases resulted in a similar decrease in the surface resistivity regardless of the measurement direction. The most significant reduction of surface resistivity (50% of the as deposited value) was recorded for MWCNT 9, while the lowest reduction of surface resistivity (80% of the as deposited value) was observed for MWCNT 16. The changes are most likely supposed to be due to the storage of DCM or water inside carbon nanotubes for the two reasons. Firstly, minor changes were observed when the annealing temperature was set below $100 \text{ }^\circ\text{C}$, which would cause both of these fluids to evaporate from the layer, but would not cause them to evaporate completely from the inside of MWCNT. Secondly, no significant changes between the as deposited and annealed films in Raman and UV-vis spectra were observed, which eliminates the impact of the removal of functional groups or defects from the carbon nanotubes.

3.5. Shear loss tangent as factor limiting the obtained anisotropy

In order to determine the influence of the MWCNT diameter on the electrical anisotropy, the $R_{S\perp}/R_{S\parallel}$ ratio vs. diameter was analyzed (Fig. 7). The highest $R_{S\perp}/R_{S\parallel}$ value of 2.5 ± 0.3 was observed for MWCNT 11 film and for the films with increasing and decreasing diameters the value of this ratio decreased gradually. As expected, the lowest electrical anisotropy was recorded for the layers obtained from the thickest nanotubes.

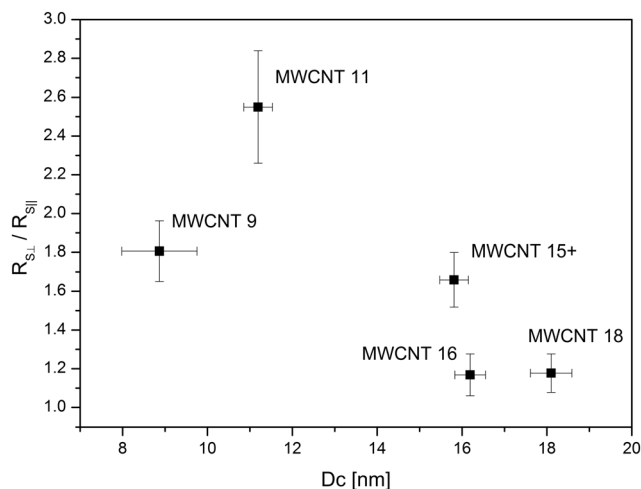


Fig. 7 Electrical anisotropy parameter defined as the ratio of surface resistivities measured in perpendicular to that measured in parallel direction ($R_{S\perp}/R_{S\parallel}$) vs. outer diameter (D_c).

Taking into account previous studies, the highest electrical anisotropy was expected to be obtained for MWCNT 9 film due to the smallest diameter of its particles.^{11,12,20,40} Since the electrical properties of MWCNT in the films MWCNT 9 and MWCNT 11 should be very similar to each other and the anisotropy of the arrangement was caused by the barrier motion, the difference in the $R_{S\perp}/R_{S\parallel}$ value should be reflected in the mechanical parameters of the layers. Jia *et al.* in their work have proposed a model which explained the alignment process of the SWCNT in Langmuir films.¹⁹ According to this model, the relative motion between the SWCNT and the subphase caused the drag torque to align CNT in film. In addition, three main factors have been identified to support the alignment process: the film velocity relative to the subphase, subphase viscosity and aspect ratio of CNT (length to diameter).

The highest anisotropy should be observed for MWCNT 9 film. On the other hand, this model fails if the CNT start to interact with one another, which becomes crucial in the case of MWCNT 9. During the compression of the film, part of the energy applied to the system is converted into two types of viscoelastic deformations: longitudinal and transverse ones, which can be measured by the imaginary part of the complex compression ε'' and complex shear G'' moduli, respectively. The better aligned the CNT, the smaller area they cover. Therefore, the longitudinal viscoelastic deformations are desirable and unavoidable to some extent and ε'' value should be greater than zero. On the other hand, the transverse viscoelastic deformations are highly undesirable, causing bending of the CNT in the arcs and consequently reducing the observed anisotropy. The ratios of the moduli G'' to G' or ε'' to ε' defined as $\tan \delta_G$ or $\tan \delta_E$, respectively, indicate the relative energy dissipation of the material. Fig. 8 shows the effect of shear modulus loss tangent angle ($\tan \delta_G$) on the electrical anisotropy and a similar figure for $\tan \delta_E$ was shown in ESI† (Fig. S7). As expected, the lowest value of $\tan \delta_G$ was obtained for the MWCNT 11 film, for which the highest ratio $R_{S\perp}/R_{S\parallel}$ was obtained and a similar $\tan \delta_G$ value was achieved for films MWCNT 9 and MWCNT 15+. Taking into

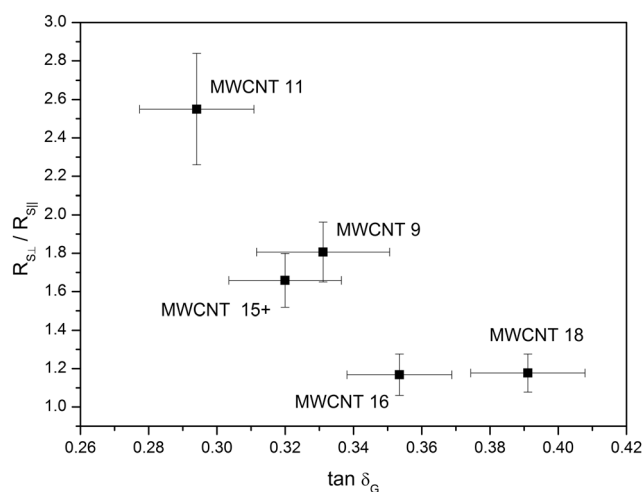


Fig. 8 Dependence of the electrical anisotropy ($R_{S\perp}/R_{S\parallel}$) on the shear loss tangent ($\tan \delta_G$).

account all the above information, it can be concluded that the main factor blocking the alignment process is represented by the $\tan \delta_G$ value and the highest anisotropy should be observed for $\tan \delta_G$ near to zero. Due to the fact that the shear loss tangent can be controlled by parameters such as: pH of the subphase, compression speed, temperature, *etc.* this approach opens up many opportunities for future research.

3.6. MWCNT films as transparent electrodes

The parameter most often used to characterize the relative performance of the films in terms of transparency and sheet resistance, is the ratio of direct current conductivity (σ_{dc}) to optical conductivity (σ_{op}) calculated as:²²

$$\frac{\sigma_{dc}}{\sigma_{op}} = \frac{Z_0}{2R_s(T^{-0.5} - 1)}$$

where $Z_0 = 377 \Omega$ is the impedance of free space, T is the polarized transmittance at 550 nm measured in parallel or perpendicular direction relative to the barrier, and R_s is the surface resistivity measured in parallel or perpendicular direction relative to the barrier. The calculated results are summarized in Fig. 9. The value of the σ_{dc}/σ_{op} is a very useful tool for comparative analysis of transparent electrodes regardless of their thickness and the type of used material. The better the film quality, the higher the σ_{dc}/σ_{op} ratio.

The highest $(\sigma_{dc}/\sigma_{op})_{||}$ ratio of 0.059 ± 0.003 measured in parallel direction with respect to the barrier position was obtained for MWCNT 9 film and for MWCNT 11 film the ratio $(\sigma_{dc}/\sigma_{op})_{||}$ was slightly lower, but within the measurement uncertainty. For the other films the ratio gradually decreased, mainly because of decreasing transmittance. The annealing process did not cause any changes in the UV-vis spectra and thus the difference between the annealed and as deposited films originated only from the removal of impurities from the MWCNT. Moreover, the influence of these impurities was greater for MWCNT with smaller diameters because the electronic

structure of the MWCNT with thinner walls can be more easily disturbed. The anisotropy of the σ_{dc}/σ_{op} ratio is slightly greater than the electrical anisotropy due to the presence of optical anisotropy (see ESI,† Fig. S2). Although it is not surprising that it reduced general performance as a transparent electrode, in some cases the $(\sigma_{dc}/\sigma_{op})_{\perp}$ ratio is irrelevant. For example, the high transparency of the electrodes used for the construction of liquid crystal display to polarized light is sufficient. Also the value of the sheet resistivity in perpendicular direction ($R_{s\perp}$) is irrelevant due to the fact that only the low resistance path can be used. Therefore, only the highest possible σ_{dc}/σ_{op} ratio is relevant. Moreover, CNT film with high optical anisotropy and low surface resistance may prove to be advantageous in devices such as liquid crystal display, where it can replace both the ITO layer and the polarizer. Although the obtained σ_{dc}/σ_{op} values are relatively low in comparison to that obtained for ITO ($\sigma_{dc}/\sigma_{op} > 100$) or other CNT-based films ($\sigma_{dc}/\sigma_{op} = 23$), for the perfectly aligned CNT films similar σ_{dc}/σ_{op} ratios can be achieved without any doping or modification.^{41,42}

4. Conclusions

In summary, the results presented and discussed above have shown that even a small change in MWCNT diameters results in a significant change in the optical, electrical and mechanical properties of Langmuir-Schaefer films. The highest transmittance of 87% was achieved for the film composed of the smallest diameter MWCNT and this value decreased gradually with increasing MWCNT diameter. Moreover, the reverse diameter dependence of π -plasmon band was observed. The most likely explanation for this phenomenon is that the wall thickness of MWCNT affects the location of the low energy component of the π -plasmon band. However, due to the wide statistical distribution of wall thicknesses, these studies must be repeated on better defined samples. In addition to wall thickness the following factors should be taken into account in the comparative analysis: the number of defects, the ratio and position of the two components of the π -plasmon band and the orientation of MWCNT relative to light electrical vector. The lowest surface resistance of $36.8 \pm 2.4 \text{ k}\Omega \text{ sq}^{-1}$ in parallel direction was obtained for the film composed of MWCNT of diameter of 11 nm. All MWCNT films showed both electrical and optical anisotropy and the highest anisotropy was achieved for the film composed of MWCNT of 11 nm in diameter. The values of the complex compression and shear moduli were determined for the first time for MWCNT films. It has been shown that the main factor limiting obtaining highly aligned MWCNT films was the shear loss tangent. Although MWCNT in the films exhibited barely visible anisotropy of placement, high anisotropy of all investigated properties was observed. It is a very important observation especially from the point of view of potential applications of the CNT based transparent electrodes.

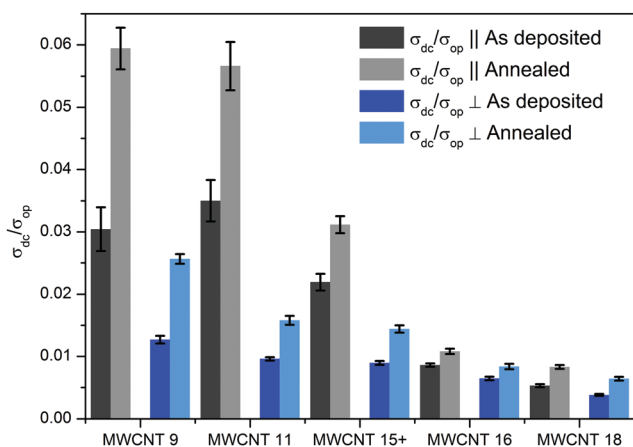


Fig. 9 General performance of MWCNT films as a transparent electrodes calculated from polarized optical conductivity and direct current conductivity measured in parallel ($\sigma_{dc}/\sigma_{op} ||$) and perpendicular direction ($\sigma_{dc}/\sigma_{op} \perp$) for as deposited and annealed films.

Conflicts of interest

There are no conflicts to declare.

Acknowledgements

The work is the result of the research project financed by the National Science Centre of Poland (No. 2016/21/N/ST8/03557). TEM studies were performed with support of NCN project UMO-2016/21/D/ST3/00975. K. K., acknowledge the support of the National Science Centre of Poland (No. 2015/17/N/ST8/00295). A. B., A. S. and D. W. acknowledge the support of the Ministry of Science and Higher Education of Poland.

References

- 1 C. De Las Casas and W. Li, A review of application of carbon nanotubes for lithium ion battery anode material, *J. Power Sources*, 2012, **208**, 74–85.
- 2 K. Rytel, D. Waszak, K. Kędzierski and D. Wróbel, Novel method of current collector coating by multiwalled carbon nanotube Langmuir layer for enhanced power performance of LiMn₂O₄ electrode of Li-ion batteries, *Electrochim. Acta*, 2016, **222**, 921–925.
- 3 V. Schroeder, S. Savagatrup, M. He, S. Lin and T. M. Swager, Carbon nanotube chemical sensors, *Chem. Rev.*, 2019, **119**, 599–663.
- 4 A. V. Eletsii, Carbon nanotube-based electron field emitters, *Usp. Fiz. Nauk*, 2010, **180**, 897.
- 5 S. Park, M. Vosguerichian and Z. Bao, A review of fabrication and applications of carbon nanotube film-based flexible electronics, *Nanoscale*, 2013, **5**, 1727–1752.
- 6 S. B. Yang, B. S. Kong, D. H. Jung, Y. K. Baek, C. S. Han, S. K. Oh and H. T. Jung, Recent advances in hybrids of carbon nanotube network films and nanomaterials for their potential applications as transparent conducting films, *Nanoscale*, 2011, **3**, 1361–1373.
- 7 G. Giancane, S. Bettini and L. Valli, State of art in the preparation, characterisation and applications of Langmuir-Blodgett films of carbon nanotubes, *Colloids Surf., A*, 2010, **354**, 81–90.
- 8 J. Liu, C. Wang, X. Tu, B. Liu, L. Chen, M. Zheng and C. Zhou, Chirality-controlled synthesis of single-wall carbon nanotubes using vapour-phase epitaxy, *Nat. Commun.*, 2012, **3**, 1–7.
- 9 W. Kim, H. C. Choi, M. Shim, Y. Li, D. Wang and H. Dai, Synthesis of Ultralong and High Percentage of Semiconducting Single-walled Carbon Nanotubes, *Nano Lett.*, 2002, **2**, 703–708.
- 10 J. Si, L. Xu, M. Zhu, Z. Zhang and L. M. Peng, CNT Electronics: Advances in High-Performance Carbon-Nanotube Thin-Film Electronics, *Adv. Electron. Mater.*, 2019, **5**, 1900122.
- 11 M. K. Massey, C. Pearson, D. A. Zeze, B. G. Mendis and M. C. Petty, The electrical and optical properties of oriented Langmuir-Blodgett films of single-walled carbon nanotubes, *Carbon N. Y.*, 2011, **49**, 2424–2430.
- 12 Q. Cao, S. J. Han, G. S. Tulevski, Y. Zhu, D. D. Lu and W. Haensch, Arrays of single-walled carbon nanotubes with full surface coverage for high-performance electronics, *Nat. Nanotechnol.*, 2013, **8**, 180–186.
- 13 F. N. Ishikawa, H. Chang, K. Ryu, P. Chen, A. Badmaev, L. G. De-Arco, D. Arco, G. Shen and C. Zhou, Transparent Electronics Based on transfer printed aligned carbon nanotubes on rigid and flexible substrates, *ACS Nano*, 2009, **3**, 73–79.
- 14 Y. Yan, M. B. Chan-Park and Q. Zhang, Advances in carbon-nanotube assembly, *Small*, 2007, **3**, 24–42.
- 15 Y. Ma, B. Wang, Y. Wu, Y. Huang and Y. Chen, The production of horizontally aligned single-walled carbon nanotubes, *Carbon N. Y.*, 2011, **49**, 4098–4110.
- 16 G. Modugno, Z. Syrgiannis, A. Bonasera, M. Carraro, G. Giancane, L. Valli, M. Bonchio and M. Prato, The supra-molecular design of low-dimensional carbon nano-hybrids encoding a polyoxometalate-bis-pyrene tweezer, *Chem. Commun.*, 2014, **50**, 4881–4883.
- 17 V. Sgobba, G. Giancane, D. Cannoletta, A. Operamolla, O. Hassan Omar, G. M. Farinola, D. M. Guldi and L. Valli, Langmuir-schaefer films for aligned carbon nanotubes functionalized with a conjugate polymer and photoelectrochemical response enhancement, *ACS Appl. Mater. Interfaces*, 2014, **6**, 153–158.
- 18 G. Giancane, A. Ruland, V. Sgobba, D. Manno, A. Serra, G. M. Farinola, H. Omar, D. M. Guidi and L. Valli, Aligning single-walled carbon nanotubes by means of Langmuir-Blodgett film deposition: Optical, morphological, and photoelectrochemical studies, *Adv. Funct. Mater.*, 2010, **20**, 2481–2488.
- 19 L. Jia, Y. Zhang, J. Li, C. You and E. Xie, Aligned single-walled carbon nanotubes by Langmuir-Blodgett technique, *J. Appl. Phys.*, 2008, **104**, 074318.
- 20 K. Kędzierski, K. Rytel, Ł. Majchrzycki and D. Wróbel, Conductive and transparent films of oriented multi-walled carbon nanotubes by Langmuir-Schaefer method, *Thin Solid Films*, 2015, **589**, 701–706.
- 21 K. Kędzierski, K. Rytel, B. Barszcz, A. Gronostaj, Ł. Majchrzycki and D. Wróbel, Unusual conductivity temperature dependence of multiwalled carbon nanotube thin film, *Chem. Phys. Lett.*, 2018, **712**, 144–148.
- 22 K. Rytel, M. Widelicka, D. Łukawski, F. Lisiecki, K. Kędzierski and D. Wróbel, Ultrasonication-induced sp³ hybridization defects in Langmuir-Schaefer layers of turbostratic graphene, *Phys. Chem. Chem. Phys.*, 2018, **20**, 12777–12784.
- 23 K. Kędzierski, K. Rytel, B. Barszcz, A. Gronostaj, Ł. Majchrzycki and D. Wróbel, On the temperature dependent electrical resistivity of CNT layers in view of Variable Range Hopping models, *Org. Electron.*, 2017, **43**, 253–261.
- 24 M. Wojdyr, Fityk: A general-purpose peak fitting program, *J. Appl. Crystallogr.*, 2010, **43**, 1126–1128.
- 25 A. Wamke, K. Dopierała, K. Prochaska, H. Maciejewski, A. Biadasz and A. Dudkowiak, Characterization of Langmuir monolayer, Langmuir – Blodgett and Langmuir – Schaefer films formed by POSS compounds, *Colloids Surf., A*, 2015, **464**, 110–120.
- 26 P. Cicuta and E. M. Terentjev, Viscoelasticity of a protein monolayer from anisotropic surface pressure measurements, *Eur. Phys. J. E: Soft Matter Biol. Phys.*, 2005, **16**, 147–158.
- 27 P. Cicuta, Compression and shear surface rheology in spread layers of β -casein and β -lactoglobulin, *J. Colloid Interface Sci.*, 2007, **308**, 93–99.

- 28 K. L. Harrison, L. B. Biedermann and K. R. Zavadil, Mechanical Properties of Water-Assembled Graphene Oxide Langmuir Monolayers: Guiding Controlled Transfer, *Langmuir*, 2015, **31**, 9825–9832.
- 29 G. A. Rance, D. H. Marsh, R. J. Nicholas and A. N. Khlobystov, UV-vis absorption spectroscopy of carbon nanotubes: Relationship between the π -electron plasmon and nanotube diameter, *Chem. Phys. Lett.*, 2010, **493**, 19–23.
- 30 B. W. Reed and M. Sarikaya, Electronic properties of carbon nanotubes by transmission electron energy-loss spectroscopy, *Phys. Rev. B: Condens. Matter Mater. Phys.*, 2001, **64**, 1–13.
- 31 J. Cao, T. Sun and K. T. V. Grattan, Gold nanorod-based localized surface plasmon resonance biosensors: A review, *Sens. Actuators, B*, 2014, **195**, 332–351.
- 32 P. Błaszkiwicz, M. Kotkowiak, E. Coy and A. Dudkowiak, Tailoring Fluorescence and Singlet Oxygen Generation of a Chlorophyll Derivative and Gold Nanorods via a Silica Shell, *J. Phys. Chem. C*, 2020, **124**, 2088–2095.
- 33 P. Błaszkiwicz, M. Kotkowiak, E. Coy and A. Dudkowiak, Laser-Induced Optoacoustic Spectroscopy Studies of Inorganic Functionalized Metallic Nanorods, *J. Phys. Chem. C*, 2019, **123**, 27181–27186.
- 34 M. M. Brzhezinskaya, E. M. Baitinger and V. V. Shnitov, Π -Plasmons in Ion-Irradiated Multiwall Carbon Nanotubes, *Phys. B*, 2004, **348**, 95–100.
- 35 M. S. Dresselhaus, A. Jorio, A. G. Souza Filho and R. Saito, Defect characterization in graphene and carbon nanotubes using Raman spectroscopy, *Philos. Trans. R. Soc., A*, 2010, **368**, 5355–5377.
- 36 Y. Murakami, E. Einarsson, T. Edamura and S. Maruyama, Polarization dependent optical absorption properties of single-walled carbon nanotubes and methodology for the evaluation of their morphology, *Carbon N. Y.*, 2005, **43**, 2664–2676.
- 37 X. Huang, R. S. Mclean and M. Zheng, High-resolution length sorting and purification of DNA-wrapped carbon nanotubes by size-exclusion chromatography, *Anal. Chem.*, 2005, **77**, 6225–6228.
- 38 W. Cheung, M. Patel, Y. Ma, Y. Chen, Q. Xie, J. V. Lockard, Y. Gao and H. He, π -Plasmon absorption of carbon nanotubes for the selective and sensitive detection of Fe^{3+} ions, *Chem. Sci.*, 2016, **7**, 5192–5199.
- 39 A. A. Lucas, Electron Inelastic Scattering Cross Section, *Phys. Rev. B: Condens. Matter Mater. Phys.*, 1994, **49**, 2888–2896.
- 40 K. Kędzierski, B. Barszcz, A. Biadasz, M. Matczak and D. Wróbel, Preparation and studies of transparent conductive monolayers of multiwall carbon nanotubes on quartz and flexible polymer with the use of modified Langmuir technique, *Prog. Org. Coat.*, 2015, **86**, 86–95.
- 41 J. Y. Lee, S. T. Connor, Y. Cui and P. Peumans, Solution-processed metal nanowire mesh transparent electrodes, *Nano Lett.*, 2008, **8**, 689–692.
- 42 S. L. Hellstrom, M. Vosgueritchian, R. M. Stoltenberg, I. Irfan, M. Hammock, Y. B. Wang, C. Jia, X. Guo, Y. Gao and Z. Bao, Strong and stable doping of carbon nanotubes and graphene by MoOx for transparent electrodes, *Nano Lett.*, 2012, **12**, 3574–3580.

Supporting Information

The influence of diameter of multiwalled carbon nanotubes on mechanical, optical and electrical properties of Langmuir-Schaefer films

Karol Rytel^{*a}, Kamil Kędzierski^a, Bolesław Barszcz^b, Małgorzata Widelicka^b, Alicja Stachowiak^a, Andrzej Biadasz^a, Łukasz Majchrzycki^c, Emerson Coy^d, Danuta Wróbel^a

^aFaculty of Materials Engineering and Technical Physics, Institute of Physics, Poznan University of Technology, Piotrowo 3, 60-965 Poznań, Poland

^bInstitute of Molecular Physics, Polish Academy of Sciences, Smoluchowskiego 17, 60-179 Poznań, Poland

^cCentre for Advanced Technology, Adam Mickiewicz University, Uniwersytetu Poznańskiego 10, 60-780 Poznań, Poland

^dNanoBioMedical Centre, Adam Mickiewicz University, Umultowska 85, 61-614 Poznań, Poland

Oscillatory Barrier Measurements

During one measurement following three signals with full 10 cycles was registered: surface pressure measured in parallel direction vs. time (Π_{\parallel} vs. t), surface pressure measured in perpendicular direction vs time (Π_{\perp} vs t) and area between the barriers vs. time (A vs. t). To determine the ΔA and $\Delta \Pi$ amplitudes and phase shifts φ Origin 8.1 sine fit function was used for all obtained signals:

$$y = y_0 + C \sin\left(\pi \frac{x - x_c}{w}\right), (S1)$$

To provide better clarity the subscript contains information (\parallel for Π_{\parallel} vs t ; \perp for Π_{\perp} vs t ; A for A vs t) about the signal from which the data were obtained. The value of φ and the phase shifts error $\Delta \varphi$ were defined as follows:

$$\varphi_{\parallel} = \left(\frac{x_{c\parallel}}{w_{\parallel}} - \frac{x_{cA}}{w_A}\right)\pi - \pi, (S2)$$

$$\Delta\varphi_{\parallel} = \left|\frac{\Delta x_{c\parallel}}{w_{\parallel}}\pi\right| + \left|\frac{\Delta x_{cA}}{w_A}\pi\right| + \left|\frac{x_{c\parallel}}{w_{\parallel}^2}\Delta w_{\parallel}\pi\right| + \left|\frac{x_{cA}}{w_A^2}\Delta w_A\pi\right|, (S3)$$

$$\varphi_{\perp} = \left(\frac{x_{c\perp}}{w_{\perp}} - \frac{x_{cA}}{w_A}\right)\pi - \pi, (S3)$$

$$\Delta\varphi_{\perp} = \left|\frac{\Delta x_{c\perp}}{w_{\perp}}\pi\right| + \left|\frac{\Delta x_{cA}}{w_A}\pi\right| + \left|\frac{x_{c\perp}}{w_{\perp}^2}\Delta w_{\perp}\pi\right| + \left|\frac{x_{cA}}{w_A^2}\Delta w_A\pi\right|. (S3)$$

Because reducing the area between the barriers leads to an increase in surface pressure and the signal A vs. t is shifted in phase by π in relation to the barrier position vs. time in equation S2 and S3 we subtract π .

The real part of compression modulus and its measurement error can be defined as:

$$\varepsilon' = \frac{|\varepsilon^* + G^*|\cos(\varphi_{\parallel}) + |\varepsilon^* - G^*|\cos(\varphi_{\perp})}{2}, (S4)$$

$$\Delta\varepsilon' = \left| \frac{1}{2} \cos(\varphi_{\parallel}) \Delta|\varepsilon^* + G^*| \right| + \left| \frac{1}{2} \cos(\varphi_{\perp}) \Delta|\varepsilon^* - G^*| \right| + \left| \frac{1}{2} |\varepsilon^* + G^*| \sin(\varphi_{\parallel}) \Delta\varphi_{\parallel} \right| + \left| \frac{1}{2} |\varepsilon^* - G^*| \sin(\varphi_{\perp}) \Delta\varphi_{\perp} \right|, (S5)$$

The real part of shear modulus and its measurement error can be defined as:

$$G' = \frac{|\varepsilon^* + G^*| \cos(\varphi_{\parallel}) - |\varepsilon^* - G^*| \cos(\varphi_{\perp})}{2}, (S6)$$

$$\Delta G' = \left| \frac{1}{2} \cos(\varphi_{\parallel}) \Delta|\varepsilon^* + G^*| \right| + \left| \frac{1}{2} \cos(\varphi_{\perp}) \Delta|\varepsilon^* - G^*| \right| + \left| \frac{1}{2} |\varepsilon^* + G^*| \sin(\varphi_{\parallel}) \Delta\varphi_{\parallel} \right| + \left| \frac{1}{2} |\varepsilon^* - G^*| \sin(\varphi_{\perp}) \Delta\varphi_{\perp} \right|, (S7)$$

The imaginary part of compression modulus and its measurement error can be defined as:

$$\varepsilon'' = \frac{|\varepsilon^* + G^*| \sin(\varphi_{\parallel}) + |\varepsilon^* - G^*| \sin(\varphi_{\perp})}{2}, (S8)$$

$$\Delta\varepsilon'' = \left| \frac{1}{2} \sin(\varphi_{\parallel}) \Delta|\varepsilon^* + G^*| \right| + \left| \frac{1}{2} \sin(\varphi_{\perp}) \Delta|\varepsilon^* - G^*| \right| + \left| \frac{1}{2} |\varepsilon^* + G^*| \cos(\varphi_{\parallel}) \Delta\varphi_{\parallel} \right| + \left| \frac{1}{2} |\varepsilon^* - G^*| \cos(\varphi_{\perp}) \Delta\varphi_{\perp} \right|. (S9)$$

The imaginary part of shear modulus and its measurement error can be defined as:

$$G'' = \frac{|\varepsilon^* + G^*| \sin(\varphi_{\parallel}) - |\varepsilon^* - G^*| \sin(\varphi_{\perp})}{2}, (S10)$$

$$\Delta G'' = \left| \frac{1}{2} \sin(\varphi_{\parallel}) \Delta|\varepsilon^* + G^*| \right| + \left| \frac{1}{2} \sin(\varphi_{\perp}) \Delta|\varepsilon^* - G^*| \right| + \left| \frac{1}{2} |\varepsilon^* + G^*| \cos(\varphi_{\parallel}) \Delta\varphi_{\parallel} \right| + \left| \frac{1}{2} |\varepsilon^* - G^*| \cos(\varphi_{\perp}) \Delta\varphi_{\perp} \right|, (S11)$$

Where:

$$|\varepsilon^* + G^*| = A_0 \frac{\Delta\Pi_{\parallel}}{\Delta A} = \frac{y_{0A} C_{\parallel}}{C_A}, (S12)$$

$$\Delta|\varepsilon^* + G^*| = \left(\frac{\Delta y_{0A}}{y_{0A}} + \frac{\Delta C_{\parallel}}{C_{\parallel}} + \frac{\Delta C_A}{C_A} \right) * |\varepsilon^* + G^*|, (S13)$$

$$|\varepsilon^* - G^*| = A_0 \frac{\Delta\Pi_{\perp}}{\Delta A} = \frac{y_{0A} C_{\perp}}{C_A}, (S14)$$

$$\Delta|\varepsilon^* - G^*| = \left(\frac{\Delta y_{0A}}{y_{0A}} + \frac{\Delta C_{\perp}}{C_{\perp}} + \frac{\Delta C_A}{C_A} \right) * |\varepsilon^* - G^*|, (S15)$$

The measurement error of obtained compression and shear moduli (presented in Table 2 in main text) appear to be very low. It was decided to check how much reproducible results will be obtained for the layers obtained from MWCNT 9 sample. The results of four independent measurements were shown in Table S1. Most of the received results were within the limits of the measurement uncertainty and the deviations that occur were originated from the inhomogeneity of the layer formed after MWCNT suspension has been applied on the air water interface. The measurement of layer designated as MWCNT 9 was selected for analysis

in the main text due to the lowest uncertainty of measurement and the closest to sinusoidal signals Π_{\parallel} vs. t and Π_{\perp} vs. t .

Table S1 The mechanical parameters of the Langmuir films obtained from the powder labeled as MWCNT 9

Film name	ϵ' [mN m ⁻¹]	ϵ'' [mN m ⁻¹]	G' [mN m ⁻¹]	G'' [mN m ⁻¹]
MWCNT 9	171.9 ± 1.3	59.5 ± 1.1	71.3 ± 1.1	23.6 ± 1.1
MWCNT 9.2	175.9 ± 3.2	61.0 ± 3.2	66.4 ± 3.3	19.7 ± 3.2
MWCNT 9.3	175 ± 3	62 ± 2	65 ± 5	19.9 ± 1.7
MWCNT 9.4	173.3 ± 1.5	62.9 ± 1.3	67.1 ± 1.5	21.6 ± 1.4

UV-Vis spectra

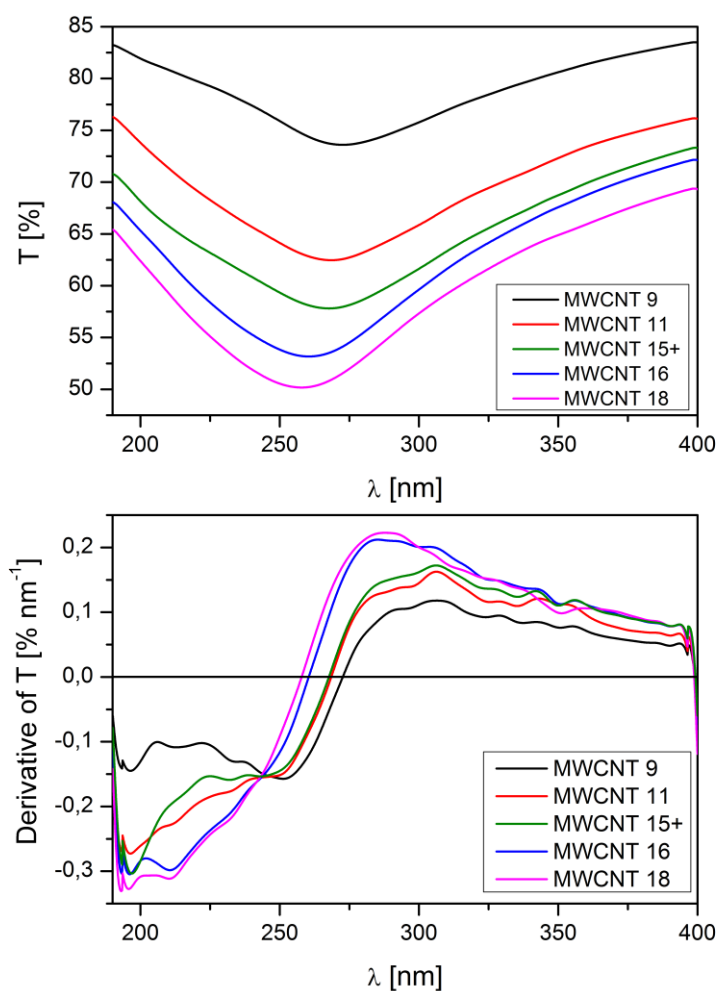


Fig. S1 UV transmittance spectra recorded at 0.3 nm step (top) and its derivative (bottom)

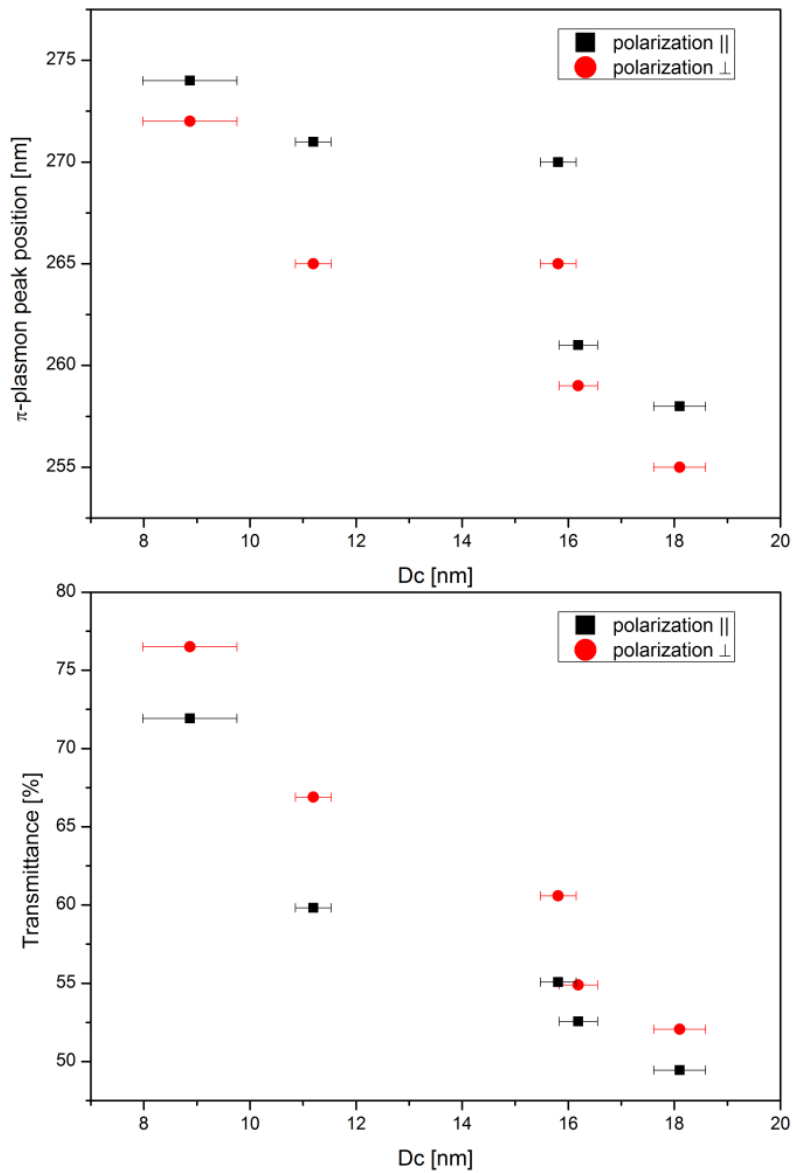


Fig. S2 Plasmon band position (top) and corresponding transmittance value (bottom) vs. diameter of the used MWCNT for electric vector polarization parallel and perpendicular to the barrier orientation

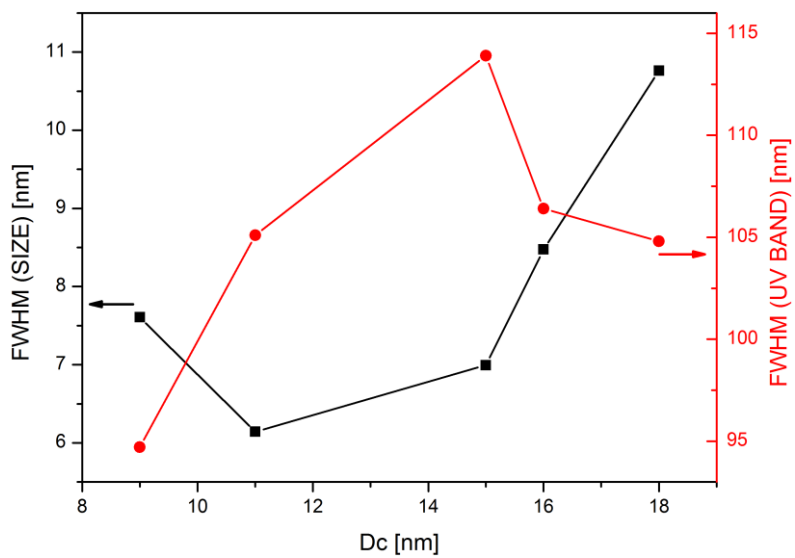


Fig. S3 The full width at half maximum (FWHM) of UV bands and diameter size

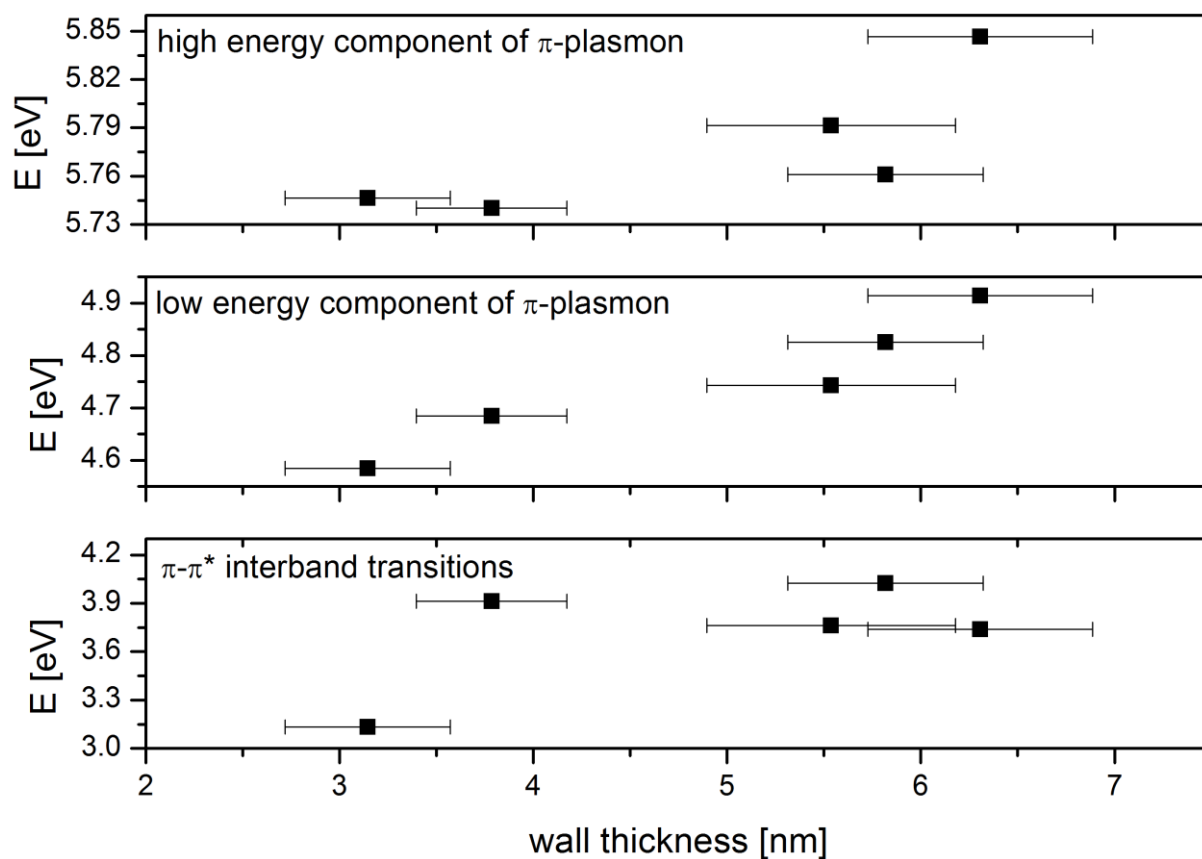


Fig. S4 Position of MWCNT UV-Vis spectra components vs wall thickness

Raman spectra

Table S2 Band position in Raman spectra

Sample name	Powder				Layer			
	D [cm^{-1}]	G [cm^{-1}]	D' [cm^{-1}]	2D [cm^{-1}]	D [cm^{-1}]	G [cm^{-1}]	D' [cm^{-1}]	2D [cm^{-1}]
MCWNT 9	1326.60	1577.05	1609.27	2646.09	1332.46	1584.02	1617.26	2658.14
MCWNT 11	1328.74	1578.55	1610.87	2649.22	1332.74	1584.53	1617.10	2658.26
MCWNT15+	1326.74	1575.58	1608.98	2649.92	1333.02	1583.76	1618.06	2659.69
MCWNT 16	1327.81	1579.16	1610.57	2649.59	1333.27	1586.56	1618.23	2660.13
MCWNT 18	1328.69	1580.24	1610.55	2649.73	1333.15	1585.84	1617.4	2659.31

Table S3 Band parameters of Raman spectra

Sample name	Powder				Layer			
	I_D/I_G	A_D/A_G	$I_{D'}/I_{D'}$	$A_{D'}/A_{D'}$	I_D/I_G	A_D/A_G	$I_{D'}/I_{D'}$	$A_{D'}/A_{D'}$
MCWNT 9	1.89150	2.46849	2.75314	7.03301	1.85234	2.26223	2.64812	7.00032
MCWNT 11	1.90435	2.23033	2.99555	6.06936	2.17196	2.47627	3.06349	7.9948
MCWNT15+	1.86665	2.32679	3.42811	6.47527	1.78059	2.08908	2.72409	6.25706
MCWNT 16	2.49393	3.00657	3.64035	8.02595	2.41209	2.44505	3.92132	9.42588
MCWNT 18	2.60067	3.25619	3.80761	8.97479	2.46953	2.80089	3.61020	8.9986

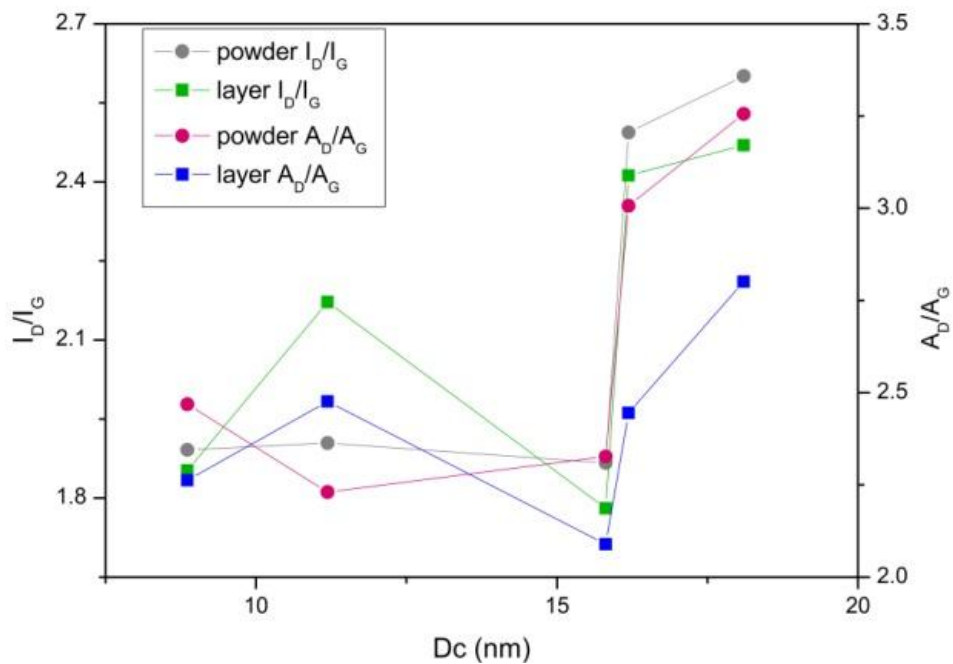


Fig. S5 Intensities (I_D/I_G) and integral intensities (A_D/A_G) ratio of band D and G measured from the powder (circle) and film (square)

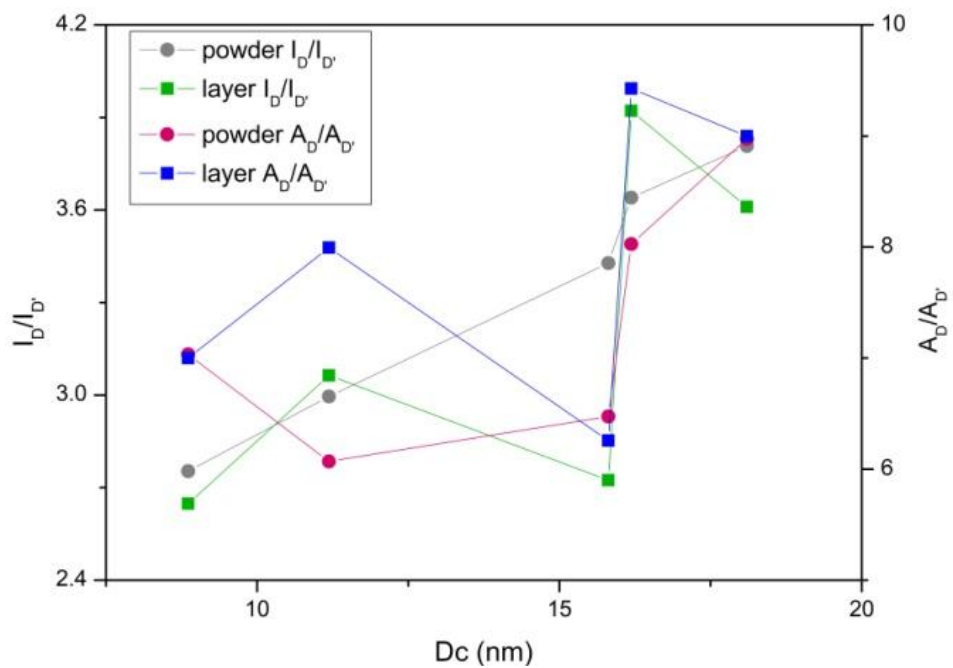


Fig. S6 Intensities ($I_D/I_{D'}$) and integral intensities ($A_D/A_{D'}$) ratio of band D and D' measured from the powder (circle) and film (square)

Surface resistivity anisotropy

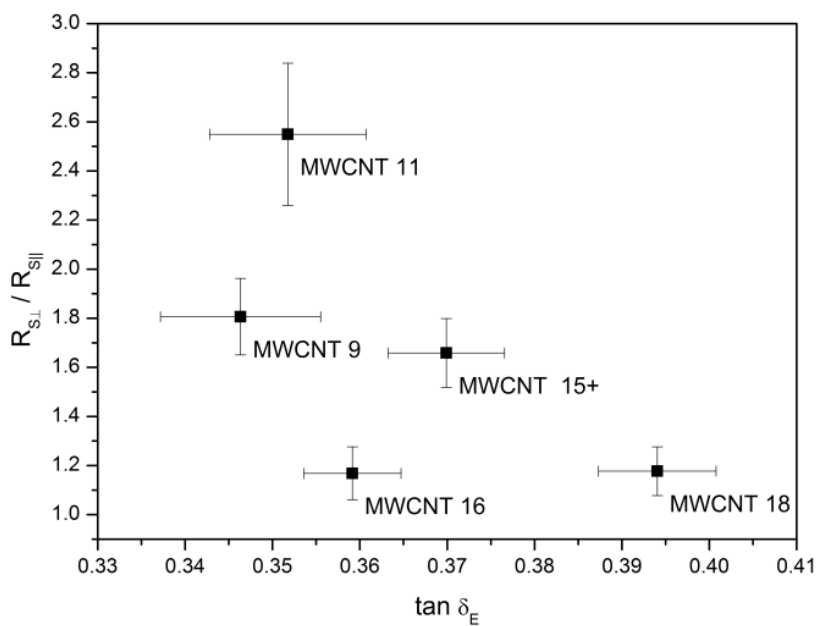
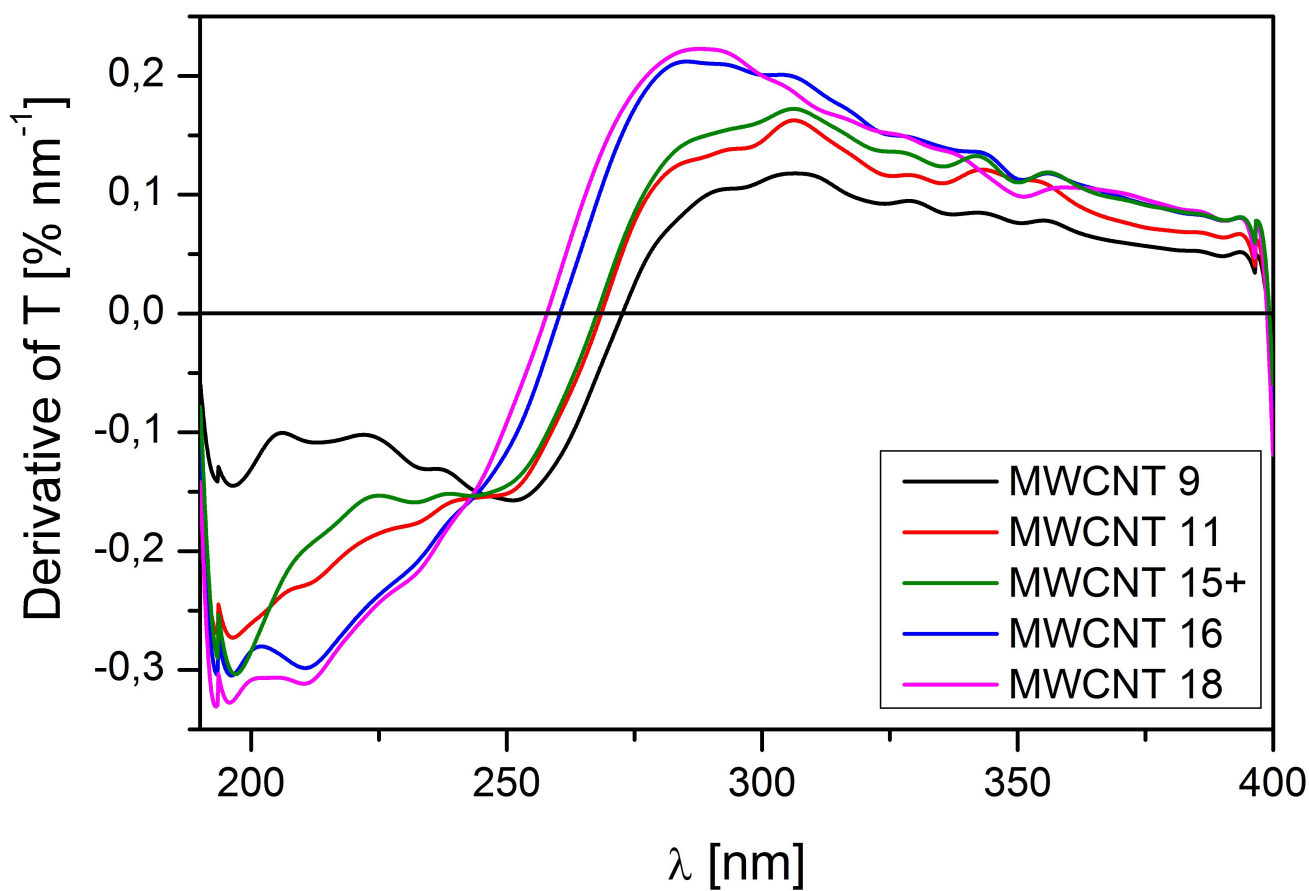
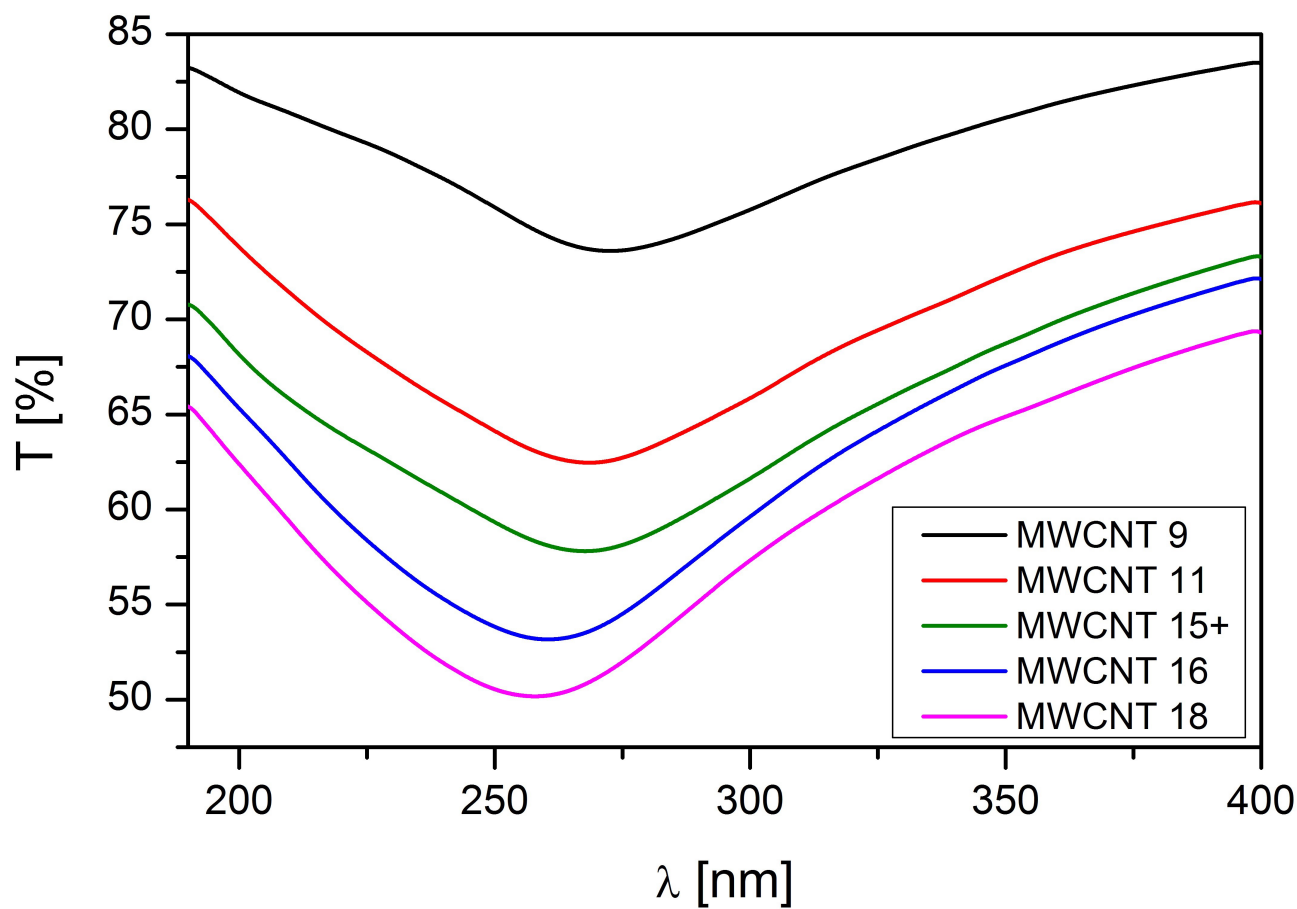
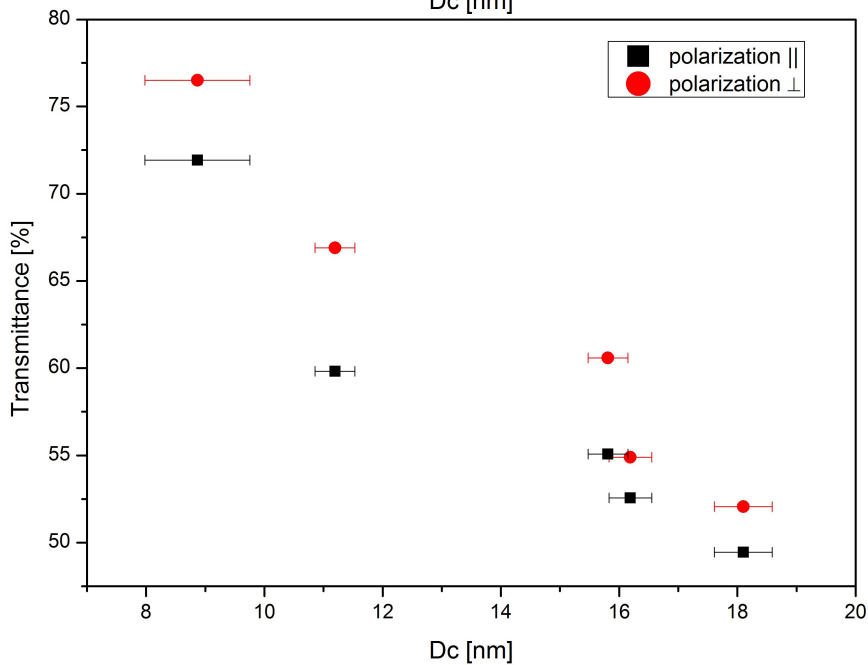
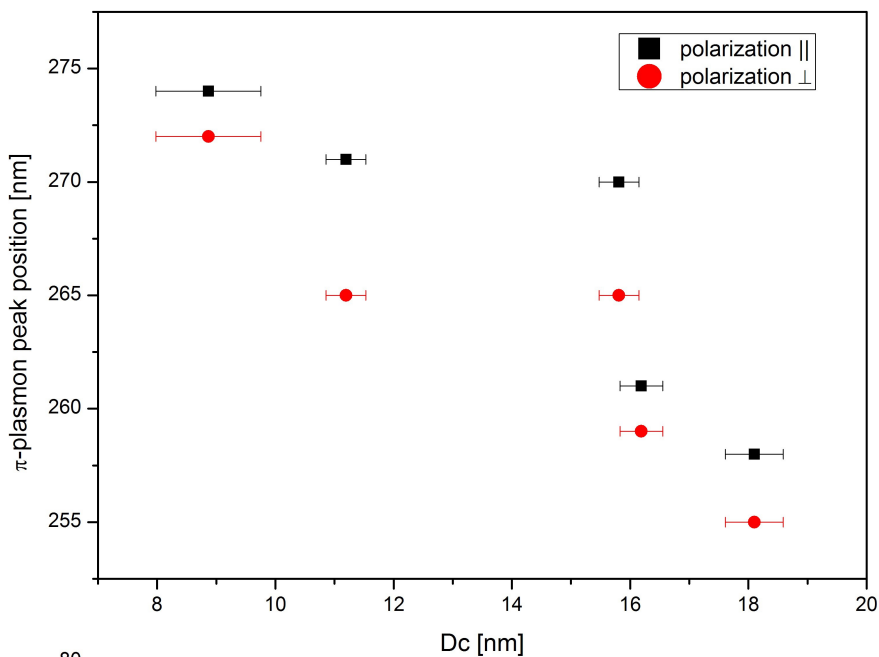
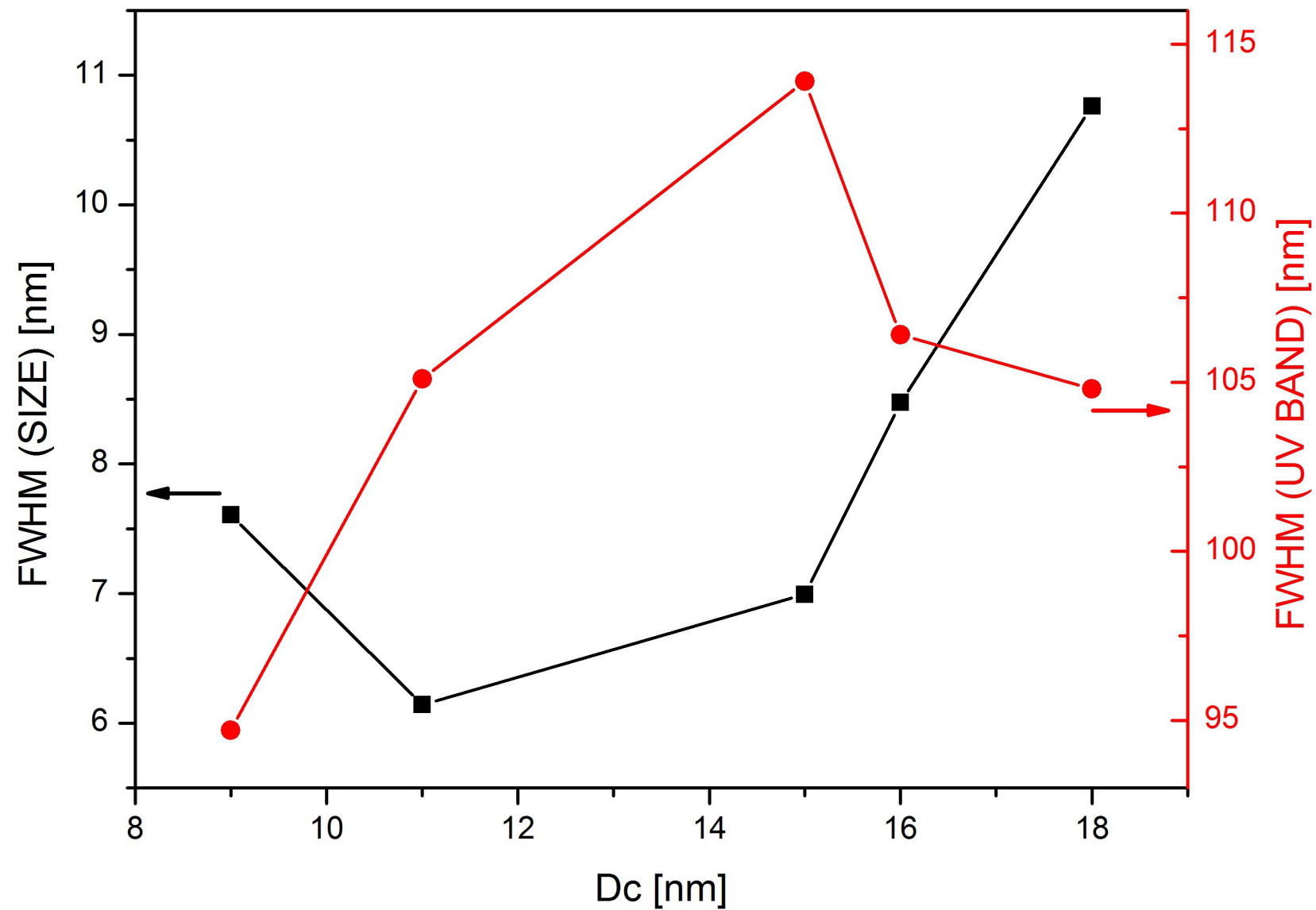
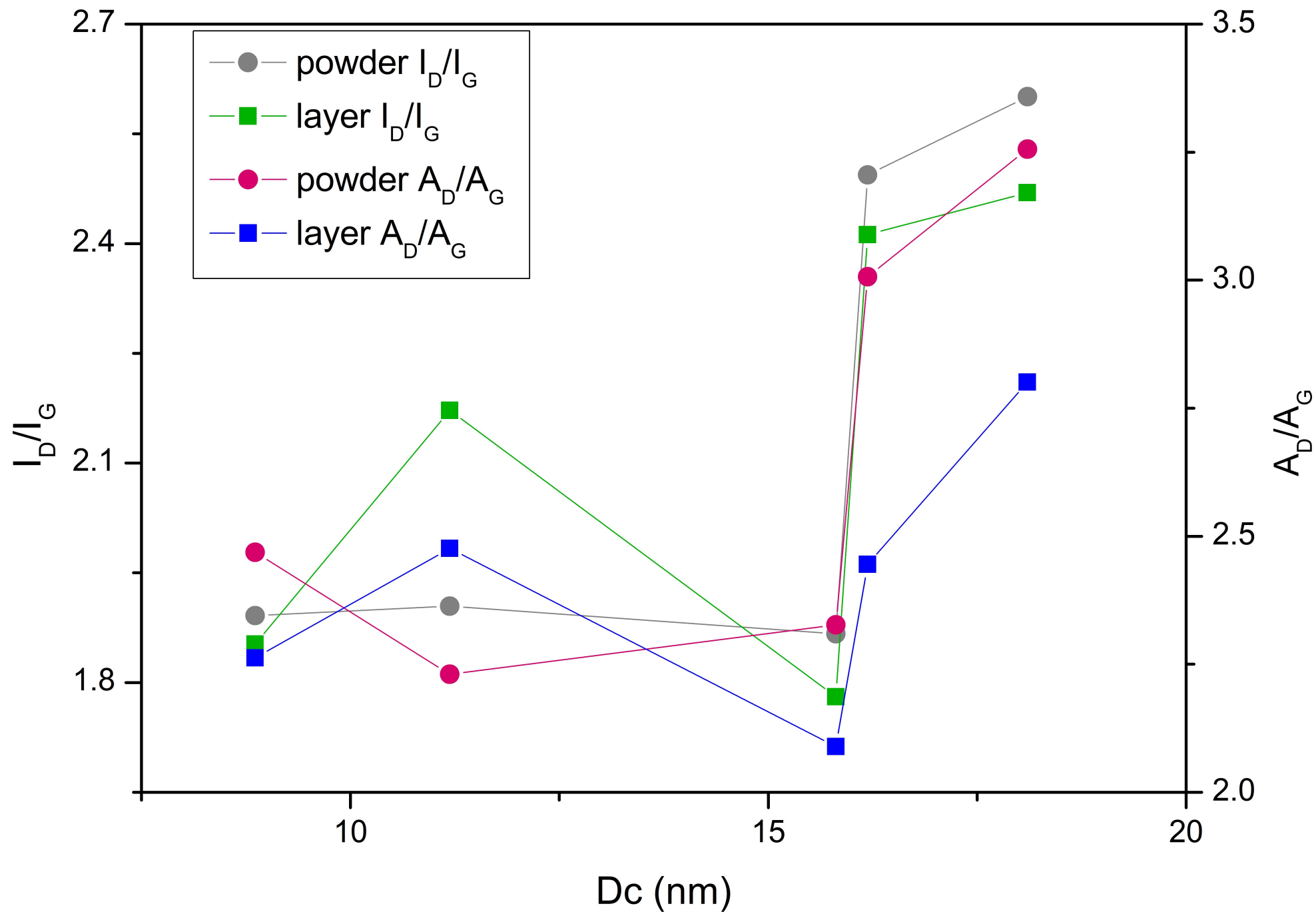


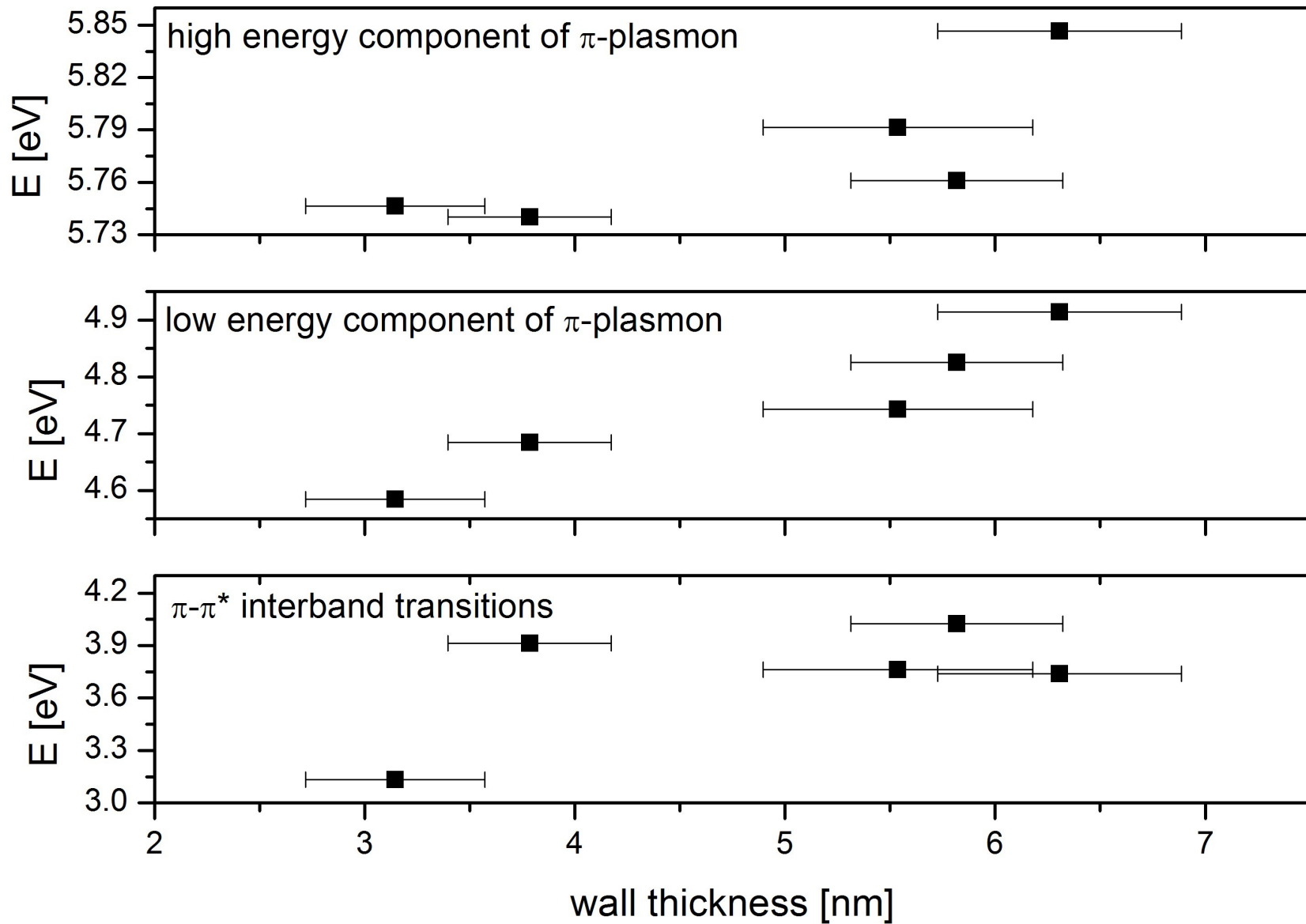
Fig. S7 Dependence of the anisotropy parameter ($R_{s\perp} / R_{s\parallel}$) in the compression loss tangent ($\tan \delta_E$)

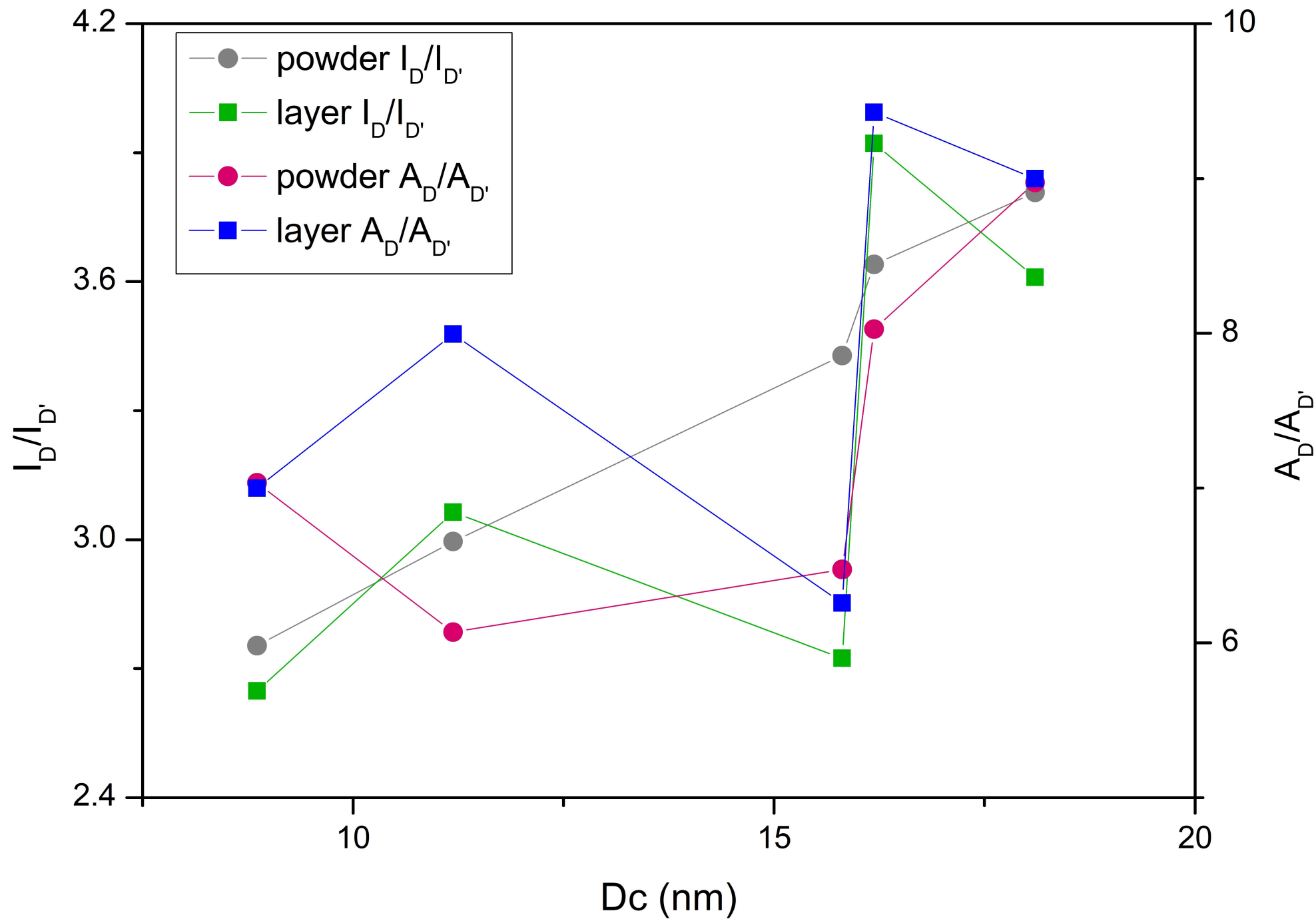


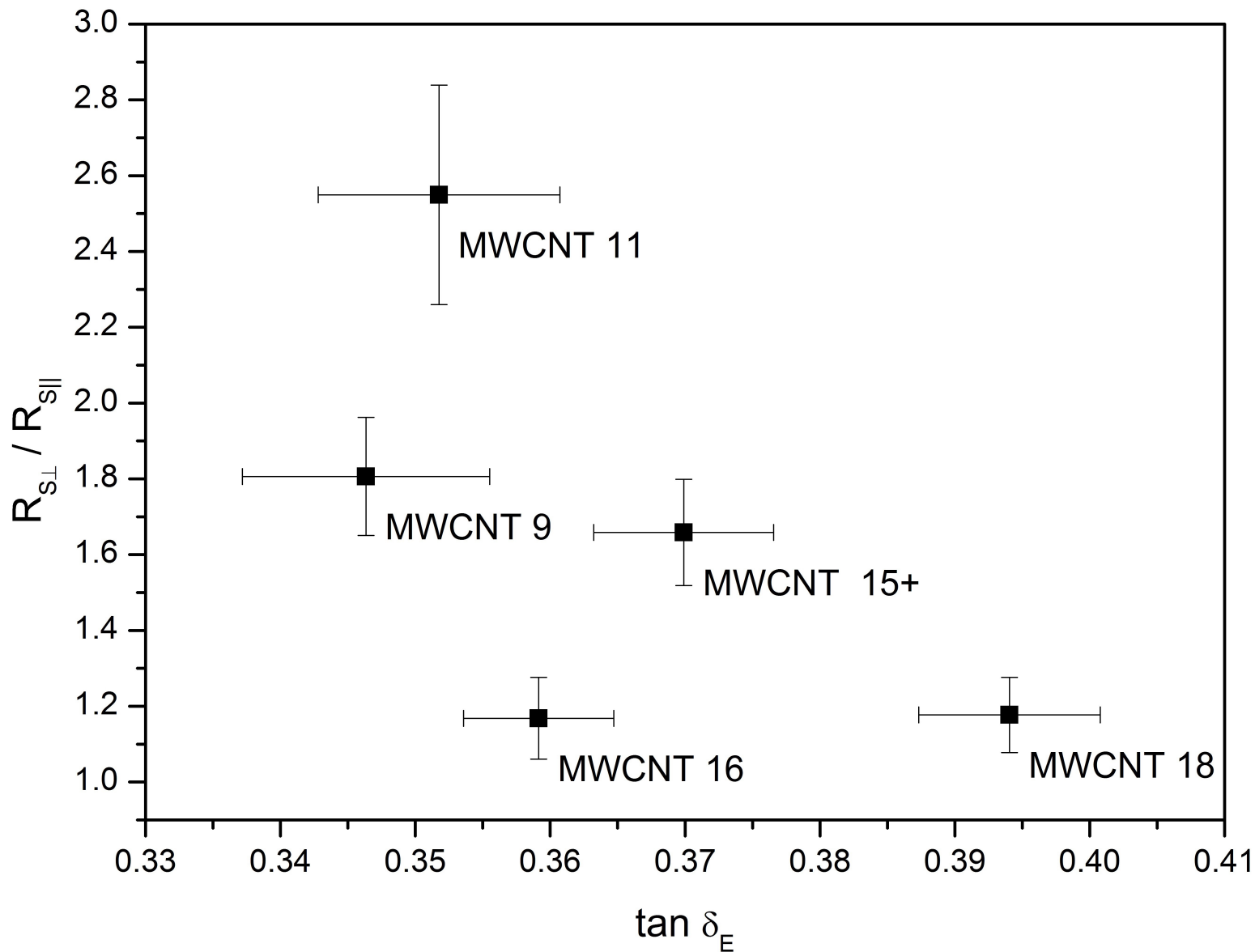






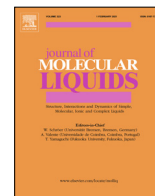






Przedruk publikacji [Rytel JoML 2022]

K. Rytel, K. Kędzierski, B. Barszcz, B. Biadasz, Ł. Majchrzycki, D. Wróbel,
*The influence of zinc phthalocyanine on the formation and properties of
multiwalled carbon nanotubes thin films on the air-solid and air-water interface,*
J. Mol. Liq. 350 (2022) 118548-1–118548-8. doi:10.1016/j.molliq.2022.118548
(MEiN 100, IF 6,165)



The influence of zinc phthalocyanine on the formation and properties of multiwalled carbon nanotubes thin films on the air–solid and air–water interface

K. Rytel^{a,*}, K. Kędzierski^a, B. Barszcz^b, A. Biadasz^a, Ł. Majchrzycki^c, D. Wróbel^a

^a Faculty of Materials Engineering and Technical Physics, Institute of Physics, Poznan University of Technology, Piotrowo 3, 60-965 Poznań, Poland

^b Institute of Molecular Physics, Polish Academy of Sciences, Smoluchowskiego 17, 60-179 Poznań, Poland

^c Centre for Advanced Technology, Adam Mickiewicz University, Uniwersytetu Poznańskiego 10, 61-614 Poznań, Poland

ARTICLE INFO

Article history:

Received 24 September 2021

Revised 20 December 2021

Accepted 14 January 2022

Available online 19 January 2022

Keywords:

Langmuir films

Air–Water Interface

Carbon nanotube

Phthalocyanine

Molecular interactions

Percolation threshold

ABSTRACT

The influence of zinc phthalocyanine (PC) on the formation and properties of multiwalled carbon nanotube (MWCNT) Langmuir films was studied. The mixtures of PC and MWCNT at different concentrations were prepared and used to obtain films on the air–solid and air–water interface. The excess Gibbs energy, excess areas and the area fraction covered by the mixtures components were determined for mixed systems at various surface pressures. For the mass fractions of MWCNT lower than 0.9, the interactions between the mixture components were attractive, while for the MWCNT mass fractions higher than 0.9, they were repulsive. Analysis of the area fractions and fluorescence images revealed three stages of filling the MWCNT films with PC. In the first stage, the PC filled the area between the MWCNT and started to form inclusions in the MWCNT film structure. In the second stage, gradual increase in the PC inclusion size with increasing PC concentration was observed. In the third stage, continuous PC films were formed. These observations were further confirmed by the calculation of electrical percolation threshold.

© 2022 Elsevier B.V. All rights reserved.

1. Introduction

Carbon nanotubes (CNT) have a variety of applications in such fields as: energy storage devices, chemical sensors, field effect transistors and transparent electrodes [1–6]. A precondition for the use of CNT in industrial applications is the possibility to obtain large scale and cheap homogeneous thin films, which is still problematic. Various methods for obtaining thin films have been proposed, including spin-coating, spray-coating, transfer printing and Langmuir methods [7–9]. The advantage of using Langmuir deposition methods is the ability to precisely control the film density and structure [10–14]. The greatest advantage of this method is the possibility of obtaining anisotropic thin films [11,12,15–17]. In addition to the above-mentioned advantages, Langmuir methods allow the study of interactions between components of a given mixture by the Langmuir isotherm analysis [18–22]. The main purpose of these studies is usually to examine and understand the influence of different types of compounds on biological mem-

branes [18–21]. However, this methodology can also be used in the search for materials that prevent formation of aggregates [22].

The surface pressure as a function of the film surface is directly measured in the Langmuir method. This relationship allows the calculation of the energy required to compress the film. The energy required for compression of a mixed film and the energy needed to compress its components are not the same thing. By analysing their mutual relation it is possible to obtain information on both the direction and strength of the interactions between film components [18–22]. The information about interaction strength, is the most important in the search for good dispersants for nanomaterials. This search is most often realized by analysis zeta potentials, surface tensions and stability of the suspension over time [23–25]. Only in the case of zeta potential measurements, the information on the interactions between the components of a mixture can be obtained. However, this method is limited to electrostatic interactions study. Therefore, the presence of ions or a high polarity solvent is necessary.

An alternative to the above mentioned techniques is the theoretical approach. By using molecular dynamics simulations, Xu *et al.* investigated the interactions between CNT and pulmonary surfactant monolayer. They explained how the diameter and length of SWCNT regulate their interactions with the pulmonary

* Corresponding author.

E-mail address: karol.rytel@put.poznan.pl (K. Rytel).

surfactant monolayer [26]. However such a studies are severely limited by computational power, which makes it necessary to reduce the dimensions of the CNT studied (e.g. very short single-walled carbon nanotubes).

The properties of films composed of CNT alone are not sufficient in some cases. Enrichment of CNT films with additional compounds may result in substantial changes of the films properties [27–30]. There are plenty of studies of hybrid materials that consist of CNT and organic dye focuses on the areas such as sensors, fuel cells and photovoltaic [31–33]. None of those studies involve investigations of the Langmuir films containing CNT and organic dye. On the other hand, there are several works on Langmuir films containing CNT and other compounds. By adding polymers to the CNT films the increase in the Langmuir films stability at air–water interface or new photoelectrochemical and gas sensing properties can be achieved [34–37]. Also, introduction of CNT to the lipid Langmuir films has resulted in their enhanced enzymatic and catalytic properties [38–40]. Understanding the interactions between CNT and other materials is essential for further improvement of the aforementioned properties.

In order to use multiwalled carbon nanotube (MWCNT) films obtained via Langmuir techniques as a transparent electrodes, both their transmittance and electrical conductivity must be increased [12,14,16]. The change in transmittance should be achieved by increasing the distance between MWCNT, while maintaining the number of MWCNT contacts as high as possible. Increase in transmittance can be achieved by changing the surface pressure at which the films are transferred onto the solid substrate. However, this changes are still insufficient to solve the aforementioned problems [12,14]. Higher transmittance can be achieved by introducing additional compound into the MWCNT film structure. However, the additional compound should be selected in such a way that produce films with greater electrical anisotropy, which at least partially solves the problem of low electrical conductivity.

The aim of this study was to increase the transmittance of the MWCNT film and to investigate by what margin the resistance of MWCNT/PC films would increase. In addition, we wanted to investigate the separation process of MWCNT and determine what effect the interactions between the mixture components have on this process. We decided to investigate the interactions between MWCNT and PC, using Langmuir isotherms analysis for the films of MWCNT-PC mixtures of different concentrations. Moreover, we investigated the influence of PC on the optical and electrical properties of the MWCNT-PC films. Zinc phthalocyanine (PC) was chosen to act as a MWCNT separator in Langmuir films due to the high transmittance of PC monolayer films [41]. Furthermore, relatively strong fluorescence makes PC a good candidate for a fluorescence marker [42].

2. Materials and methods

2.1. Materials

The mixtures of zinc phthalocyanine (zinc (II) 2,9,16,23-tetra-*tert*-butyl-29H, 31H-phthalocyanine, Sigma-Aldrich) with MWCNT (6–9 nm diameter, Sigma-Aldrich) were studied. PC was dissolved in spectrally pure dichloromethane (DCM) in a concentration of $160.4 \mu\text{g ml}^{-1}$. MWCNT were dispersed in DCM in a concentration of $20 \mu\text{g ml}^{-1}$. The dispersion of MWCNT was carried out by a probe sonicator (Hielscher 400St, 24 kHz) in an ice bath to minimize solvent evaporation. The suspension (200 ml) was sonicated by a 14 mm diameter sonotrode at 60 W power for 20 min.

2.2. Langmuir films preparation

Langmuir films were obtained on a KSV instruments Ltd. 2000 LB system, with a custom made Teflon trough of 750 cm^2 area

($15 \text{ cm} \times 50 \text{ cm}$), under laminar flow at a stabilized temperature of $20 \pm 0.5 \text{ }^\circ\text{C}$. In our experiments, the subphase was deionized water (electrical resistivity $18.2 \text{ M}\Omega \text{ cm}$) obtained with an ultra-pure water purification system (Millipore Corp.). To obtain a Langmuir film, the suspension was carefully spread onto the subphase and before compression we waited for 30 min for DCM evaporation. Platinum Wilhelmy plate was placed parallel to the barriers for measurement of the surface pressure. The table summarizing the operating conditions has been added to the [supplementary information](#) (Table S1)

Determination of molar concentration of the MWCNT requires extensive work and its value depends on the material homogeneity in terms of diameter and length. Therefore, the value obtained is affected by a large error. Instead of generally accepted parameters, such as area per molecule or molar fraction, the area per mass unit or mass fraction (MF) was used. The compression isotherms of films were measured for different proportions of PC and MWCNT, ranging from pure MWCNT to pure PC. The concentration, mass fractions and the amount of used materials are specified in [supplementary information](#) (Table S2)

2.3. Films deposition

The layers were transferred simultaneously onto quartz substrate ($7.6 \text{ cm} \times 2.6 \text{ cm}$) and polyvinyl chloride (PCV) foil ($2 \text{ cm} \times 2 \text{ cm}$) by horizontal transfer. The quartz substrate was placed in such a way that the long axis was parallel to the barrier. The transfer process was carried out by removal of the substrate from the subphase, in the same way as in our previous studies [12,14]. The substrate was removed at a constant speed of 1 mm min^{-1} . Before the transfer, the floating films were relaxed at a specified surface (see [supplementary information](#) Table S2) pressure for 50 min to obtain a uniform layer.

2.4. Films investigation

After deposition, the homogeneity of LB films was checked via confocal laser scanning microscope (Zeiss LSM710) in the material and fluorescent modes. In the material mode, a HeNe laser operating at 543 nm wavelength was used. In the fluorescence mode, an HeNe laser operating at 633 nm was used and fluorescence was observed in the range 643–799 nm.

The electric resistance measurements were performed using a standard two-probe method by a Keithley 2400-LV source meter. The contacts were made of silver wire (diameter 0.25 mm) and attached to the film using a silver paint. The electrodes were placed in such a way to ensure the perpendicular or parallel current flow, with respect to the position of the barrier at the Langmuir trough, as in our previous work [14]. For each film the measurements were made at 8 different locations for each current flow direction and the measurement uncertainty was calculated as the standard deviation. The area of the MWCNT film between electrodes was measured using an Imager Z2m Zeiss microscope. The SEM images were recorded by means of the HeliosNanoLab 660 (FEI) scanning electron microscope operating at 1 kV.

3. Results and discussion

3.1. Films thermodynamics

Fig. 1 presents the dependence of surface pressure (Π) on the surface area per unit mass (A) of all mixtures components. For materials of low densities, 2D gas phase was identified for all studied films and the surface pressure was negligible. With increasing compression, the value of Π smoothly grows and then collapses at

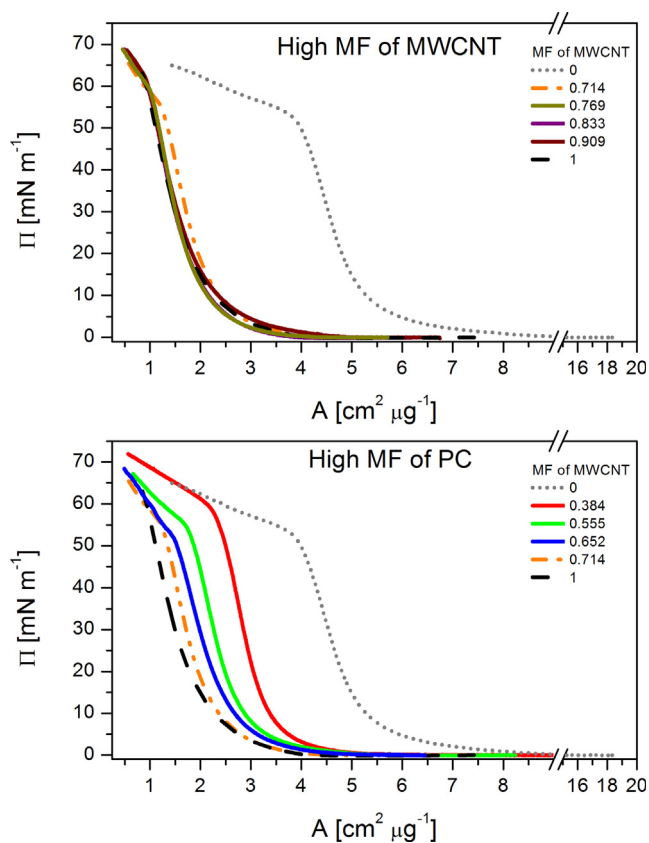


Fig. 1. Dependence of surface pressure on the surface area per 1 μg of used materials obtained for PC and MWCNT mixtures at high mass fraction of MWCNT (top) and high mass fraction of PC (bottom).

a specific surface pressure value (see [Supplementary materials Fig. S2](#)). Unfortunately, the collapse point and the shape of the isotherm for pure MWCNT depended on the quantity of the suspension used (see [Supplementary materials Fig. S3](#)). However, for the amount of suspension used in the range from 5 ml to 6 ml almost identical isotherms were observed. Thus, the volume of the MWCNT suspension used was in range from 5 ml to 6 ml. For pure PC films, the obtained isotherms were similar to those reported by Matsuura *et al.* and the differences visible for low surface pressures were related to the film compression rate[43]. Moreover, the limiting area (see [Fig. S4](#)), obtained by the extrapolation of the linear region to zero surface pressure just before collapse was almost identical to that shown by Matsuura *et al.* This indicates that the plane of the molecular structure of PC was tilted relative to the subphase surface. For the mixtures with high contents of PC, a gradual increase in surface density was observed, while for the mixtures with high contents of MWCNTs, minor changes in the isotherm shape were observed.

Compressibility modulus (β) vs surface pressure calculated for each MF of MWCNT is shown in [Fig. 2](#). The compressibility module is a measure of the film stiffness and can be calculated from the following equation[21]:

$$\beta = -A \frac{\partial \Pi}{\partial A}$$

where A is the area per mass unit of the film and Π is the surface pressure. At the surface pressure of 30 mN m^{-1} , the PC film reaches a maximal value of compressibility modulus and the area per molecule of 0.603 nm^2 , which corresponds to the geometrical cross-section of PC molecule[43]. For higher surface pressures,

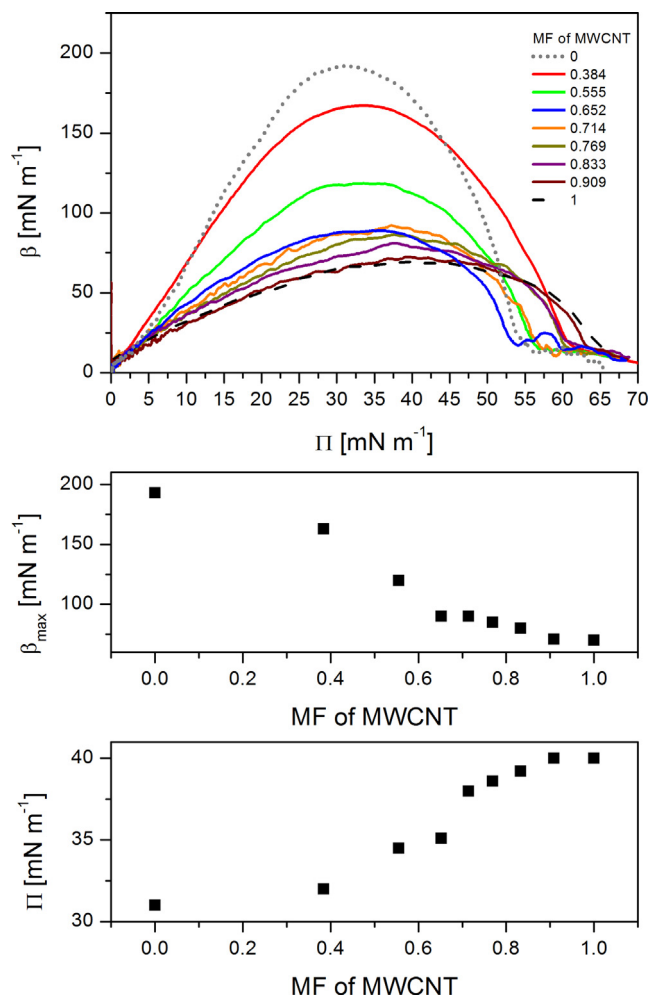


Fig. 2. Compressibility modulus (β) vs surface pressure (Π) calculated for each MF of MWCNT (top); maximal value of compressibility modulus vs mass fraction (MF) of MWCNT (middle); maximal value of surface pressure at compressibility modulus maximum vs mass fraction of MWCNT (bottom).

the processes such as PC reorientation, tilt angle change or multi-layer formation may occur, causing a decrease in the compressibility modulus. For MWCNT or graphene films at surface pressure above 40 mN m^{-1} the multilayer formation (mainly near barriers) may occur, which is visible to the naked eye. We decided to transfer the films for further studies at a pressure corresponding to the maximum compressibility of the mixture, in order to obtain the best homogeneity of the films, while maintaining the previously mentioned film parameters. The maximal compressibility module obtained for MWCNT films is significantly lower than that for PC films (70 mN m^{-1} vs 193 mN m^{-1} , respectively) and a gradual increase in this value with increasing PC content was observed. The reason for this increase is that PC fills the spaces between MWCNT causing gradual strengthening of the film's structure. An analogous dependence is observed for the surface pressure at the maximum of the compressibility modulus.

3.2. Excess Gibbs free energy

Analysis of the interactions between the components making the film at the air–water interface can be made in terms of the excess Gibbs free energy of mixing and its value was calculated from the following expression[19,20,22,44]:

$$\Delta G = A_{12} \int_{\Pi_0}^{\Pi} d\Pi_{12} - \left(x_1 A_1 \int_{\Pi_0}^{\Pi} d\Pi_1 + x_2 A_2 \int_{\Pi_0}^{\Pi} d\Pi_2 \right)$$

where: A_{12} – is the experimental value of area per mass unit in a bicomponent film, A_1 and A_2 are the area per mass unit of the first and second component film, respectively, while x_1 and x_2 are the mass fractions of the components. It is worth mentioning that the generally accepted unit of excess Gibbs free energy is joules per molecule. However, it is not possible to use it because of the unknown molar mass of the MWCNT used. For this reason, ΔG was calculated per unit mass of the mixture components. The values of $\Delta G > 0$ indicate the repulsive forces between the components of the mixture and the higher the value of ΔG , the stronger the repulsive forces between them. If the values of ΔG are negative, the attractive forces instead of repulsive ones appear and the smaller the value of ΔG , the stronger the attractive forces between the components [19,20,22,44].

3.3. Excess areas

Usually, the repulsive or attractive interaction between components of the films at the air–water interface cause a change in the excess area ΔA defined as [22,44]:

$$\Delta A = A_{12} - (x_1 A_1 + x_2 A_2)$$

If the interactions between the film components are repulsive, ΔA should take a positive value. Moreover, the stronger the interactions, the higher should be the value of the excess area. As shown in Fig. 3A and 3B, the above mentioned relations are not obeyed for the films studied. Despite the increase in strength of the interactions between MWCNT and PC with increasing Π , the excess area decreases, due to the fact that at lower compression states MWCNT occupy a smaller portion of the total area leaving more space available to PC.

3.4. Area fractions

From the Π -A isotherms, the area fraction occupied by each component at any given compression state can be calculated for any mixture composition as:

$$AF = \frac{A_1 * FF}{A_{exp}}$$

where A_1 is the area per unit mass of a selected mixture component (MF of MWCNT equal to 1 or 0), FF is the fill factor corresponding to the film transferred at the surface area A_1 and A_{exp} is the experimental area per unit mass of the same component for which we calculate AF. The values of A_1 and A_{exp} were calculated on the basis of the isotherms obtained during the layer transfer process (after compression and relaxation time). The value of FF of MWCNT and its measurement uncertainty of 0.426 ± 0.021 were determined from SEM and confocal microscopy images (mean value and standard deviation for twelve images). The FF for PC was assumed as 1 on the basis of the fluorescence microscopy images. It is worth emphasizing that the AF values of each component calculated in this way can add up to values lower or higher than 1. The values higher than 1 are observed if both mixtures components are stack on each other. On the other hand, the values lower than 1 indicate that the film has some areas not covered by either of the components (see Fig. 3C).

3.5. Interaction between mixtures components

In order to explain the interaction between MWCNT and PC, three regions should be distinguished, as shown in Fig. 3. The first region corresponds to a gradual filling of the spaces between the

MWCNT (hereafter referred to as pores; see Fig. 3D SEM) with PC observed for MF of MWCNT in the range from 1 to 0.769. The information on pore filling can be obtained from the linear relationship between the AF of MWCNT + PC and ΔA with respect to MF of MWCNT (see in Fig. 3C and 3B).

For low concentrations of PC, the surface pressure inside the pores is lower than that measured by the Wilhelmy plate. The dye inside the pore is oriented horizontally to the subphase which makes the *tert*-butyl group of PC to interact with MWCNT. Partially filled pores require more energy to contract than empty pores, which can be interpreted as repulsive interactions. Thus positive ΔG values and homogeneous fluorescence images are observed (see Fig. 3D).

As the pore filling increases, the surface pressure inside the pores tends to the measured value. This leads to a change in the orientation of PC relative to the subphase. Therefore, for higher PC concentrations, the interaction between PC macrocycle and MWCNT is observed. Thus, the transition from positive to negative ΔG is observed. This is consistent with earlier theoretical work [45]. Moreover, due to the presence of attractive interactions, PC inclusions (clusters) start forming (bright red spots in the fluorescence images; see Fig. 3E). Furthermore, formation of PC inclusions suggest the presence of attractive PC-PC interaction near MWCNT.

In the third region (MF of MWCNT below 0.652), the PC molecules form continuous films. Therefore, the percolation threshold should be located near the local maximum of ΔG . Moreover, in this region PC is the medium responsible for the surface pressure transmission. The value of ΔG in this region decreases as the concentration of PC increases, which means a strengthening of the attractive interaction. It was caused by the separation of individual MWCNT which can be seen in SEM images (Fig. 3G). Thus, the number of PC molecules that may interact with individual MWCNT (directly or indirectly) increases.

3.6. Electrical measurements and percolation threshold

Fig. 4 presents the surface resistance measured in parallel and perpendicular direction vs the mass fraction of the used MWCNT. For all samples, linear current–voltage characteristics were observed in the measured current range (from –1 mA to 1 mA). The ratios between resistance measured in perpendicular to parallel direction were in range from 3 to 4. This anisotropy was caused by the relative motion between the MWCNT and the subphase during the compression cycle. However this effect is reduced by the transverse viscoelastic deformations during compression cycle, causing bending of the CNT in the arcs and consequently reducing the observed anisotropy. The electrical anisotropy of MWCNT film was described in more detail in our previous work [12,14]. The growth of the surface resistance was of exponential character for both directions and an almost 4 orders of magnitude increase in the surface resistance was observed. Resistance of the layers with less than 0.65 MF of MWCNT was too high to measure. The reason for this is that the amount of MWCNT per unit of area decreases, limiting the number of conducting paths. This relationship can be analyzed using the percolation theory, according to which, the changes in the surface resistance (R) can be expressed as [46]:

$$R = R_0(p - p_c)^{-t}$$

where R_0 is a constant, t is the percolation exponent, p is the amount of conducting material and p_c is the critical amount of conducting material. The relationship between the surface resistivity and $p - p_c$ can be expressed as a straight line in the log–log scale. In order to determine the value of p_c , a linear fit was performed for various p_c values and the value for which the best fit was obtained was chosen. The values of t were calculated as the slopes

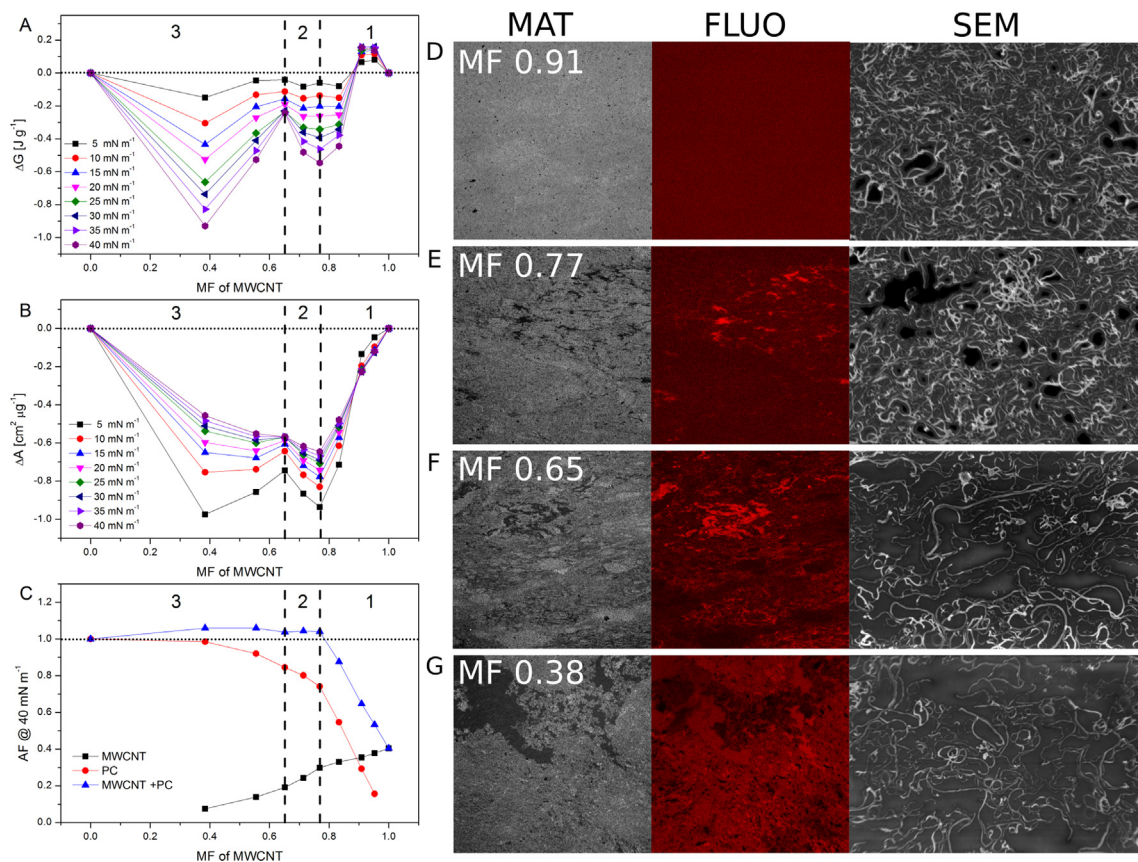


Fig. 3. Excess Gibbs free energy (ΔG) vs mass fraction (MF) of MWCNT for various surface pressures (A); Excess area vs mass fraction (MF) of MWCNT for various surface pressure (B); Area fraction occupied by MWCNT, PC and MWCNT + PC at surface pressure of 40 mN m^{-1} vs mass fraction (MF) of MWCNT (C); all presented values were calculated based on the data from Fig. 2; LSM images ($425 \mu\text{m} \times 425 \mu\text{m}$) in the material and fluorescent mode and SEM images ($2.6 \mu\text{m} \times 4 \mu\text{m}$) obtained for the films with mass fraction of MWCNT of 0.91 (D), 0.77 (E), 0.65 (F), 0.38(G).

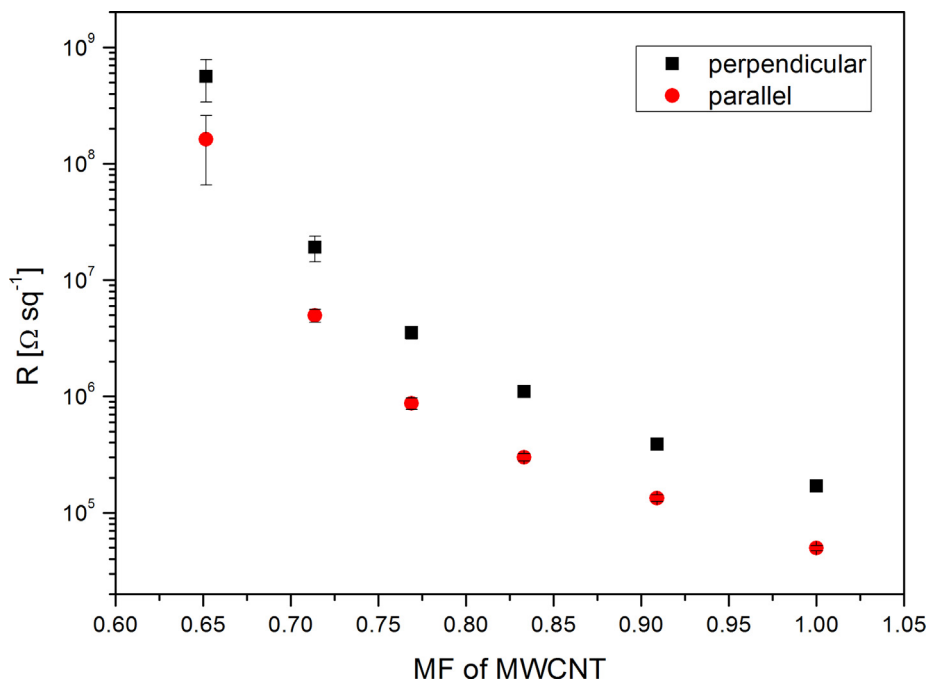


Fig. 4. Surface resistance (R) vs. mass fraction of MWCNT measured with respect to the barriers position.

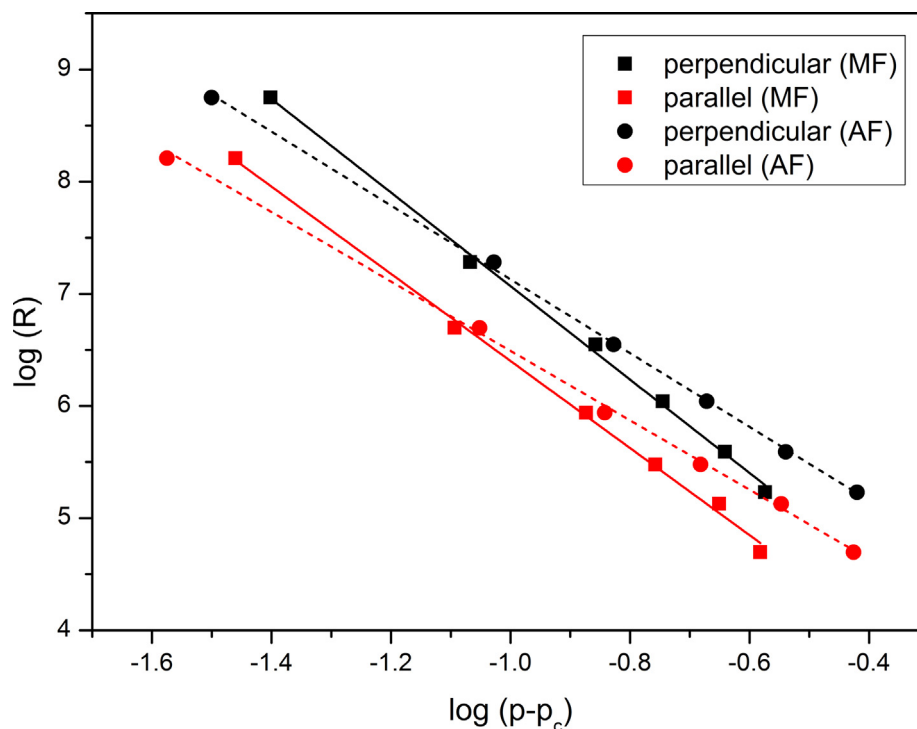


Fig. 5. The relationship between surface resistivity and $p-p_c$ for p and p_c expressed as mass fraction and area fraction.

Table 1
Fitting parameters obtained for the amount of MWCNT expressed as mass fraction and area fraction.

	Mass Fraction			
	p_c	t	R_0 [k Ω]	Fitting Coefficient
Perpendicular	0.620	3.29	6.913	0.99921
Parallel	0.625	3.06	2.484	0.99848
	Surface density			
	p_c [$\mu\text{g cm}^{-2}$]	t	R_0 [k Ω]	Fitting Coefficient
Perpendicular	0.305	4.21	11.78	0.99770
Parallel	0.325	3.67	4.696	0.99690
	Area Fraction			
	p_c	t	R_0 [k Ω]	Fitting Coefficient
Perpendicular	0.165	4.17	0.799	0.99767
Parallel	0.16	3.88	0.329	0.99692

of the lines in Fig. 5. This procedure was performed for the amount of MWCNT (conducting material) expressed as the area fraction and mass fraction and the fitting results are summarized in Table 1. The small difference between the two results is due to the fact that some of the MWCNT overlap one another. The area fractions of PC and MWCNT films were calculated from the isotherms obtained during the transfer process and the data are presented in supplementary materials (Fig. S5).

For single percolation systems, the critical component t is related to the sample dimensionality. The universal values of critical exponent t are 1.33 and 2, for two and three dimensional systems, respectively. However, its higher values have been often reported in literature[46]. Most common explanations of non-universal critical exponent are non-direct electrical contacts between conductive material, electric charge tunneling and non-uniform dispersion of conductive filler[46–48]. All of the above factors may be present in the examined films, causing an increase in the parameter t to a value above 3, instead of the expected value of 1.33.

The value of p_c (about 0.62) expressed as a mass fraction seems to be enormous. However, the thickness of pure PC film is almost

five times smaller than the diameter of MWCNT (1.55 nm and 7.5 nm for PC and MWCNT, respectively)[43]. Moreover, in the studied system there are surfaces which are not occupied either by MWCNT or PC. Taking these two effects into account, the p_c value expressed as a mass fraction will be significantly reduced. Despite these problems, in some cases there are practical reasons for calculating this value in mass fraction units, which facilitates the practical reproduction of the experiment. For thin films, p_c expressed as a surface density of the conducting material is often used. This permits making the p_c value independent of the density of the insulating material and the area not covered by any material. Although, if the conductive material overlaps one another the p_c value will be inflated. This problem can be eliminated if p_c is expressed as the area fraction.

Due to the previously mentioned problems, comparison of the obtained percolation threshold with the results reported by other authors is not a trivial task. The percolation threshold value of 0.62 (MF) obtained in this work is by a few orders of magnitude higher than that obtained for the latex/SWCNT composite of 0.0012 (MF). However, we achieved a slightly higher film transmittance of 95% vs. 93% (see supplementary materials Fig. S6 and

Fig. S7) and significantly higher electrical conductivity of $8 \cdot 10^{-3} \text{ S cm}^{-1}$ (assuming films thickness of 7.5 nm) vs $10^{-5} \text{ S cm}^{-1}$, which is significantly better for films applications in transparent electronics [49]. On the other hand, Lee *et al.* have provided empirical equation for determination of p_c expressed in terms of surface density which at the rigid random-coil limit is depended on the MWCNT density, diameter and the static bending persistence length [50]. According to this equation percolation threshold of $0.315 \mu\text{g cm}^{-2}$ should be obtained for MWCNT density of 1.4 g cm^{-3} , diameter of 7.5 nm and static bending persistence length of 25 nm.

4. Conclusions

In this paper we report on the effects of the presence of zinc phthalocyanine on the formation and properties of multiwalled carbon nanotubes thin films on the air–solid and air–water interfaces. Based on the relation of the surface pressure to the area occupied by unit mass of the mixture components the strength and direction of the interactions between MWCNT and PC were determined. For the mass fraction of MWCNT lower than 0.9, the interactions between the mixture components were attractive, whereas for the mass fractions higher than 0.9 they were repulsive.

The repulsive interactions appeared as a result of the interactions of *tert*-butyl groups of PC with MWCNT. On the other hand, the attractive interactions were a consequence of the interaction of the PC macrocycle with MWCNT. A change in the direction of the interactions between MWCNT and PC resulted in the formation of PC inclusions (clusters). With increasing PC concentration the size of the inclusions increased until a continuous PC film was formed followed by the separation of individual nanotubes.

Electrical measurements of the MWCNT/PC films revealed the exponential growth of the surface resistance with increasing PC concentration for both current directions and an increase in surface resistance by almost 4 orders of magnitude was observed. Moreover, the increase in the surface resistance was accompanied by the increase in its relative error (from about 5% to 40%). Thus, the process of MWCNT separation was not uniform. The lowest determined percolation thresholds were 0.620, 0.305, 0.16, expressed in terms of mass fraction, surface density the fraction of area covered with MWCNT

On the basis of the data obtained, we believe that the percolation thresholds can be significantly reduced for a compound for which strong attractive interactions are observed at its low concentrations. Moreover, with increasing concentration of such a compound increasingly stronger repulsive interactions would be observed. The proposed research methodology is particularly relevant in the field of finding optimal compounds to facilitate the dispersion of nanomaterials.

CRedit authorship contribution statement

K. Rytel: Conceptualization, Investigation, Formal analysis, Methodology, Visualization, Data curation, Writing – original draft, Writing – review & editing, Supervision, Project administration, Funding acquisition. **K. Kędziński:** Conceptualization, Investigation, Formal analysis, Methodology, Visualization. **B. Barszcz:** Conceptualization, Validation, Formal analysis, Writing – original draft, Writing – review & editing. **B. Biadasz:** Conceptualization, Validation, Formal analysis, Methodology. **Ł. Majchrzycki:** Investigation, Validation, Formal analysis. **D. Wróbel:** Conceptualization, Formal analysis, Validation, Supervision.

Declaration of Competing Interest

The authors declare that they have no known competing financial interests or personal relationships that could have appeared to influence the work reported in this paper.

Acknowledgements

The author would like to thank Dr Małgorzata Widelicka for her helpful discussion. The work is the result of the research project financed by the National Science Centre of Poland (No 2016/21/N/ST8/03557). K. K., A. B. and D. W. acknowledge the support of the Ministry of Science and Higher Education of Poland (No 0512/SBAD/2120).

Appendix A. Supplementary data

Supplementary data to this article can be found online at <https://doi.org/10.1016/j.molliq.2022.118548>.

References

- [1] L. Sun, X. Wang, Y. Wang, Q. Zhang, Roles of carbon nanotubes in novel energy storage devices, *Carbon N. Y.* 122 (2017) 462–474, <https://doi.org/10.1016/j.carbon.2017.07.006>.
- [2] K. Rytel, D. Waszak, K. Kędziński, D. Wróbel, Novel method of current collector coating by multiwalled carbon nanotube Langmuir layer for enhanced power performance of LiMn2O4 electrode of Li-ion batteries, *Electrochim. Acta.* 222 (2016) 921–925, <https://doi.org/10.1016/j.electacta.2016.11.058>.
- [3] V. Schroeder, S. Savagatrup, M. He, S. Lin, T.M. Swager, Carbon nanotube chemical sensors, *Chem. Rev.* 119 (1) (2019) 599–663, <https://doi.org/10.1021/acs.chemrev.8b00340>.
- [4] P. Prakash, K. Mohana Sundaram, M. Anto Bennet, A review on carbon nanotube field effect transistors (CNTFETs) for ultra-low power applications, *Renew. Sustain. Energy Rev.* 89 (2018) 194–203, <https://doi.org/10.1016/j.rser.2018.03.021>.
- [5] K.T. Lee, D.H. Park, H.W. Baac, S. Han, Graphene- and carbon-nanotube-based transparent electrodes for semitransparent solar cells, *Materials* 11 (2018) 1503–1523, <https://doi.org/10.3390/ma11091503>.
- [6] D.S. Hecht, L. Hu, G. Irvin, Emerging transparent electrodes based on thin films of carbon nanotubes, graphene, and metallic nanostructures, *Adv. Mater.* 23 (13) (2011) 1482–1513, <https://doi.org/10.1002/adma.201003188>.
- [7] D. Janas, K.K. Koziol, A review of production methods of carbon nanotube and graphene thin films for electrothermal applications, *Nanoscale* 6 (2014) 3037–3045, <https://doi.org/10.1039/c3nr05636h>.
- [8] V.T. Dang, D.D. Nguyen, T.T. Cao, P.H. Le, D.L. Tran, N.M. Phan, V.C. Nguyen, Recent trends in preparation and application of carbon nanotube-graphene hybrid thin films, *Adv. Nat. Sci. Nanosci. Nanotechnol.* 7 (3) (2016) 033002, <https://doi.org/10.1088/2043-6262/7/3/033002>.
- [9] K. Rytel, M. Widelicka, D. Łukawski, F. Lisiecki, K. Kędziński, D. Wróbel, Ultrasonication-induced sp^3 hybridization defects in Langmuir-Schaefer layers of turbostratic graphene, *Phys. Chem. Chem. Phys.* 20 (18) (2018) 12777–12784.
- [10] K. Kędziński, B. Barszcz, A. Biadasz, M. Matczak, D. Wróbel, Preparation and studies of transparent conductive monolayers of multiwall carbon nanotubes on quartz and flexible polymer with the use of modified Langmuir technique, *Prog. Org. Coatings* 86 (2015) 86–95, <https://doi.org/10.1016/j.porgcoat.2015.04.017>.
- [11] M.K. Massey, C. Pearson, D.A. Zeze, B.G. Mendis, M.C. Petty, The electrical and optical properties of oriented Langmuir-Blodgett films of single-walled carbon nanotubes, *Carbon N. Y.* 49 (7) (2011) 2424–2430, <https://doi.org/10.1016/j.carbon.2011.02.009>.
- [12] K. Rytel, K. Kędziński, B. Barszcz, M. Widelicka, A. Stachowiak, A. Biadasz, Ł. Majchrzycki, E. Coy, D. Wróbel, The influence of diameter of multiwalled carbon nanotubes on mechanical, optical and electrical properties of Langmuir-Schaefer films, *Phys. Chem. Chem. Phys.* 22 (39) (2020) 22380–22389.
- [13] Q. Zheng, L. Shi, P.-C. Ma, Q. Xue, J. Li, Z. Tang, J. Yang, Structure control of ultra-large graphene oxide sheets by the Langmuir-Blodgett method, *RSC Adv.* 3 (14) (2013) 4680, <https://doi.org/10.1039/c3ra22367a>.
- [14] K. Kędziński, K. Rytel, Ł. Majchrzycki, D. Wróbel, Conductive and transparent films of oriented multi-walled carbon nanotubes by Langmuir-Schaefer method, *Thin Solid Films* 589 (2015) 701–706, <https://doi.org/10.1016/j.tsf.2015.06.050>.
- [15] L. Jia, Y. Zhang, J. Li, C. You, E. Xie, Aligned single-walled carbon nanotubes by Langmuir-Blodgett technique, *J. Appl. Phys.* 104 (2008) 074318–074324, <https://doi.org/10.1063/1.2996033>.
- [16] K. Kędziński, K. Rytel, B. Barszcz, A. Gronostaj, Ł. Majchrzycki, D. Wróbel, On the temperature dependent electrical resistivity of CNT layers in view of

- Variable Range Hopping models, *Org. Electron. Physics, Mater. Appl.* 43 (2017) 253–261, <https://doi.org/10.1016/j.orgel.2017.01.037>.
- [17] Q. Cao, S.-J. Han, G.S. Tulevski, Y.u. Zhu, D.D. Lu, W. Haensch, Arrays of single-walled carbon nanotubes with full surface coverage for high-performance electronics, *Nat. Nanotechnol.* 8 (3) (2013) 180–186, <https://doi.org/10.1038/nnano.2012.257>.
- [18] P. Dynarowicz, W. Jawień, J.M. Trillo, N.V. Romeu, C.V. Sanchez-Caballero, E.I. Jado, et al., Molecular interaction in mixed spread films at the water/air interface, *Colloids Surfaces A Physicochem. Eng. Asp.* 97 (1995) 83–88, [https://doi.org/10.1016/0927-7757\(94\)03068-B](https://doi.org/10.1016/0927-7757(94)03068-B).
- [19] M. Rojewska, M. Skrzypiec, K. Prochaska, Surface properties and morphology of mixed POSS-DPPC monolayers at the air/water interface, *Colloids Surfaces B Biointerfaces.* 150 (2017) 334–343, <https://doi.org/10.1016/j.colsurfb.2016.10.047>.
- [20] R. Maget-Dana, The monolayer technique: A potent tool for studying the interfacial properties of antimicrobial and membrane-lytic peptides and their interactions with lipid membranes, *Biochim. Biophys. Acta* 1462 (1–2) (1999) 109–140, [https://doi.org/10.1016/S0005-2736\(99\)00203-5](https://doi.org/10.1016/S0005-2736(99)00203-5).
- [21] K. Makyła, M. Paluch, The linoleic acid influence on molecular interactions in the model of biological membrane, *Colloids Surfaces B Biointerfaces.* 71 (1) (2009) 59–66, <https://doi.org/10.1016/j.colsurfb.2009.01.005>.
- [22] A. Biadasz, K. Rytel, K. Kędzierski, A. Adamski, M. Kotkowiak, A. Stachowiak, B. Barszcz, H.Y. Jeong, T.-D. Kim, The liquid crystal induced J-type aggregation of diketopyrrolopyrrole derivatives in monolayer, *J. Mol. Liq.* 285 (2019) 598–606, <https://doi.org/10.1016/j.molliq.2019.04.093>.
- [23] S. Javadian, A. Motae, M. Sharifi, H. Aghdastinat, F. Taghavi, Dispersion stability of multi-walled carbon nanotubes in cationic surfactant mixtures, *Colloids Surfaces A Physicochem. Eng. Asp.* 531 (2017) 141–149, <https://doi.org/10.1016/j.colsurfa.2017.07.081>.
- [24] D. Lin, N.i. Liu, K. Yang, L. Zhu, Y. Xu, B. Xing, The effect of ionic strength and pH on the stability of tannic acid-facilitated carbon nanotube suspensions, *Carbon* N. Y. 47 (12) (2009) 2875–2882, <https://doi.org/10.1016/j.carbon.2009.06.036>.
- [25] A.C. Zaman, F. Kaya, C. Kaya, A study on optimum surfactant to multiwalled carbon nanotube ratio in alcoholic stable suspensions via UV-Vis absorption spectroscopy and zeta potential analysis, *Ceram. Int.* 46 (18) (2020) 29120–29129, <https://doi.org/10.1016/j.ceramint.2020.08.085>.
- [26] Y. Xu, Z. Luo, S. Li, W. Li, X. Zhang, Y.Y. Zuo, F. Huang, T. Yue, Perturbation of the pulmonary surfactant monolayer by single-walled carbon nanotubes: A molecular dynamics study, *Nanoscale.* 9 (29) (2017) 10193–10204.
- [27] L. Deng, Q. Wang, X. An, Z. Li, Y. Hu, Towards enhanced antifouling and flux performances of thin-film composite forward osmosis membrane via constructing a sandwich-like carbon nanotubes-coated support, *Desalination.* 479 (2020) 114311–114321, <https://doi.org/10.1016/j.desal.2020.114311>.
- [28] P. Wang, Y. Zheng, T. Inoue, R. Xiang, A. Shaway, M. Watanabe, A. Anisimov, E.I. Kauppinen, S. Chiashi, S. Maruyama, Enhanced In-Plane Thermal Conductance of Thin Films Composed of Coaxially Combined Single-Walled Carbon Nanotubes and Boron Nitride Nanotubes, *ACS Nano.* 14 (4) (2020) 4298–4305, <https://doi.org/10.1021/acsnano.9b09754>.
- [29] C. Cirtoaje, E. Petrescu, The influence of single-walled carbon nanotubes on the dynamic properties of nematic liquid crystals in magnetic field, *Materials (Basel).* 12 (2019) 4031–4043, <https://doi.org/10.3390/ma12244031>.
- [30] E. Petrescu, C. Cirtoaje, Dynamic behavior of a nematic liquid crystal with added carbon nanotubes in an electric field, *Beilstein J. Nanotechnol.* 9 (2018) 233–241, <https://doi.org/10.3762/bjnano.9.25>.
- [31] F. D'Souza, O. Ito, Supramolecular donor-acceptor hybrids of porphyrins/phthalocyanines with fullerenes/carbon nanotubes: Electron transfer, sensing, switching, and catalytic applications, *Chem. Commun.* (2009) 4913–4928, <https://doi.org/10.1039/b905753f>.
- [32] G. Bottari, G. de la Torre, D.M. Guldi, T. Torres, An exciting twenty-year journey exploring porphyrinoid-based photo- and electro-active systems, *Coord. Chem. Rev.* 428 (2021) 213605–213639, <https://doi.org/10.1016/j.ccr.2020.213605>.
- [33] Z. Yue, C. Ou, N. Ding, L. Tao, J. Zhao, J. Chen, Advances in Metal Phthalocyanine based Carbon Composites for Electrocatalytic CO₂ Reduction, *ChemCatChem.* 12 (24) (2020) 6103–6130, <https://doi.org/10.1002/cctc.202001126>.
- [34] V. Sgobba, G. Giancane, D. Cannolella, A. Operamolla, O. Hassan Omar, G.M. Farinola, D.M. Guldi, L. Valli, Langmuir-schaefer films for aligned carbon nanotubes functionalized with a conjugate polymer and photoelectrochemical response enhancement, *ACS Appl. Mater. Interfaces.* 6 (1) (2014) 153–158, <https://doi.org/10.1021/am403656k>.
- [35] G. Giancane, A. Ruland, V. Sgobba, D. Manno, A. Serra, G.M. Farinola, O.H. Omar, D.M. Guldi, L. Valli, Aligning single-walled carbon nanotubes by means of Langmuir-Blodgett film deposition: Optical, morphological, and photoelectrochemical studies, *Adv. Funct. Mater.* 20 (15) (2010) 2481–2488, <https://doi.org/10.1002/adfm.201000290>.
- [36] S. Abdulla, B. Pullithadathil, Unidirectional langmuir-blodgett-mediated alignment of polyaniline-functionalized multiwalled carbon nanotubes for NH₃ gas sensor applications, *Langmuir.* 36 (39) (2020) 11618–11628, <https://doi.org/10.1021/acs.langmuir.0c02200>.
- [37] C.-L. Lo, Y.-L. Lee, W.-P. Hsu, Behavior of mixed multi-walled carbon nanotube/P3HT monolayer at the air/water interface, *Synth. Met.* 160 (19–20) (2010) 2219–2223, <https://doi.org/10.1016/j.synthmet.2010.08.014>.
- [38] L.H.R.R. Possarle, J.R. Siqueira Junior, L. Caseli, Insertion of carbon nanotubes in Langmuir-Blodgett films of stearic acid and asparaginase enhancing the catalytic performance, *Colloids Surfaces B Biointerfaces.* 192 (2020) 111032–111039, <https://doi.org/10.1016/j.colsurfb.2020.11.1032>.
- [39] L. Caseli, J.R. Siqueira, High enzymatic activity preservation with carbon nanotubes incorporated in urease-lipid hybrid langmuir-blodgett films, *Langmuir.* 28 (12) (2012) 5398–5403, <https://doi.org/10.1021/la300193m>.
- [40] F.A. Scholl, P.V. Morais, R.C. Gabriel, M.J. Schöning, J.R. Siqueira, L. Caseli, Carbon Nanotubes Arranged As Smart Interfaces in Lipid Langmuir-Blodgett Films Enhancing the Enzymatic Properties of Penicillinase for Biosensing Applications, *ACS Appl. Mater. Interfaces.* 9 (36) (2017) 31054–31066, <https://doi.org/10.1021/acsami.7b08095>.
- [41] A. Stachowiak, K. Kędzierski, B. Barszcz, K. Kotwica, D. Wróbel, Determination of phthalocyanines energy gaps based on spectroscopic and electrochemical studies and DFT calculations, *J. Mol. Liq.* 341 (2021) 116800, <https://doi.org/10.1016/j.molliq.2021.116800>.
- [42] O.A. Dmitrieva, Y.B. Ivanova, A.S. Semeikin, N.Z. Mamardashvili, Fluorescence properties and quantum-chemical modeling of tert-butyl-substituted porphyrazines: Structural and ionization effect, *Spectrochim. Acta - Part A Mol. Biomol. Spectrosc.* 240 (2020) 118601–118610, <https://doi.org/10.1016/j.saa.2020.118601>.
- [43] T. Matsuura, T. Komatsu, E. Hatta, Y. Shimoyama, Enhanced orientation in Langmuir-Blodgett films of tetra-tert-butyl phthalocyanines, *Jpn. J. Appl. Phys.* 39 (Part 1, No. 4A) (2000) 1821–1825.
- [44] P. Dynarowicz-Latka, K. Kita, Molecular interaction in mixed monolayers at the air/water interface, *Adv. Colloid Interface Sci.* 79 (1) (1999) 1–17, [https://doi.org/10.1016/S0001-8686\(98\)00064-5](https://doi.org/10.1016/S0001-8686(98)00064-5).
- [45] P.O. Krasnov, T.V. Basova, A. Hassan, Interaction of metal phthalocyanines with carbon zigzag and armchair nanotubes with different diameters, *Appl. Surf. Sci.* 457 (2018) 235–240, <https://doi.org/10.1016/j.apsusc.2018.06.282>.
- [46] W. Bauhofer, J.Z. Kovacs, A review and analysis of electrical percolation in carbon nanotube polymer composites, *Compos. Sci. Technol.* 69 (10) (2009) 1486–1498, <https://doi.org/10.1016/j.compscitech.2008.06.018>.
- [47] I. Balberg, Tunneling and nonuniversal conductivity in composite materials, *Phys. Rev. Lett.* 59 (12) (1987) 1305–1308, <https://doi.org/10.1103/PhysRevLett.59.1305>.
- [48] F. Dalmas, J.-Y. Cavallé, C. Gauthier, L. Chazeau, R. Dendievel, Viscoelastic behavior and electrical properties of flexible nanofiber filled polymer nanocomposites. Influence of processing conditions, *Compos. Sci. Technol.* 67 (5) (2007) 829–839, <https://doi.org/10.1016/j.compscitech.2006.01.030>.
- [49] I. Jurewicz, P. Worajittiphon, A.A.K. King, P.J. Sellin, J.L. Keddie, A.B. Dalton, Locking carbon nanotubes in confined lattice geometries - A route to low percolation in conducting composites, *J. Phys. Chem. B.* 115 (20) (2011) 6395–6400, <https://doi.org/10.1021/jp111998p>.
- [50] H.S. Lee, C.H. Yun, S.K. Kim, J.H. Choi, C.J. Lee, H.-J. Jin, H. Lee, S.J. Park, M. Park, Percolation of two-dimensional multiwall carbon nanotube networks, *Appl. Phys. Lett.* 95 (13) (2009) 134104, <https://doi.org/10.1063/1.3238326>.

The influence of zinc phthalocyanine on the formation and properties of multiwalled carbon nanotubes thin films on the air-solid and air-water interface

K. Rytel¹, K. Kędzierski¹, B. Barszcz², B. Biadasz¹, Ł. Majchrzycki³, D. Wróbel¹

1. Faculty of Materials Engineering and Technical Physics, Institute of Physics, Poznan University of Technology, Piotrowo 3, 60-965 Poznań, Poland.

E-mail: karol.rytel@put.poznan.pl

2. Institute of Molecular Physics, Polish Academy of Sciences, Smoluchowskiego 17, 60-179 Poznań, Poland

3. Centre for Advanced Technology, Adam Mickiewicz University, Uniwersytetu Poznańskiego 10, 61-614 Poznań, Poland

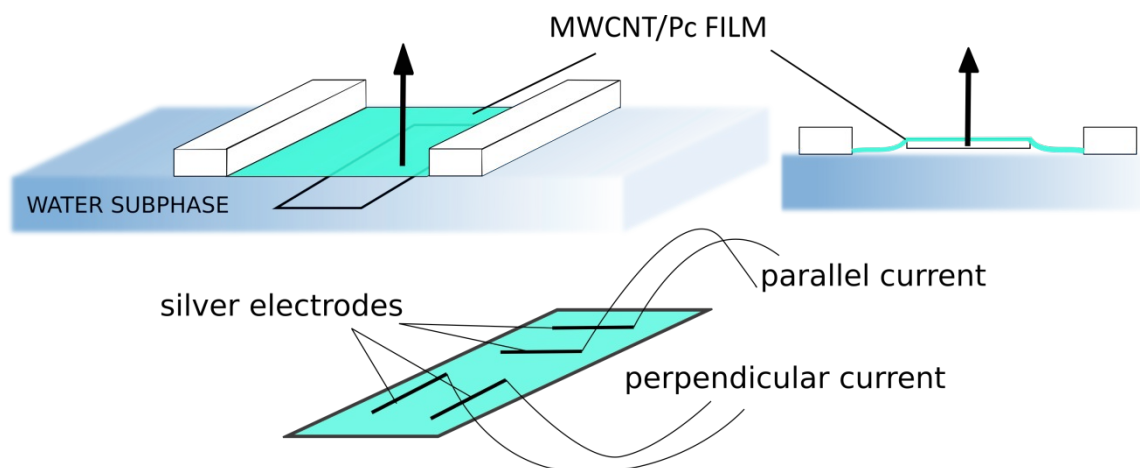


Fig. S1 Experiment setup diagram

Table S2 Table of operating conditions

Teflon trough area [cm ²]	Teflon trough dimensions [cm ²]	Temperature [°C]	Solvent evaporation time [min]	Barriers speed [mm min ⁻¹]	Substrate removal speed [mm min ⁻¹]	Relaxation time [min]
750	15 x 50	20 ± 0.5	30	5	1	50

Table S1 Mixtures parameters used for preparation of Langmuir films, where V_{MWCNT} is the volume of MWCNT suspension, V_{PC} is the volume of PC solution MF is mass fraction, C_{MWCNT} and C_{PC} is MWCNT and PC concentration, respectively; Π_T is the surface pressure at which films was trasfered

MF of MWCNT	MF of PC	V_{MWCNT} [ml]	V_{PC} [ml]	C_{MWCNT} [$\mu\text{g ml}^{-1}$]	C_{PC} [$\mu\text{g ml}^{-1}$]	Π_T [mN m ⁻¹]
1	0	5	0	20	0	40
0.95	0.05	5	0.0625	19.75	0.002	-

0.91	0.09	5	0.125	19.51	1.96	39
0.83	0.17	5	0.250	19.05	3.82	38
0.77	0.23	5	0.375	18.60	5.60	37
0.71	0.29	5	0.5	18.18	7.29	35
0.65	0.35	3.75	0.5	17.65	9.44	34
0.55	0.45	2.5	0.5	16.67	13.36	33
0.38	0.62	1.25	0.5	14.28	22.91	32
0	1	0	0.5	0	80.20	30

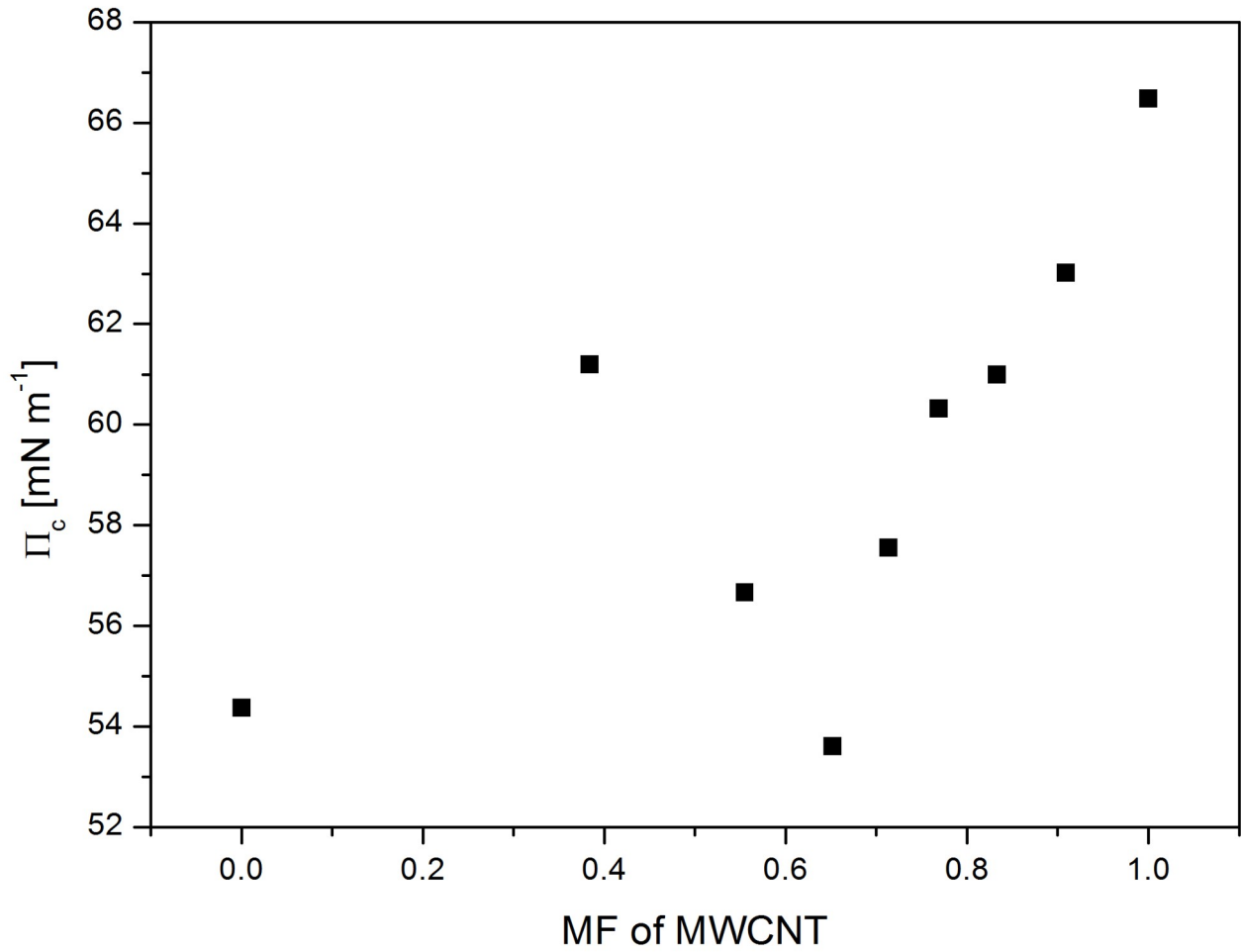


Fig. S2 Surface pressure at which films collapse occurs vs mass fraction of MWCNT

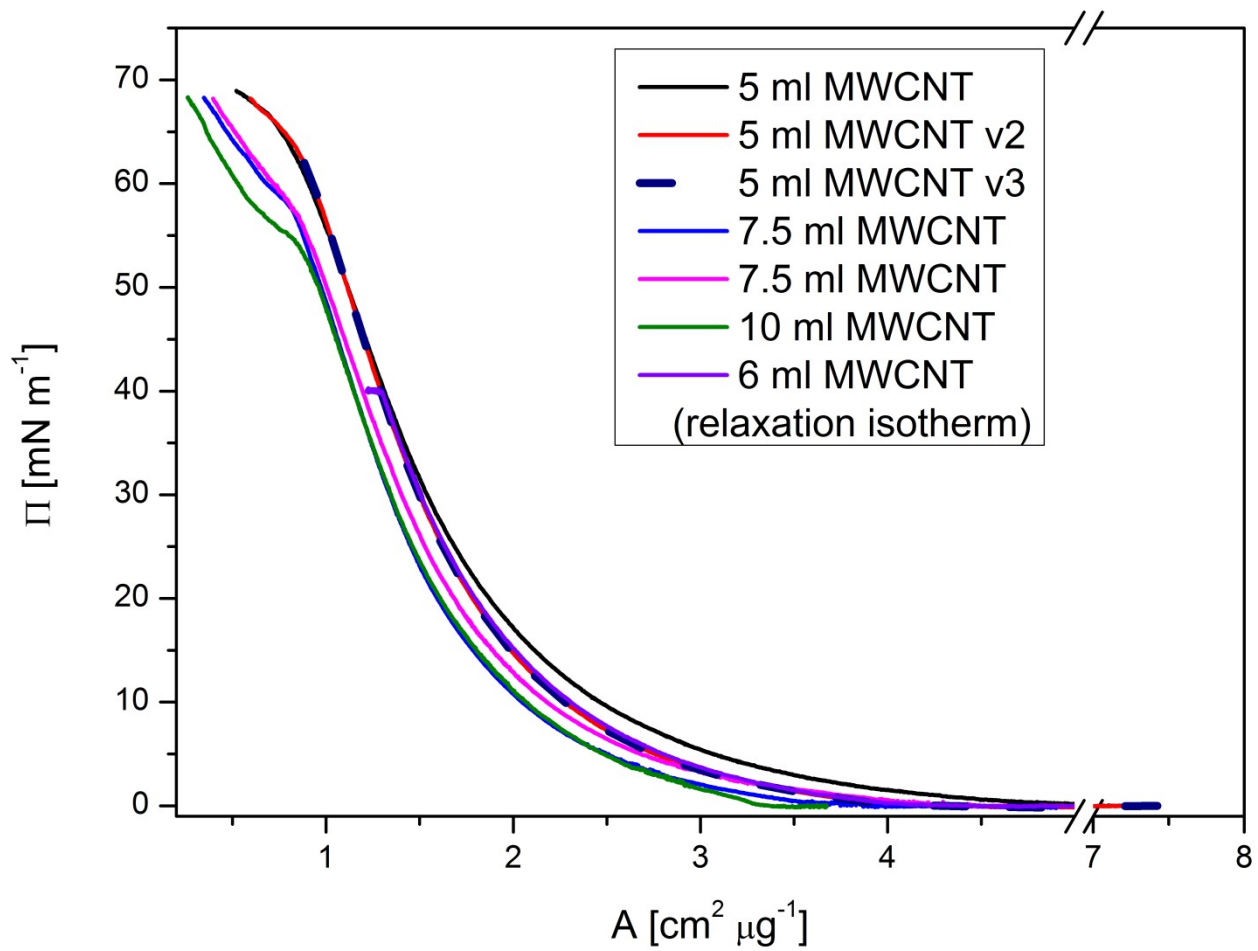


Fig. S3 Surface pressure vs area per unit mass of MWCNT for various amount of MWCNT suspension

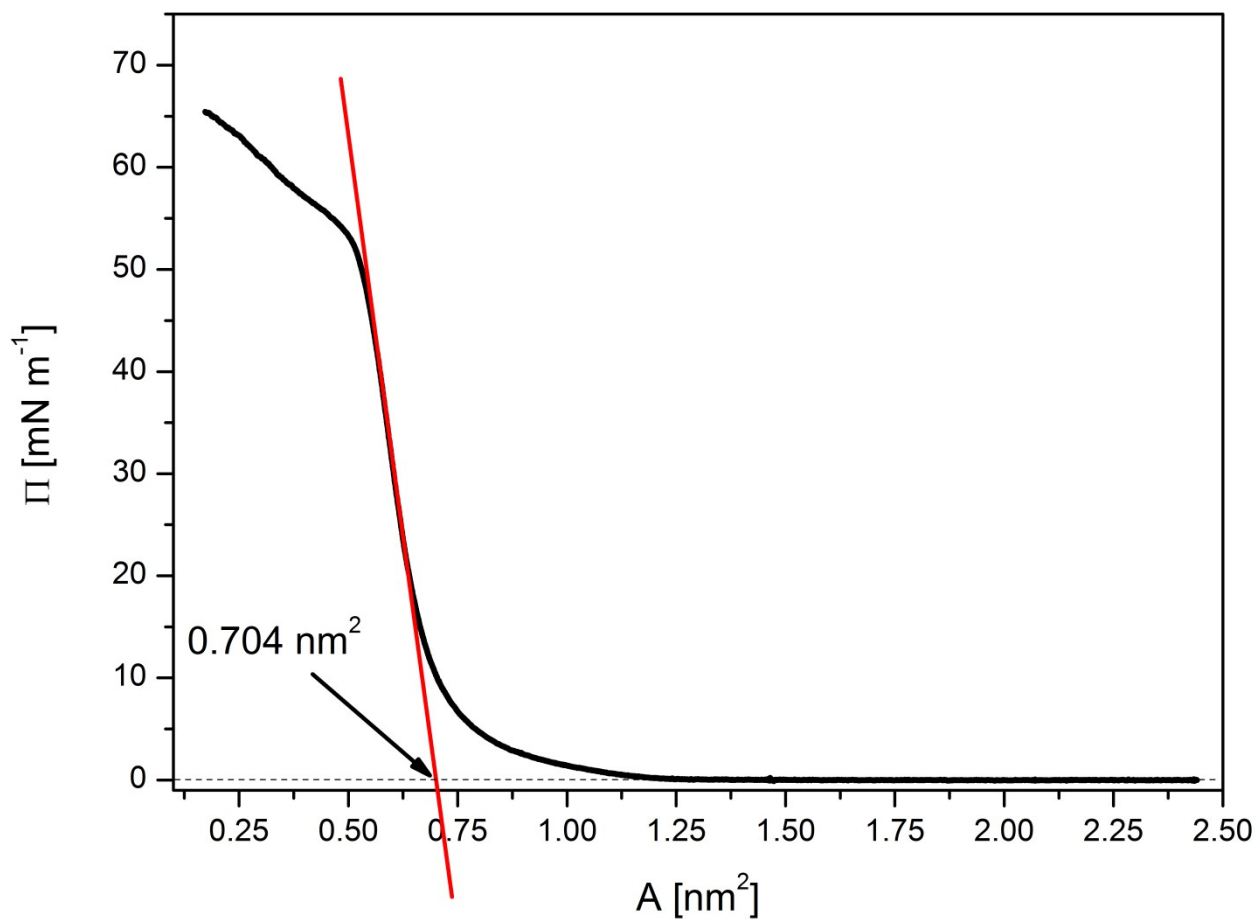


Fig. S4 Surface pressure vs area per molecule measured for pure PC

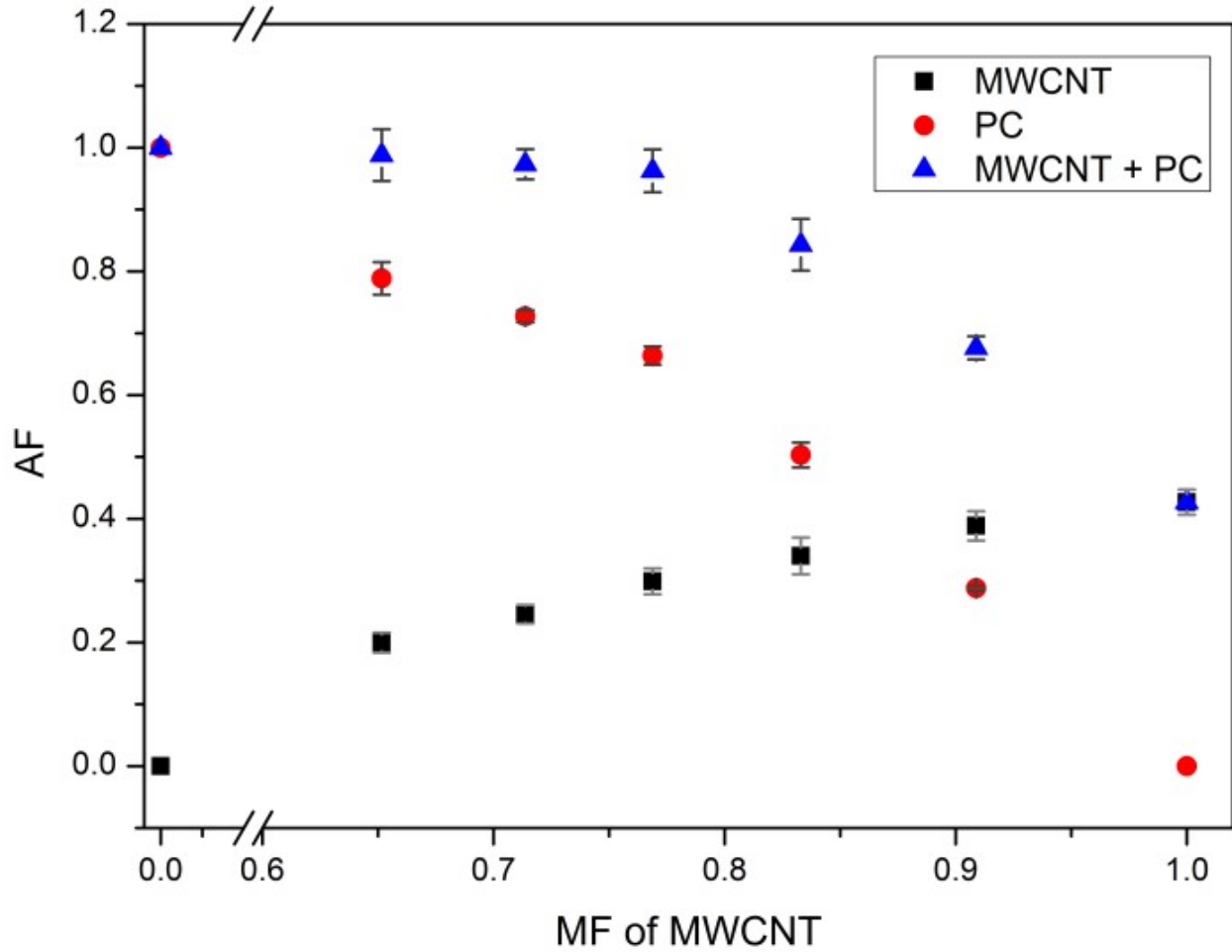


Fig. S5 Area fraction (AF) vs mass fraction (MF) of MWCNT calculated from isotherms obtained during transfer process

The relative measurement uncertainty can be calculated by following equation:

$$\frac{\Delta AF}{AF} = \frac{\Delta A_1}{A_1} + \frac{\Delta A_{\text{exp}}}{A_{\text{exp}}} + \frac{\Delta FF}{FF}$$

where ΔA_1 , ΔA_{exp} and ΔFF are the measurement errors of the area per unit mass of selected mixture component. The estimated AF relative error for our measurements was in range of 4.7-8.7 % and 0.4-2.6 % for MWCNT and PC, respectively. We estimated the relative errors of A_1 and A_{exp} from the highest difference between the values recorded for multiple Π -A measurements of the corresponding mixture. The largest contribution in the AF relative error has Fill Factor (50-78 % of total error)

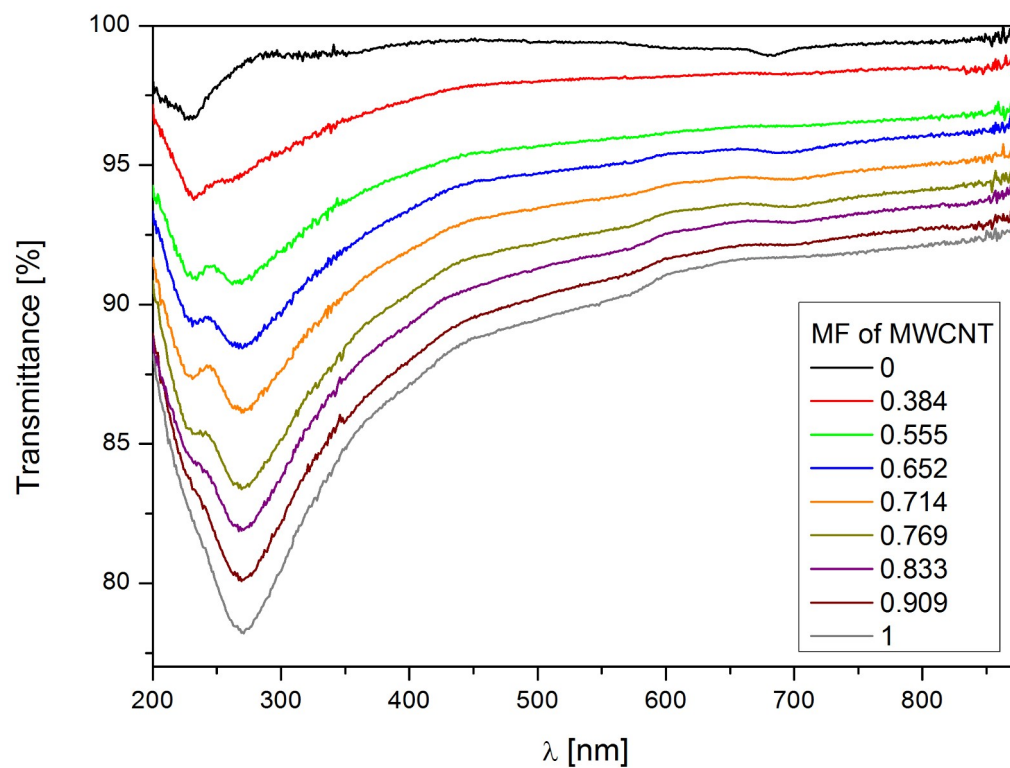


Fig. S6 UV-Vis spectra of MWCNT/PC films obtained for various mass fraction of MWCNT

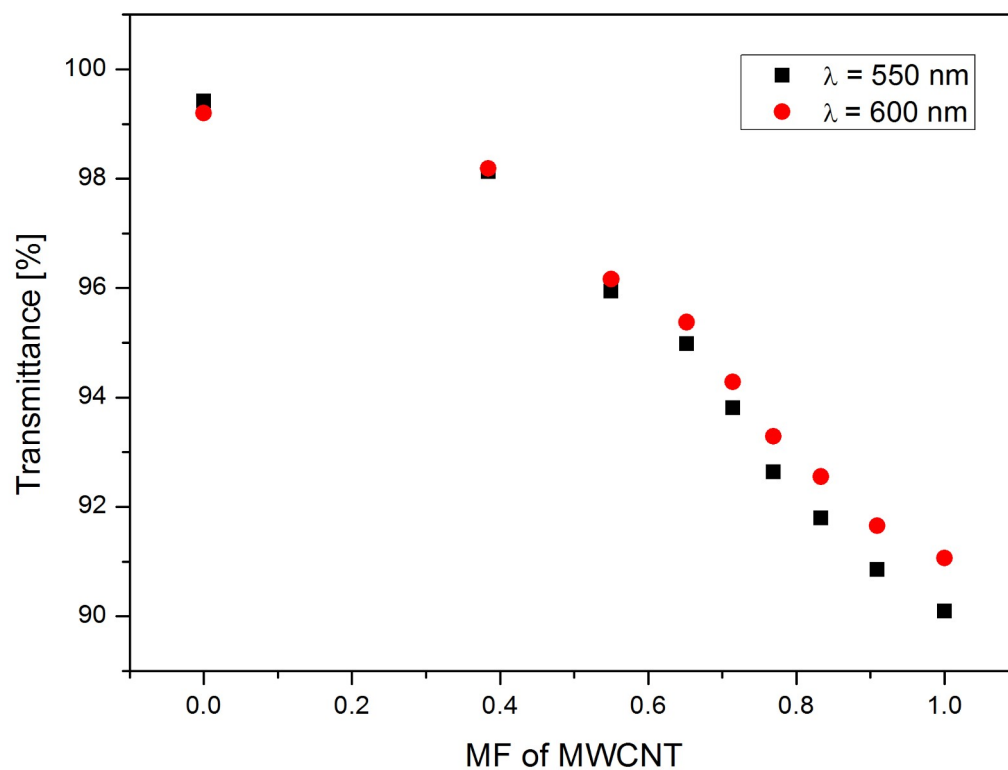


Fig. S7 Transmittance of MWCNT/PC films at a wavelengths of 550 nm and 600 nm

CNT MF	×20 MAT	×20 FLUO	× 30 000 SEM	×100 000 SEM
1				
0.91				
0.83				
0.77				
0.71				
0.65				
0.55				
0.38				
0				

Fig. S 8 LSM images in the material and fluorescent mode and SEM images obtained for the films with various mass fraction of MWCNT

Przedruk publikacji [Rytel Electr 2016]

K. Rytel, D. Waszak, K. Kędziński, D. Wróbel,

*Novel method of current collector coating by multiwalled carbon nanotube
Langmuir layer for enhanced power performance of LiMn_2O_4 electrode of Li-ion
batteries, Electrochim. Acta. 222 (2016) 921–925.*

doi:10.1016/j.electacta.2016.11.058.

(MEiN 40, IF 4,798)



Novel method of current collector coating by multiwalled carbon nanotube Langmuir layer for enhanced power performance of LiMn_2O_4 electrode of Li-ion batteries



Karol Rytel^a, Daniel Waszak^b, Kamil Kędzierski^a, Danuta Wróbel^{a,*}

^a Faculty of Technical Physics, Poznań University of Technology, ul. Piotrowo 3, 60-965 Poznań, Poland

^b Institute of Non-Ferrous Metals, Division in Poznań, Central Laboratory of Batteries and Cells, Department of Advanced Materials, ul. Forteczna 12, 61-362 Poznań, Poland

ARTICLE INFO

Article history:

Received 12 August 2016

Received in revised form 9 November 2016

Accepted 9 November 2016

Available online 14 November 2016

ABSTRACT

Lithium manganese oxide (LiMn_2O_4) of spinel structure is a very attractive and widely applied active material for lithium ion cells because of high potential vs. metallic lithium content, non-toxicity and low cost of production. Unfortunately, the capacity fading at higher current densities limits its application in fast charging batteries. One of the solutions to this problem is modification of the interface between the current collector and the cathode mass. In this paper we proposed a modification of aluminum current collector by coating it with a thin film of multiwalled carbon nanotubes. Two variants of Langmuir-Schaefer method have been used for the first time to produce the film modifying the interface between the collector and the active material. The proposed modification of the current collector resulted in reduction of charge-transfer resistance and consequently in increasing cells capacity at high current densities.

© 2016 Elsevier Ltd. All rights reserved.

1. Introduction

Because of high energy density, lithium ion batteries have been widely applied in electric vehicles, portable electronics and smart grids [1–6]. Lithium manganese oxide LiMn_2O_4 (LMO) of spinel structure has several advantages over layered Ni or Co oxide, such as low cost, high discharge potential (4 V vs. Li/Li^+) and reasonable theoretical capacity of 148 mA h g^{-1} . The major disadvantage of this material is high capacity fading during charge-discharge cycles and capacity fading at higher current densities which limits its application in industry [7,8]. This drawback can be related to the few factors: manganese dissolution, Jahn-Teller distortion at the state of deep discharge and LMO spinel instability [9,10]. Recent studies have shown that a carbon coated current collector can reduce charge-transfer resistance, resulting in the enhanced power performance [11–14]. In this work we focus on modification of the interface between the Al current collector and the LMO-based active mass with multiwalled carbon nanotubes (MWCNTs). In order to prevent increasing electric resistance, the aluminum substrate was coated with a thin film of multiwalled carbon

nanotubes using the Langmuir-Schaefer method. The Langmuir layers of carbon nanotubes were used for the first time as the current collector modification to bring significant improvement in the cell parameters in high current density tests.

2. Experimental methods

In this work MWCNT (Sigma-Aldrich, diameter 6–9 nm, length 5 μm) Langmuir layers were used to modify the current collector in lithium ion cells. Langmuir layers were produced from MWCNTs suspension in chloroform of a concentration lower than 0.15 mg ml^{-1} , the details are given in supplementary material (Appendix A). The floating film preparation is described in details in supplementary material (Appendix B) and in our previous work [15]. The scheme of Langmuir layer formation is presented in Fig. B.1 (Appendix B). Standard surface pressure vs. area isotherm of MWCNT floating film was recorded and is presented in Fig. 1. The MWCNT Langmuir layers were deposited on an aluminum foil ($10 \times 10 \text{ cm}$). The Al foil was cleaned with isopropanol and chloroform prior to layer deposition. Two horizontal transfer methods (Langmuir-Schaefer) were used to cover Al foils. In the first method (L1) the substrate was emerged from the subphase and it was coated with a compressed MWCNTs film. In the second method (L2) the layer was transferred onto the substrate by gently

* Corresponding author.

E-mail address: danuta.wrobel@put.poznan.pl (D. Wróbel).

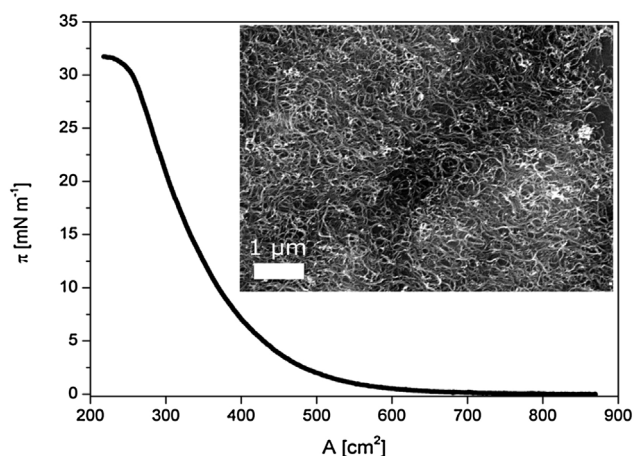


Fig. 1. Isotherm of surface pressure vs. area of the MWCNTs layer. Inset – the SEM image of the MWCNT layer.

stamping the MWCNT film on the water surface. The raising and lowering speed of the substrates in both methods was 1 mm min^{-1} . The schemes of L1 and L2 transfer methods are presented in Fig. B.2 (Appendix B). The Al current collectors modified by only one MWCNT layer were used in the study. Attempts to transfer MWCNT multilayers were made, however the coverage proved to be highly inhomogeneous. The optical image of Al substrate coated by mono

and double layer of MWCNTs is presented in Fig. C.1 (Appendix C). It is rather impossible to evaluate the MWCNTs transfer ratio, however, the laser scanning confocal microscopy (not shown) and SEM examinations (Fig. 1 inset) indicate good and homogeneous coverage. The average mass of MWCNT thin film transferred onto Al substrate (m_{CNT}) can be estimated from the equation:

$$m_{\text{CNT}} = \frac{CV}{A}$$

where C is the concentration of MWCNT (w/v) in suspension, V is the suspension volume dispersed on the subphase and A is the surface area between the barriers at the target surface pressure. Using the surface area between barriers (A) at the targeted surface pressure from Fig. 1, m_{CNT} was estimated to be lower than $1 \mu\text{g cm}^{-2}$. Taking into account the MWCNT diameter distribution of 6–9 nm, we can conclude that the surface of Al substrate was not fully coated. Assuming the average density of the MWCNT of around 1.5 g cm^{-3} the average thickness of the layer is smaller than 6 nm. The MWCNT films are homogenous in the macro-scale and well distributed on very large area – as follows from our experience the only limitation of the area covered is the surface of the Langmuir trough used. On the other hand, L1 and L2 films analyzed in the micro-scale are formed as tangled networks of individual and bundled MWCNTs. The inset of Fig. 1 shows the SEM image of MWCNT L1 layer transferred onto Al substrate. The layer is characterized by randomly dispersed holes of uncovered Al substrate and few larger aggregates of MWCNTs. The transferred

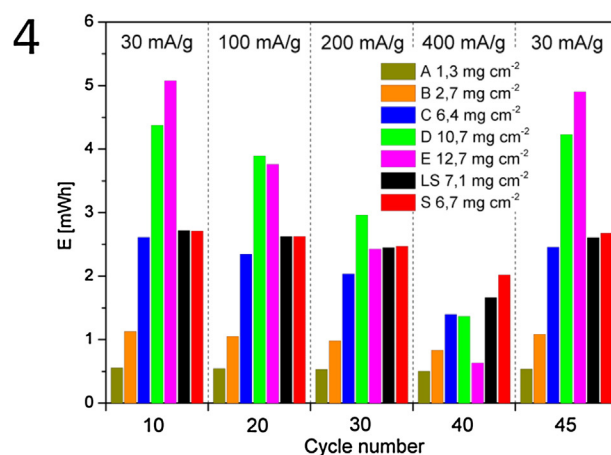
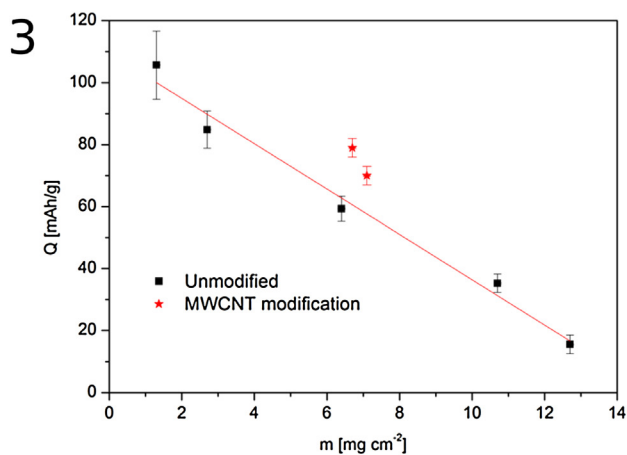
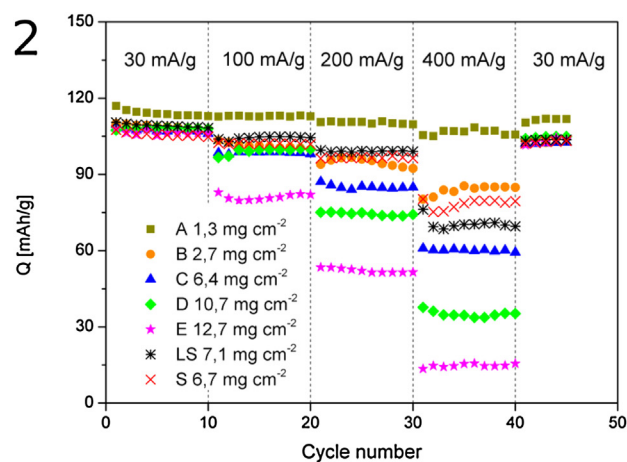
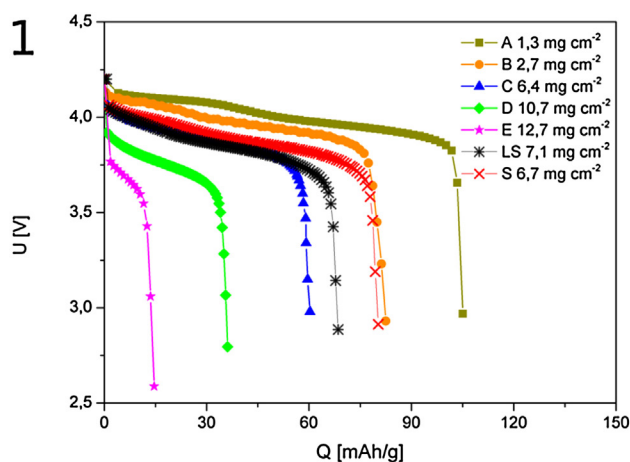


Fig. 2. Basic electrochemical parameters; 1 – a comparison of discharge profiles at the 40th cycle (from Fig. 2.2); 2 – the specific discharge capacities of LiMn₂O₄ electrodes with various active mass loadings of the electrode with unmodified current collectors (A–E) and with a modified current collector (LS, S), the cells are charged/discharged with current densities varied from 30 to 400 mA h^{-1} ; 3 – the specific discharge capacities (40th cycle) of the modified and unmodified electrodes vs. active mass loading (linear fit for the unmodified electrode for better presentation of the modification influence); 4 – energy stored in the electrodes at the last cycle of each current density.

layer is transparent because of its thickness. The total reflectance spectra of Al substrate and MWCNTs L1 layer transferred onto Al is shown in Fig. C.2 and described in supplementary material (Appendix C). The optical and electrical properties of MWCNT Langmuir layer transferred onto glass and polymer are presented in our previous papers [15,16]. Although the loading of MWCNTs is light, the modification of the aluminum foil surface results in significant changes in the interface between the current collector and the active material.

The cathode active material (LiMn_2O_4) was synthesized via the modified sol-gel method proposed by B. Hamankiewicz et al. and standard cathode preparation procedure was used [17,18]. Details of the cells preparation and electrochemical tests are given in supplementary material Appendix D and Appendix E respectively. Also the cross section SEM image of the C electrode is shown in Fig. D.1 (Appendix D). Five unmodified electrodes of the active mass loading between 1.3 and 12.7 mg cm^{-2} were prepared as reference samples (samples A–E in Fig. 2). The MWCNTs modified electrodes were coated with the active material mass loading of 7.1 (sample LS) and 6.7 mg cm^{-2} (sample S) using the L1 and the L2 methods, respectively. The active mass loadings of modified electrodes were chosen to ensure the highest reproducibility. Standard deviation of the electrodes with mass loading about 7 mg cm^{-2} was within the measurement error ($\pm 3 \text{ mA h g}^{-1}$) at all current densities tested. For the electrochemical test the electrodes were assembled in the two-electrode Swagelok type system with a lithium metal foil (Sigma-Aldrich, 99%) as the reference electrode. The cells were tested by chronopotentiometry using the constant current mode in the varied potential range. The experiments were performed under conditions similar to the operating parameters of commercial cells. Charge (discharge) current density rates varied from 30 to 400 mA g^{-1} . In addition the electrochemical impedance spectroscopy (EIS) analysis was carried out to characterize the cathode resistance.

3. Results and discussion

The chronopotentiometric curves of discharging are presented in Fig. 2.1 and reveal a two-step voltage profile with the plateaus near 3.95 V and 4.09 V for the electrodes with the low active mass loadings (samples A and B). The plateaus are attributed to Li^+ insertion/removal from 8a sites. At the higher potential plateau, the Li–Li interaction does not occur in contrast to the situation at the lower potential plateau. For the high active mass loadings (sample D) the higher plateau is not observed due to the electrode polarization effect [20]. For E electrode no visible plateau is recorded. Decrease in the potential vs. Li/Li^+ reduction is caused by an increase in the active mass loading. The shape of chronopotentiometric curves of the modified electrodes (samples S and LS) is similar to that of the curves recorded for the low active mass loading electrodes (samples A–C). The potential vs. Li/Li^+ recorded for the S electrode was even higher than that for the electrode C which had 0.3 mg cm^{-2} less active mass loading. The LS electrode potential vs. Li/Li^+ was the same as that observed for the electrode C, although the active mass loading was by 0.7 mg cm^{-2} higher.

Fig. 2.2 shows the specific discharge capacities (Q) of the modified (S, LS) and the unmodified electrodes (A–E) with various active mass loadings. In the first cycle, the highest specific capacity 117 mA h g^{-1} was achieved for the electrode with the lowest active mass loading (1.3 mg cm^{-2}), while the specific capacity of the remaining electrodes was in the range 110 – 107 mA h g^{-1} . Moreover, in the first cycle the specific capacity difference between the best and the worst electrode was 10 mA h g^{-1} and at the 10th cycle this difference decreased to 7 mA h g^{-1} . For the active mass loadings between 2.7 mg cm^{-2} and 10.7 mg cm^{-2} , major changes in the specific capacities were observed at the current densities

200 and 400 mA g^{-1} . In the 40th cycle, the specific capacities of the modified electrodes were higher when compared to those of the electrode C which had active mass loading similar to that of the modified electrodes. The differences were 20 and 11 mA h g^{-1} for S and LS electrodes, respectively. After 45 cycles, the specific capacity retention was not higher than 6% for all electrodes tested. The specific capacities of the electrodes A–E decreased linearly with increasing active mass loadings in the mass range studied, as shown in Fig. 2.3. For the MWCNT modified collectors, a clear deviation from the linear fit of unmodified electrodes capacities versus active mass loading was observed. The LS and S electrodes were characterized by significantly higher capacities than those implied by the linear fit of the capacities of the unmodified electrodes with the same active mass loadings. With increasing current density, the specific capacities were reduced more rapidly for the electrodes with higher active mass loadings. A similar effect has been observed by Hamankiewicz et al. [17] and explained by Thunman et al. [19]. A possible explanation is that the specific capacity of the electrode was reduced by the electric resistance and ion transport in it.

In order to get more information on the impact of the current collector modification, the energy stored in electrodes (E_s) was calculated from the equation defining it:

$$E_s = I \int_0^t U(t) dt$$

where $U(t)$ is the electrode potential vs. Li/Li^+ , I is the current used to discharge the electrodes and t is the time of discharging the electrode measured between 4.2 and 3.0 V potential vs. Li/Li^+ . The results are presented in Fig. 2.4. The highest energy stored in the electrodes was recorded for electrode E (12.7 mg cm^{-2}) at 30 mA g^{-1} current density. Increasing the current density resulted in a more rapid decrease in the energy stored in the electrodes with higher mass loading. As expected, the electrodes with the modified current collector were characterized by the highest energy stored at the highest current density of 400 mA g^{-1} . The values of energy stored in LS and S electrodes are 1.6 and 2.0 mW h , respectively. These values are by about 18% and 42% higher when compared to the corresponding values for C electrode. For the current density of 200 mA g^{-1} the energy stored in the two modified electrodes was by 22% higher than that stored in electrode C. Moreover, the energy stored in the modified electrodes decreased more slowly with increasing current density, Especially when compared to that stored in the electrodes with the highest active mass loading (sample E).

The above results indicate that the presence of MWCNTs in the interface between the Al foil and the active mass causes a reduction in electrical resistance [12–14], which results in improving the electrode parameters: specific capacities, storage energy and potential vs. Li/Li^+ . The effect is especially pronounced for high current densities tested. To verify the effect of modification of the current collector with the MWCNT layer, the electrochemical impedance spectroscopy was also performed. In Fig. 3 the Nyquist plots and the equivalent circuits of electrodes C, LS and S are shown.

For the electrode with the unmodified current collector (sample C), the inclined line at the low frequency associated with the diffusion process and one semi-circle at the high frequency originated from the charge transfer reaction, were recorded [14]. Moreover, at the highest frequency an additional small semi-circle was detected for the modified electrodes. The small semi-circle originated from the additional interface made of the MWCNT layer between the current collector and the cathode mass. A similar effect has been observed by Chen et al. [14] but the small semi-

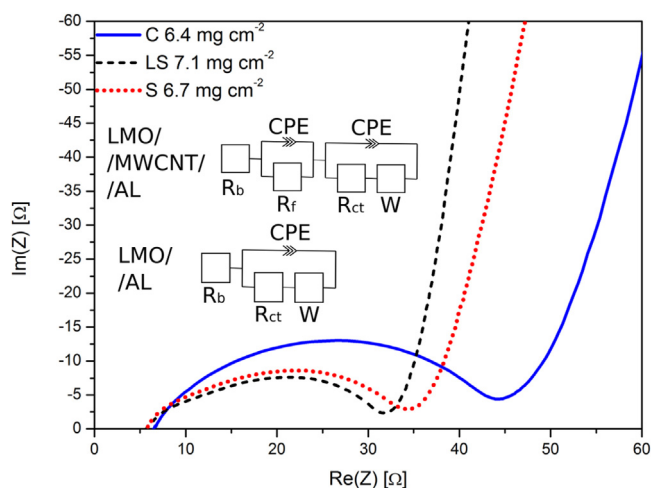


Fig. 3. Nyquist plots and the equivalent circuits of cells with the modified (LS and S) and the unmodified (C) current collector; R_b – bulk resistance of cell, CPE – constant phase element, R_f – interfacial resistance due to MWCNTs layer, R_{ct} – charge transfer resistance, W – Warburg impedance.

circle was observed at a medium frequency. In the modified cathode, part of the charge is transferred directly from the active mass to Al current collector and the remaining charge reaches the current collector through the network of carbon nanotubes. This modification results in improvement in the cathode parameters at higher current densities. As a result of the MWCNT layer, the interfacial resistances expressed by R_f parameters of the electrodes LS and S, were fitted as 10Ω and 8Ω , respectively. In our work the proposed modification of the current collector results in a decrease in the charge transfer resistance (R_{ct}) parameter from 39Ω for electrode C to 22Ω and 25Ω for the electrodes LS and S, respectively. The EIS results are summarized in Table 1.

The improvement in the electrochemical parameters in the MWCNT modified electrodes can be explained in two ways: as a result of upgrading the electrical transport in the electrode and enhancement of adhesion between the active mass and the Al collector. The improvement in adhesion for the MWCNT modified electrodes, when compared to that in the unmodified electrodes was observed as we tried to clean the modified and unmodified collector surface. We were able to easily clean the whole surface of the unmodified collector by simple mechanical peeling off the active mass. For the MWCNT modified electrodes intensive polishing had to be used to fully clean the collector. The influence of adhesion at the active layer/current collector interface Li-ion

Table 1

Summarized data of the electrodes with the modified (LS and S) and the unmodified (C) current collector; where R_b – bulk resistance of cell, R_f – interfacial resistance due to MWCNTs layer, R_{ct} – charge transfer resistance, W – Warburg impedance.

Electrode type	C	LS	S
Active mass loading [mg cm^{-2}]	6.4	7.1	6.7
Capacity retention [%]	4.6	6.3	3.7
EIS results			
R_b	7	6	6
R_f	–	10	8
R_{ct}	39	22	25
R_{cel}	46	32	35
W	49	32	36
Cycle number	Current densities [mA g^{-1}]	Specific Capacity [mAh g^{-1}]	
		C	S
1	30	108	111
10	30	106	108
20	100	98	104
30	200	85	99
40	400	59	70
45	30	103	104

batteries has been analyzed by Wu et al. [12]. Moreover, the modified electrodes are characterized by significantly lower resistance than the unmodified ones. Also an additional small semi-circle is observed in the Nyquist plots (Fig. 3) recorded for the modified electrodes which indicates significant influence of MWCNT layer on electrode electrical transport as observed by Chen et al. [14].

The SEM and LSM investigation shows no differences between MWCNT layers obtained by the L1 and L2 methods: However, the electrochemical performance of the modified electrodes is different for the layers deposited in L1 and L2 process. The only difference in the layers created by L1 and L2 methods is the contact time with water. In L1 method the collector before deposition remains in water for 2 h and after deposition it is wet and subjected to drying for about 1 h in air. In L2 method the Al substrate dries immediately after MWCNT transfer and the Al collector contact with water does not exceed 5 min. The native AlO_x passivation layer is present on the Al collector surface before and after MWCNT deposition and it can be extended in corrosion process accelerated by water contact. Shorter contact with water can explain higher capacity of S electrode at high current density experiment than that of LS electrode. On the other hand, the resistance parameters obtained from EIS experiments are higher for S electrode, which contradicts the idea of insulating effect of AlO_x layer. However, the difference in specific capacities between the S and LS electrodes is slight, especially taking into account the sensitivity of LMO based cells to active mass loadings changes in high current densities experiments – the effect is clearly seen in Fig. 2.3 for unmodified electrodes capacities. The LS electrode active mass loading is higher than that of S electrodes, which can explain the differences in capacities. Moreover, taking into account the measurement uncertainty, we can conclude that the differences between the capacities of S and LS electrodes are negligible.

4. Conclusion

In conclusion, the MWCNTs thin film on the aluminum current collector was fabricated using two Langmuir-Schaefer deposition techniques. The greatest advantage of the Langmuir-Schaefer deposition technique is the ability to transfer large scale thin films whose size is limited only by the dimensions of the Langmuir trough. The amount of material used for the thin film coating (less than $1 \mu\text{g cm}^{-2}$) is also negligible in terms of material cost and total weight of the electrodes produced. Moreover, the electrodes with modified current collectors demonstrated better power performance than those with the unmodified current collector with similar active mass loading. The specific capacities were increased more than 18% and 33% for the electrodes LS and S, respectively, when compared that of electrode C at the current density 400 mA g^{-1} . More than 10% increase in the specific capacities at the current density 200 mA g^{-1} was revealed for the electrodes LS and S. The energy stored in electrodes LS and S was higher by about 43% and 19%, respectively, when compared to that s for electrode C. The improved properties of the MWCNT modified electrodes result from the lower electrical resistance at the interface between the electrode and the active mass. The charge transfer resistance decreased more than 35% for the MWCNTs modified electrodes when compared to that of electrode C. The electrochemical investigation of the cells was performed under conditions similar to those defined by the operating parameters of commercial cells. However, the Langmuir method is “time consuming” and the study presented is mostly cognitive in character. Nevertheless, the proposed modification of the current collector is worth considering for Li-ion batteries applications.

Acknowledgements

The authors thank Dr Bolesław Barszcz from the Institute of Molecular Physics, Polish Academy of Sciences for his helpful discussion on the experimental techniques. This work was supported by the National Center for Research and Development “Research and development of modern technologies of lithium-ion batteries with polymer electrolytes with enhanced operation safety” (grant No. **PBS1/A1/2012 DW**), Poznan University of Technology (grant No. **06/62/DSPB/0216**, KR, DWr,) and National Science Centre of Poland (grant No. **2015/17/N/ST8/00295**, KK)

Appendix A. Supplementary data

Supplementary data associated with this article can be found, in the online version, at <http://dx.doi.org/10.1016/j.electacta.2016.11.058>.

References

- [1] B. Scrosati, J. Hassoun, Y.K. Sun, Lithium-ion batteries A look into the future, *Energy Environ. Sci.* 4 (2011) 3287–3295.
- [2] M. Armand, J.M. Tarascon, Building better batteries, *Nature* 451 (2008) 652–657.
- [3] J.M. Tarascon, Key challenges in future Li-battery research, *Philos. Trans. A. Math. Phys. Eng. Sci.* 368 (2010) 3227–3241.
- [4] M. Walkowiak, D. Waszak, B. Gierczyk, G. Schroeder, Impact of selected supramolecular additives on the initial electrochemical lithium intercalation into graphite in propylene carbonate, *Cent. Eur. J. Chem.* 6 (2008) 600–606.
- [5] P. Pórolniczak, A. Arunthathy Surendran, M. Walkowiak, S. Thomas, A.M. Stephan, Low Resistance, Carbon Black-free Magnetite Anode for Li-ion Batteries Obtained by One-step Attachment of Carbon Nanotubes, *J. New Mat. Electr. Sys.* 17 (2014) 225–230.
- [6] M. Walkowiak, D. Waszak, G. Schroeder, B. Gierczyk, Enhanced graphite passivation in Li-ion battery electrolytes containing disiloxane-type additive/co-solvent, *J. Solid State Electrochem* 14 (2010) 2213–2218.
- [7] B. Put, P.M. Vereecken, N. Labyedh, A. Sepulveda, C. Huyghebaert, I.P. Radu, et al., High Cycling Stability and Extreme Rate Performance in Nanoscaled LiMn₂O₄ Thin Films, *ACS Appl. Mater. Interfaces* 7 (2015) 22413–22420.
- [8] R.E. Warburton, H. Iddir, L.A. Curtiss, J. Greeley, Thermodynamic Stability of Low- and High-Index Spinel LiMn₂O₄ Surface Terminations, *ACS Appl. Mater. Interfaces* (2016), doi:<http://dx.doi.org/10.1021/acsami.6b01069>.
- [9] B. Scrosati, J. Garche, Lithium batteries: Status, prospects and future, *J. Power Sources* 195 (2010) 2419–2430.
- [10] T. Yi, X. Hu, K. Gao, Synthesis and physicochemical properties of LiAlO₂.05Mn_{1.95}O₄ cathode material by the ultrasonic-assisted sol-gel method, *J. Power Sources* 162 (2006) 636–643.
- [11] K. Striebel, J. Shim, A. Sierra, H. Yang, X. Song, R. Kostecki, et al., The development of low cost LiFePO₄-based high power lithium-ion batteries, *J. Power Sources* 146 (2005) 33–38.
- [12] H.C. Wu, H.C. Wu, E. Lee, N.L. Wu, High-temperature carbon-coated aluminum current collector for enhanced power performance of LiFePO₄ electrode of Li-ion batteries, *Electrochem Commun.* 12 (2010) 488–491.
- [13] J. Guo, A. Sun, C. Wang, A porous silicon-carbon anode with high overall capacity on carbon fiber current collector, *Electrochem Commun.* 12 (2010) 981–984.
- [14] S. Chen, K. Chiu, S. Su, S. Liu, K.H. Hou, H. Leu, et al., Low contact resistance carbon thin film modified current collectors for lithium ion batteries, *Tin Solid Films* 572 (2014) 56–60.
- [15] K. Kędzierski, K. Rytel, Ł. Majchrzycki, D. Wróbel, Conductive and transparent films of oriented multi-walled carbon nanotubes by Langmuir-Schaefer method, *Thin Solid Films*. 589 (2015) 701–706.
- [16] K. Kędzierski, B. Barszcz, A. Biadasz, M. Matczak, D. Wróbel, Preparation and studies of transparent conductive monolayers of multiwall carbon nanotubes on quartz and flexible polymer with the use of modified Langmuir technique, *Prog. Org. Coatings* 86 (2015) 86–95.
- [17] B. Hamankiewicz, M. Michalska, M. Krajewski, D. Ziołkowska, L. Lipińska, K. Korona, et al., The effect of electrode thickness on electrochemical performance of LiMn₂O₄ cathode synthesized by modified sol-gel method, *Solid State Ionics* 262 (2014) 9–13.
- [18] M. Michalska, B. Hamankiewicz, D. Ziołkowska, M. Krajewski, L. Lipińska, M. Andrzejczak, et al., Influence of LiMn₂O₄ modification with CeO₂ on electrode performance, *Electrochim Acta* 136 (2014) 286–291.
- [19] M. Thunmana, K. Marquardt, R. Hahn, D. Koberc, O. Goerke, H. Schubert, Discharge Performance Dependence on Electrode Thickness for Li₄Ti₅O₁₂/LiMn₂O₄ Cells for application in Wafer-integrated Microbatteries, *ECS Transactions* 41 (2012) 147–157.
- [20] G. Nazri, G. Pistoia, Lithium batteries: science and technology, Kluwer Academic Publishers, Boston, 2004.

Supplementary materials for

Novel method of current collector coating by multiwalled carbon nanotube Langmuir layer for enhanced power performance of LiMn_2O_4 electrode of Li-ion batteries

Karol Rytel^a, Daniel Waszak^b, Kamil Kędzierski^a, Danuta Wróbel^{a*}

^a Faculty of Technical Physics, Poznań University of Technology, 60-965 Poznań, Poland

^b Institute of Non-Ferrous Metals, Division in Poznań, Central Laboratory of Batteries and Cells, Department of Advanced Materials, ul. Forteczna 12, 61-362 Poznań, Poland

*Corresponding author: Danuta Wróbel, email. danuta.wrobel@put.poznan.pl, tel. +48 61 665 3179

Appendix A: MWCNTs suspension preparation

3 mg of MWCNT (Sigma-Aldrich, diameter 6-9 nm, length 5 μm) powder was added to 75 ml chloroform (Uvasol) and sonicated for 20 min (Ultra-sonic Bath POLSONIC; 300 W). The suspension was kept in a glass container for 48 h to allow bigger MWCNT aggregates to settle. Then, 50 ml of the top part of the sample was collected, and 50 ml chloroform was added to the collected dispersion and sonicated again for 20 min. The suspension was very stable and after 30 days storage at about 4°C no sediment was observed.

Appendix B: Floating film formation (Langmuir layer)

MWCNT Langmuir layers were obtained using the model 2000 Langmuir-Blodgett system (KSV Instrument Ltd.) with the Teflon trough of 870 cm^2 (custom made) at 21 °C. Deionized water (electric resistivity 18.2 $\text{M}\Omega\text{ cm}$) obtained with an ultrapure water purification system (Millipore Corp) was used as a subphase.

To obtain a floating film the MWCNT suspension was carefully spread onto the subphase and the chloroform was allowed to evaporate. The floating film was compressed symmetrically from both sides at the 75 $\text{mm}^2\text{ min}^{-1}$ rate of surface compression change. The surface pressure during the film compression was recorded using Wilhelmy plate method. Before transferring the MWCNT Langmuir layer was relaxed at 20 mN m^{-1} surface pressure for 15 min in order to produce a more homogenous film, with respect to non-relaxed film. Schemes of this methods was presented in Fig B.1 and Fig B.2.

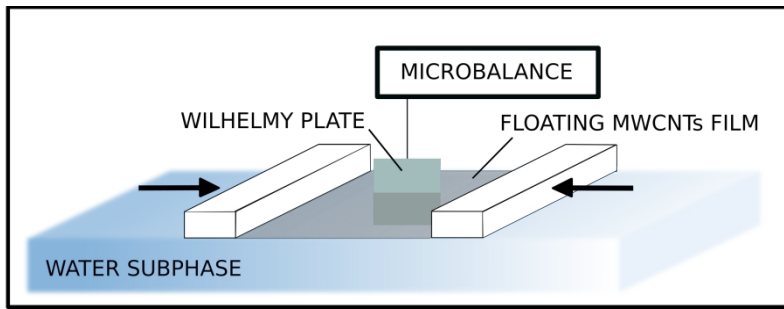


Fig. B.1 Scheme of Langmuir layer formation

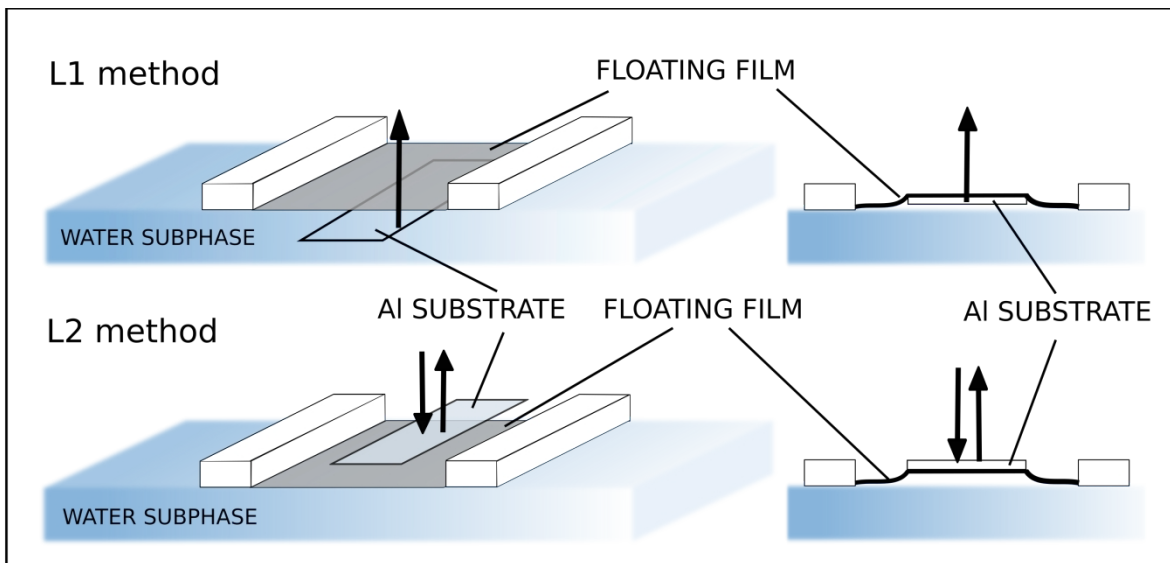


Fig. B.2 Scheme of L1 and L2 MWCNTs layer transfer methods

Appendix C: optical properties of MWCNTs coating

The optical image of Al substrate coated by mono and double layer of MWCNTs is presented in Fig. C.1.

The total reflectance spectra of MWCNTs coated Al in the wavelength range 350-900 nm were recorded using a spectrophotometer (Cary 4000 Varian) with diffuse reflectance accessory (DRA); the incident beam was directed at the $3^{\circ} 20'$ angle with respect to the sample normal. As a the reflectance standard PTFE (Varian) has been used.

The total reflectance spectra of the Al substrate and MWCNTs layer transferred on Al (L1 method) are shown in Fig. C.2 Al substrate reflects about 90% of light in tested range. The MWCNTs coating causes decrease of reflectance however, the total reflectance of L1 layer transferred onto Al exhibit reflectance higher than 55% over the range.

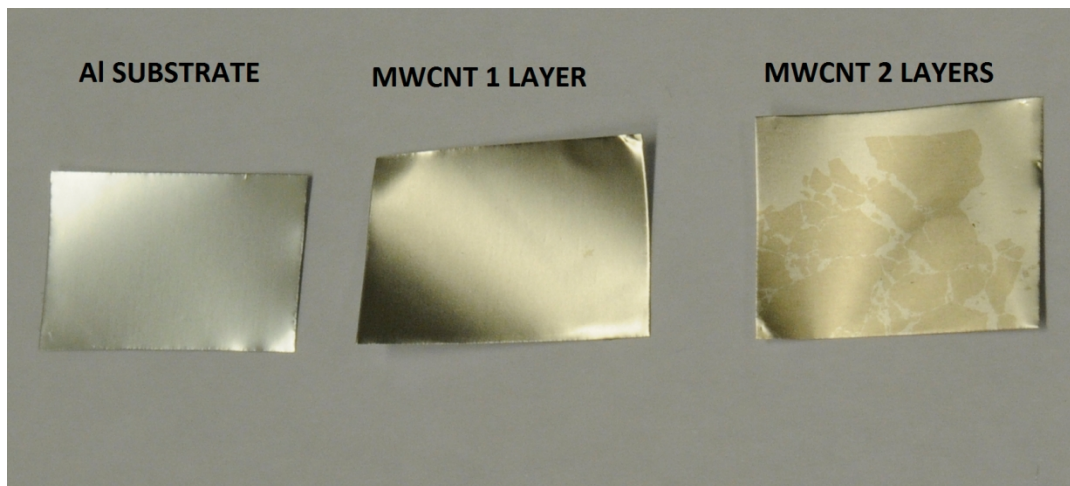


Fig. C.1 Optical image of tested current collectors

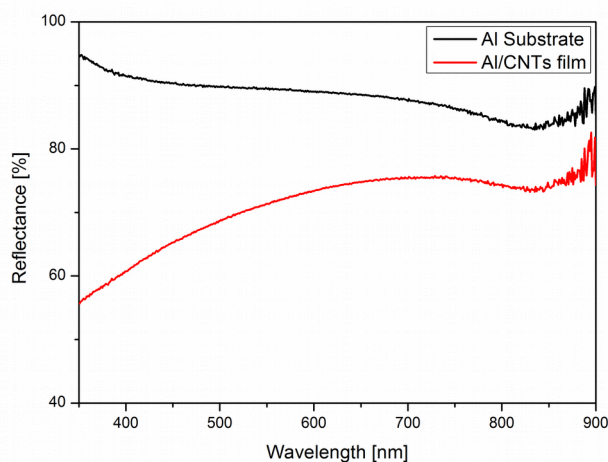


Fig. C.2 The total reflectance spectra of Al substrate and MWCNTs L1 layer transferred onto Al

Appendix D: cathode preparation

Slurry of LiMn_2O_4 powder (80 wt.%), polyvinylidene-fluoride binder (10 wt.%, PVDF, Fluka) and carbon black (10 wt.%, Vulcan XC72R) have been mixed and dissolved in N-methyl-pyrrolidone (NMP, Sigma Aldrich). A uniform slurry was achieved by adding 2.5 ml NMP to 1 g of mixed powder. To prepare the cathode electrodes, pure and modified Al foil was coated by the slurry using the doctor-blade technique.

The cross section SEM image of the C electrode (mass loading 6.4 mg cm^{-2}) was shown at Fig. D.1. The Al substrate visible on the image on the left side (more homogenous part) having a thickness of about $10 \mu\text{m}$.

The cathode material right side of the image (more porous) is characterized by the thickness of about $20 \mu\text{m}$.

The SEM image has been done by using Phenom ProX microscope.

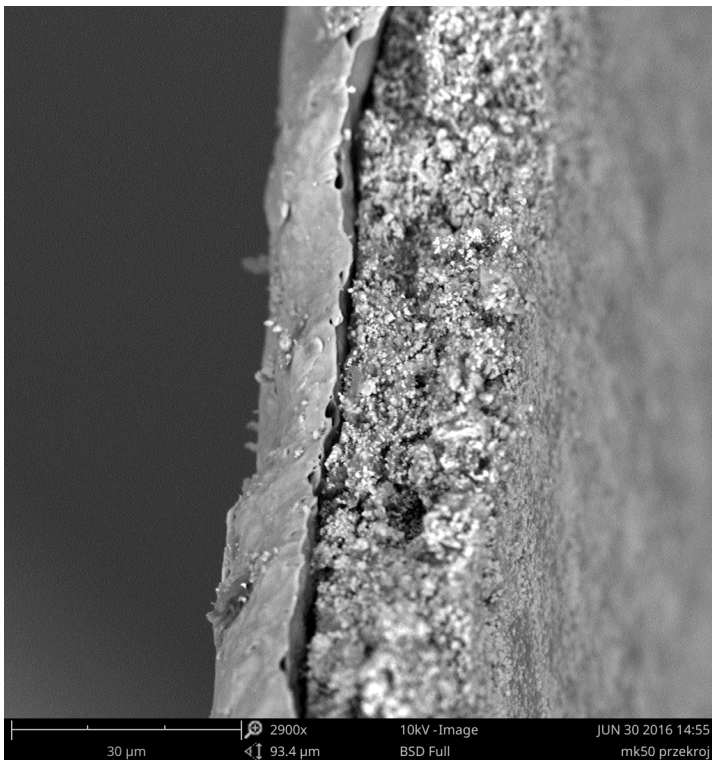


Fig. D.1 The cross section SEM image of the C electrode

Appendix E: Cell preparation and electrochemical tests

In tested Swagelok type system Celgard 2400 was used as the separator and a liquid mixture (Baf LP30) containing solution of 1M LiPF_6 dissolved in ethylene carbonate (EC) and dimethyl carbonate (DMC) of volume proportion 1:1 was used as the electrolyte. All cells were assembled in an Ar-filled glove box.